Electrostatic Assist of Liquid Transfer in Printing Processes

A DISSERTATION
SUBMITTED TO THE FACULTY OF THE GRADUATE SCHOOL
OF THE UNIVERSITY OF MINNESOTA
BY

Chung-Hsuan Huang

IN PARTIAL FULFILLMENT OF THE REQUIREMENTS
FOR THE DEGREE OF
DOCTOR OF PHILOSOPHY

Advisor: Satish Kumar

July, 2018

Acknowledgements

Many people have earned my gratitude for their contribution to my time in graduate school. Firstly, I would like to express my sincere appreciation to my advisor Prof. Satish Kumar for his patience, motivation, and immense knowledge and the continuous support of my Ph.D. study over the past five years. He has guided me the processes of conducting high-quality scientific research and writing of this thesis. I could not have imagined having a better advisor and mentor for my Ph.D. study. I would thank Prof. Marcio Carvalho for his invaluable suggestions that help me build the finite element codes. I sincere thanks also goes Wieslaw Suszynski, who provided essential technical support for the experimental part of this work. Without their precious support, it would not be possible to conduct this research. Besides my advisor, I would like to thank the rest of my thesis committee: Prof. Cari Dutcher, Prof. Lorraine Francis, and Prof. Joseph Zasadzinski for serving on my graduate committee and for their insightful comments on my dissertation to widen my research from various perspectives.

I am grateful for the funding from the Industrial Partnership for Research in Interfacial Materials and Engineering (IPRIME program) and the resources provided by the Department of Chemical Engineering and Materials Science and Minnesota Supercomputing Institute. I appreciate the opportunity to be part of the Coatings Process Fundamentals Program (CPFP), from which I received valuable feedback and comments from the people from both academia and industry.

I would like to thank all my colleagues in my research group, including Dr. Aruna Ramkrishnan, Dr. Leonardo Espin, Dr. Andrew Corbett, Dr. Joonsik Park, Dr. Chen-Yu Liu, Dr. Weihua Li, Truong Pham, Jyun-Ting Wu, Gokul Hariharan, Chance Parrish, Panayiotis Kolliopoulos, and Vasileios Charitatos for all the research discussions and fun we have had in the last five years. I am especially grateful to Dr. Shawn Dodds

for helping me build my slender-jet code, and to Dr. Weihua Li for discussing and troubleshooting the finite element code with me.

I want to thank my friends and family for all for supporting me spiritually throughout this journey and my life in general. Finally, and most of all, I would like to thank my wife, Jessica Liu for all her love and support. I am very fortunate that I have met Jessica in my life. I'll always cherish the moments we spent together and all the beautiful memories we made, and I look forward to our future together.

Dedication

To my dearest parents, Chao-Mu Huang and Shu-Chih Chang, and my wonderful wife, Jessica Liu.

Abstract

Printing processes are being explored for the large-scale manufacture of electronic devices. Transfer of liquid from one surface to another plays a key role in most printing processes. During liquid transfer, a liquid bridge is formed and then undergoes significant extensional motion. Incomplete liquid transfer can produce defects that can be detrimental to device operation. One important printing process is gravure, which involves transfer of liquid from micron-scale cavities at high speeds. Electric fields are sometimes used to enhance liquid transfer, a technique known as electrostatic assist (ESA). However, its underlying physical mechanisms remain a mystery. This thesis uses a combination of theory and experiment to understand the fundamental mechanisms by which electrostatic forces influence liquid transfer.

Liquid transfer without electric fields and cavities must be understood before studying the mechanism of ESA. We develop one-dimensional (1D) slender-jet and two-dimensional (2D) axisymmetric models of this phenomenon and compare the resulting predictions with previously published experimental data. At relatively low stretching speeds, predictions from both models of the amount of liquid transferred agree well with the experimental data. When the stretching speed is high enough, the models predict that each surface receives half the liquid, in agreement with experimental observations. For intermediate values of the stretching speed, predictions from each model can deviate substantially from the experimental data, which we speculate is due to the influence of surface defects that are not included in the models.

The 1D and 2D model are modified to include electrostatic effects. The liquid behaves like a perfect (non-conducting), or leaky dielectric (poorly conducting) material. The liquid is confined between two plates, with the top plate having a constant electrostatic potential while the bottom plate is grounded. For perfect dielectrics, application of an electric field enhances liquid transfer to the more wettable surface because it slows the surface-tension-driven breakup of the bridge, thereby allowing more time for the contact line to retract on the less-wettable surface. For leaky dielectrics, application of an electric field can augment or oppose the influence of wettability differences, depending on the direction of the electric field and the sign of the interfacial charge. Experimental

results confirm the enhancement of the amount of liquid transferred when the electric field is present, and the measured values are in good agreement with the predictions of the 1D perfect dielectric model.

When one of the plate is replaced by a cavity, the presence of the cavity causes the contact line on the cavity wall to effectively pin and inhibits the liquid transfer. For perfect dielectrics, application of an electric field unpins the contact line on the cavity and leads to improvement of cavity emptying. For the leaky dielectrics, the presence of the surface charge does not further improve liquid transfer because of nearly zero electric tangential stress near the contact line on each surface.

Contents

Acknowledgements **i**

Dedication **iii**

Abstract **iv**

List of Tables **ix**

List of Figures **x**

1 Introduction **1**

1.1 Background 2

1.1.1 Gravure Printing Processes 2

1.1.2 Contact Angle 4

1.1.3 Fundamentals of Electrohydrodynamics 5

1.2 Thesis Overview 6

1.2.1 Stretching Liquid Bridges with Moving Contact Lines: Comparison of Model Predictions and Experiments 7

1.2.2 Electrostatic Assist of Liquid Transfer between Flat Surfaces . . 8

1.2.3 Electrostatic Assist of Liquid Transfer with Plates and Cavities . 8

2 Stretching liquid bridges with moving contact lines comparison of liquid-transfer predictions and experiments **10**

2.1 Introduction 10

2.1.1 Prior experimental work 11

2.1.2 Overview of present paper 13
2.2 Problem formulation 14
2.2.1 Governing equations 14
2.2.2 2D axisymmetric model 15
2.2.3 1D slender-jet model 16
2.2.4 Parameter values 17
2.3 Comparison to experiments of Chen *et al.* 17
2.3.1 Quasi-static experiments 18
2.3.2 Dynamic experiments 22
2.4 Comparison to experiments of Qian and Breuer 25
2.5 Effect of initial bridge shape 28
2.5.1 Parametric study 28
2.5.2 Comparison to experiments of Gupta *et al.* 30
2.6 Conclusions 32

3 Electrostatic Assist of Liquid Transfer between Flat Surfaces 34
3.1 Introduction 34
3.2 Problem formulation 37
3.2.1 Governing equations 37
3.2.2 1D slender-jet model 39
3.2.3 Solution method 40
3.2.4 Parameter values 41
3.3 Results: Perfect dielectrics 42
3.3.1 Liquid transfer 42
3.3.2 Physical mechanisms 47
3.3.3 Influence of initial bridge shape 51
3.4 Results: Leaky dielectrics 53
3.4.1 Role of tangential stresses 54
3.4.2 Liquid transfer 55
3.5 Experiments 58
3.5.1 Experimental setup 59
3.5.2 Results: Two identical surfaces 60

3.5.3 Results: Two different surfaces 62
3.5.4 Comparison to model predictions 64
3.6 Conclusions 67

4 Electrostatic Assist of Liquid Transfer with Plates and Cavities 69
4.1 Introduction 69
4.1.1 Motivation 69
4.1.2 Summary key findings from recent previous work 71
4.1.3 Overview of present paper 72
4.2 Problem formulation 73
4.2.1 Governing equations 74
4.2.2 Solution method 77
4.3 Results - Flat Plates 78
4.3.1 Perfect dielectric 78
4.3.2 Leaky dielectric 86
4.4 Results - Cavity 90
4.4.1 Perfect dielectric 91
4.4.2 Leaky dielectric 97
4.5 Conclusions 100

5 Final Remarks 102
5.1 Conclusions 102
5.2 Future research directions 104
5.3 Final remarks 106

References 107

List of Tables

2.1 Dimensionless problem parameters. The Bond number is denoted by Bo, the Weber number by We, and the initial aspect ratio of the bridge by Λ. 18

3.1 Order-of-magnitude values of dimensional parameters 42

3.2 Dimensionless problem parameters 42

3.3 Comparison of transfer ratios for different initial bridge shapes 53

3.4 Mean transfer ratios and bridge breakup lengths when both surfaces are identical 61

3.5 Contact line motion, transfer ratio and the breakup length in the experiments with two different surfaces 63

3.6 Predicted transfer ratio and breakup length for different boundary conditions. The entries in boldface correspond to the conditions observed in the experiments. 65

4.1 Order-of-magnitude values of key dimensional parameters 73

4.2 Dimensionless problem parameters 75

List of Figures

1.1 Electronic circuits printed on flexible substrates [1, 2]. 1

1.2 (a) Schematic of a gravure printing process. (b) Schematic of stretching liquid bridge. 3

1.3 The images printed with ESA off (left), and ESA on (right). Image from Ref. [3]. 4

1.4 Schematic showing the quantities in Young's equation. 5

1.5 Schematic of the steps of liquid bridge stretching. The gripper surface is lowered until a liquid bridge is formed. Then, the gripper is retracted with a constant velocity until the liquid bridge breaks. Image from Ref. [4]. 7

2.1 (a) Schematic of a gravure printing process. The ink in a cavity is transferred from an engraved roll to a substrate. (b) Illustration of a stretching liquid bridge. 11

2.2 Schematic of liquid bridge and coordinate system. Note that $L(t = 0) \equiv L$. 14

2.3 Relationship between liquid transfer ratio and Ca for different values of $\Delta\ \theta_r$. Here θ_{top}=60° and θ_{bottom} is varied. 19

2.4 (a) Comparison of predicted liquid transfer ratios with experimental results [5]. (b) Position of the contact lines on both surfaces during the stretching process for case 8 in Ref. [5] where $\Delta\theta_r = 15°$. For the simulations, Ca=10^{-3}. 20

2.5 Comparison of predicted liquid transfer ratios with experimental results [6]. (a) Transfer from Teflon (θ_r=106.7) to PEMA (θ_r=61.7). (b) Transfer from OTS (θ_r=83.9) to PEMA. (c) PS (θ_r=56.6) to PEMA. (d) Transfer from silicon (θ_r=37.3) to PEMA. 23

2.6 Radius of droplet deposited on bottom plate r_d non-dimensionalized with the radius of the top plate R as a function of the speed of the top plate U. The dimensionless bridge volume is $V = v/\pi\ R^3$, where v is the dimensional volume. The experimental data are from Figure 9 of Ref. [7]. 26

2.7 (a) Droplet radius (contact-line position) on bottom plate $r(0)$ versus bridge height h. Both quantities are non-dimensionalized using the radius of the top plate R. Experimental data are from Figure 2 of Ref. [7], where $U = 100$ μm/s. (b) Contact-line velocity u_c as a function of contact-line position. Here, U is the velocity of the top plate (600 μm/s). Note that increasing time corresponds to decreasing $r(0)$. Experimental data are from Ref. [7]. 27

2.8 (a) Transfer ratio as a function of θ_{bottom} for different bridge aspect ratios Λ. Here, the contact line on the top plate is pinned. (b) Transfer ratio as a function of $\Delta\ \theta_r = \theta_{\text{bottom}}$ - θ_{top} for different bridge aspect ratios Λ. Here, $\theta_{\text{bottom}} = 60^\circ$. For all the calculations in this figure, $Ca = 0.1$. . . 29

3.1 (a) Schematic of a gravure printing process with electrostatic assist. The ink in a cavity is transferred from an engraved roll to a substrate. (b) Illustration of a stretching liquid bridge. (c) Schematic of a stretching liquid bridge subject to an electric field. 35

3.2 Relationship between transfer ratio and wettability difference for different values of χ for (a) $Ca = 0.1$ and (b) $Ca = 1$. Here, θ_{top} is 60° and θ_{bottom} varies from 40° to 80°. The wettability difference is $\Delta\theta_r = \theta_{\text{bottom}} - \theta_{\text{top}}$, and the parameter $\beta = 1.74$. 43

3.3 Comparison of final bridge shapes and contact-line positions for the cases $\chi = 0$ (solid lines) and 50 (dashed lines). (a,c) $Ca = 0.1$; the breakup times for $\chi = 0$ and 50 are 2.1 and 2.4, respectively. (b,d) $Ca = 1$; the breakup times for $\chi = 0$ and 50 are 8.8 and 7.6, respectively. Values of other parameters are $\theta_{\text{bottom}} = 70^\circ$, $\theta_{\text{top}} = 60^\circ$, $\Delta\theta_r = 10^\circ$, and $\beta = 1.74$. 45

3.4 Relationship between transfer ratio and the value of bottom contact angle for different values of χ. The top contact line is pinned and θ_{bottom} is varied. Values of other parameters are $Ca = 1$ and $\beta = 1.74$. 46

3.5 (a) Comparison of bridge shapes for the cases $\chi = 0$ (solid line) and 50 (dashed line) at $t = 1$. (b) Comparison of relative pressure for the cases $\chi = 0$ (solid line) and 50 (dashed line) at $t = 1$. Values of other parameters are $Ca = 1$, $\theta_{\text{bottom}} = 60°$, $\theta_{\text{top}} = 60°$, $\Delta\theta_r = 0°$, and $\beta = 1.74$. 48
3.6 Comparison of bridge shapes (a,c) for the cases $\chi = 0$ (solid line) and 50 (dashed line) with corresponding relative pressures (b,d) at (a,b) $t = 1$ (c,d) $t = 4$. Values of other parameters are $Ca = 1$, $\theta_{\text{bottom}} = 70°$, $\theta_{\text{top}} = 60°$, $\Delta\theta_r = 10°$, and $\beta = 1.74$. 49
3.7 (a) Equilibrium bridge shapes for $Ca_E = 0$ (solid line), 10 (dashed line), and 50 (dotted line) when $\Delta\theta_r$ is 0° ($\theta_{\text{bottom}} = 60°$, $\theta_{\text{top}} = 60°$). (b) Equilibrium bridge shapes for $Ca_E = 0$ (solid line) and 50 (dashed line) when $\Delta\theta_r$ is 10° ($\theta_{\text{bottom}} = 70°$, $\theta_{\text{top}} = 60°$). Here, $\beta = 1.74$. 52
3.8 (a) Comparison of equilibrium bridge shapes between the cases where $\sigma_o = 0$ (solid line) and 0.1 (dashed line). The wettability difference $\Delta\theta_r = 0°$ with both the top and bottom contact angles set to 60°. (b) Equilibrium bridge shape for the case where $\sigma = 0.1$ and both contact lines are fixed at 1. Values of other parameters are $Ca_E = 50$, $K^* = 1$, and $\beta = 1.74$. . 54
3.9 Relationship between transfer ratio and wettability difference when $\chi = 0$ and $\chi = 50$ at (a) $Ca = 0.1$ and (b) $Ca = 1$. Here θ_{top} is 60° and θ_{bottom} varies. Values of other parameters are $K^* = 1$, σ = -0.1, and $\beta = 1.74$. 56
3.10 Comparison of electrified and non-electrified bridge shapes at different times for the case where $\Delta\theta_r = 10°$ ($\theta_{\text{bottom}} = 70°$, $\theta_{\text{top}} = 60°$) at $Ca = 0.1$. Values of other parameters are σ_o = -0.1, $K^* = 1$, and $\beta = 1.74$. The breakup time for the electrified bridge is 1.1 and the breakup time for the non-electrified bridge is 2.1. 57
3.11 Schematic of experimental apparatus 59
3.12 Visualizations of static liquid bridge shapes between two aluminum surfaces (a) without an electrostatic potential difference ($Ca_E = 0$) and (b) with an electrostatic potential difference of 1 kV ($Ca_E \approx 0.1$). 61

3.13 Visualizations of the liquid bridge (a) before stretching and (b) after liquid bridge breaks without application of an electrostatic potential difference ($\chi = 0$). Visualizations of the liquid bridge (c) before stretching and (d) after application of an electrostatic potential difference of 1.5 kV ($\chi \approx 27$). 63
3.14 (a) Initial bridge shapes and (b) final bridge shapes with ($\chi = 27$; dashed line) and without ($\chi = 0$; solid line) the electric field. Both top contact radii are fixed at 0.8 mm. The bottom contact radius for the case where $\chi = 0$ is fixed at 1 mm, while the bottom contact radius for the case where $\chi = 27$ is free to move and the contact angle is 58°. Here, $\beta = 44.9$. 65
4.1 (a) Schematic of a gravure printing process with electrostatic assist (ESA). Ink is transferred from a cavity to a substrate, sometimes with the help of an electrostatic potential difference. (b) Schematic of a stretching liquid bridge. 70
4.2 70
4.3 Relationship between transfer ratio and wettability difference for different values of χ at (a) $Ca = 0.1$ and (b) $Ca = 0.5$. Here, $\theta_{\text{top}} = 60°$, and θ_{bottom} varies from 40° to 80°. The wettability difference $\Delta\theta_r = \theta_{\text{bottom}} - \theta_{\text{top}}$. . 79
4.4 Relationship between transfer ratio and wettability difference predicted by the 1D slender-jet model for different values of χ at (a) $Ca = 0.1$ and (b) $Ca = 0.5$. Here, $\theta_{\text{top}} = 60°$, and θ_{bottom} varies from 40° to 80°. The wettability difference $\Delta\theta_r = \theta_{\text{bottom}} - \theta_{\text{top}}$. 80
4.5 (a) Time-evolution of contact line on top and bottom plates for $\chi = 0$ (solid line) and 40 (dashed line). (b) Final bridge shapes for $\chi = 0$ (solid line) and 40 (dashed line). The bridge breakup times for $\chi = 0$ and 40 are 5.4 and 8.3, respectively. Values of other parameters are $Ca = 0.5$, $\theta_{\text{top}} = 60°, \theta_{\text{bottom}} = 80°$, and $\Delta\theta_r = 20°$. 81
4.6 (a) Time-evolution of contact line on top and bottom plates for $\chi = 0$ (solid line) and 40 (dashed line). (b) Final bridge shapes for $\chi = 0$ (solid line) and 40 (dashed line). The breakup times for $\chi = 0$ and 40 are 5.6 and 4.4, respectively. Values of other parameters are $Ca = 0.5$, $\theta_{\text{top}} = 60°, \theta_{\text{bottom}} = 80°$, and $\Delta\theta_r = 20°$. 82

4.7 Pressure contours and bridge shapes for the cases where (a,c) $\chi = 0$ and (b,d) $\chi = 40$ at (a,b) $t = 0.6$ and (c,d) $t = 5$. The bridge breakup times for $\chi = 0$ and 40 are 5.4 and 8.3, respectively. Values of other parameters are $Ca = 0.5$, $\theta_{\text{top}} = 60°, \theta_{\text{bottom}} = 80°$, and $\Delta\theta_r = 20°$. 83

4.8 Electrostatic potential contours and bridge shapes for for the case where $\chi = 40$ at (a) $t = 0.6$ and (b) $t = 5$. Values of other parameters are $Ca = 0.5$, $\theta_{\text{top}} = 60°, \theta_{\text{bottom}} = 80°$, and $\Delta\theta_r = 20°$. 84

4.9 Comparison equilibrium bridge shapes for different Pe. Here, $\theta_{\text{top}} = \theta_{\text{bottom}} = 60°$, $\Delta\theta_r = 0°$, and $Ca_E = 40$. 87

4.10 Transfer ratio vs. wettability difference for cases where $\chi = 0$ ($\square$), $\chi = 40$, $q_o = 0$, $K^* = 0$ ($\bigcirc$), $\chi = 40$, $q_o = 0.5$, $K^* = 0$ ($\triangle$), $\chi = 40$, $q_o = 0.5$, $K^* = 1$ ($\triangledown$), and $\chi = 40$, $q_o = 0$, $K^* = 1$ ($\triangleleft$). Here, $\theta_{\text{top}} = 60°$, and θ_{bottom} varies from 40° to 80°. Values of other parameters are $Ca = 0.5$ and $Pe = 1000$. 88

4.11 Bridge shapes at times (a) $t = 4$, (b) $t = 6$, and (c) $t = 8$. The breakup times for the cases with $q_o = 0$, $K^* = 0$ (solid line), $q_o = 0.5$, $K^* = 0$ (dashed line), and $q_o = 0$, $K^* = 1$ (dotted line) are 8.3, 6.9, and 8.0, respectively. Values of other parameters are $Ca = 0.5$, $\chi = 40$, $\theta_{\text{top}} = 60°$, $\theta_{\text{bottom}} = 80°$, and $\Delta\theta_r = 20°$. 89

4.12 Relationship between transfer ratio and wettability difference for different values of χ at (a) $Ca = 0.1$ and (b) $Ca = 0.5$. Here, $\theta_{\text{top}} = 70°$, and θ_{bottom} varies from 50° to 90°. The wettability difference $\Delta\theta_r = \theta_{\text{bottom}} - \theta_{\text{top}}$. . 91

4.13 (a) Time-evolution of contact-line on top (flat plate) and bottom (cavity) surfaces for $\chi = 0$ (solid line) and 40 (dashed line). (b) Final bridge shapes for $\chi = 0$ (solid line) and 40 (dashed line). The bridge breakup times for $\chi = 0$ and 40 are 2.8 and 3.9, respectively. Values of other parameters are $Ca = 0.5$, $\theta_{\text{top}} = 70°$, $\theta_{\text{bottom}} = 90°$, and $\Delta\theta_r = 20°$. 93

4.14 Pressure contours and interface shapes for (a,b) $\chi = 0$ and (c,d) $\chi = 40$ at $t = 0.4$. Panels (a) and (c) show the region near the contact line on the cavity wall, and panels (b) and (d) show the region near the flat plate. Values of other parameters are $Ca = 0.5$, $\theta_{\text{top}} = 70°, \theta_{\text{bottom}} = 90°$, and $\Delta\theta_r = 20°$. 94

4.15 (a) Cavity shapes for $\delta = 1$ (right) and 0.5 (left). (b) Relationship between transfer ratio and wettability difference for different values of χ and cavity depths at $Ca = 0.5$. Here, $\theta_{\text{top}} = 70°$, and θ_{bottom} varies from 50° to 90°. 96

4.16 Pressure contours and interface shapes for the (a) shallow cavity and (b) deep cavity at $t = 0.4$. Values of other parameters are $Ca = 0.5$, $\chi = 40$, $\theta_{\text{top}} = 70°, \theta_{\text{bottom}} = 90°$, and $\Delta\theta_r = 20°$. 97

4.17 (a) Relationship between transfer ratio and wettability difference when (i) $q_o = 0$, $K^* = 0$ ($\square$), (ii) $q_o = 0.5$, $K^* = 0$ ($\triangle$), (iii) $q_o = 0$, $K^* = 1$ ($\triangledown$), and (iv) $q_o = 0.5$, $K^* = 1$ ($\bigcirc$). Here, $\theta_{\text{top}} = 70°$, and θ_{bottom} varies from 50° to 90°. (b) Final bridge shapes for different cases when $\theta_{\text{top}} = \theta_{\text{bottom}} = 70°$ The bridge breakup times for cases (i)-(iv) are 3.56, 3.64, 3.73, and 3.55, respectively. Values of other parameters are $Ca = 0.5$ and $\chi = 40$. 98

4.18 (a,b) Electrostatic potential contours and (c,d) electrostatic contribution to the tangential stress for liquid transfer between (a,c) flat plates and (b,d) a flat plate and a cavity at $t = 0.6$. Values of other parameters are $Ca = 0.5$, $\chi = 40$, $\theta_{\text{top}} = \theta_{\text{bottom}} = 70°$, $q_o = 0.5$, and $K^* = 1$. 99

Chapter 1

Introduction

Printing processes are ubiquitous in daily life and industrial manufacturing. We see printing products around us every day such as newspapers, packages, and magazines because printing is an efficient way to disseminate information. Nevertheless, printing techniques are not only used to make books and newspapers but increasingly being applied to fabricate electronic devices such as flexible electric circuits [8](Fig. 1.1), organic light emitting diodes [9], biosensor [10], and solar cells [11]. The market for the printed electronics will grow from $29.28 billion in 2017 to $73.43 billion in 2027 [12]. One of the challenges in the electronics industry is how to reduce production costs. Electronic products such as radio frequency identification (RFID) tags are made by expensive techniques, but if traditional printing techniques were used, production costs could be significantly reduced [13, 14].

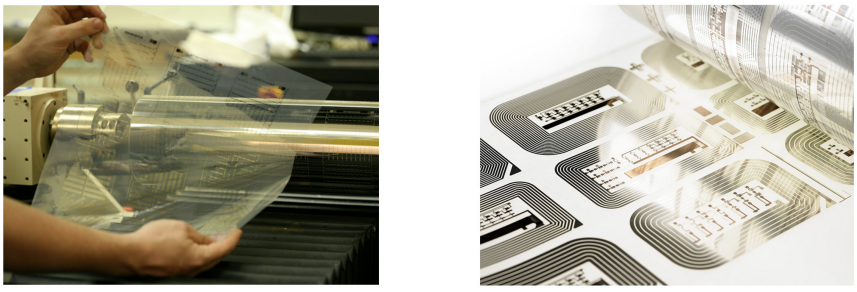

Figure 1.1: Electronic circuits printed on flexible substrates [1, 2].

One of the advantages of printing processes is that the pattern can be printed on a flexible surface. In these printing processes, the inks are conductive materials that are deposited onto a flexible substrate that is unwound from a cylindrical roll and then wound onto another roll after printing. Such roll-to-roll printing techniques have significant potential to reduce production costs and dramatically speed up manufacturing processes [15, 16]. Even though using the roll-to-roll processing to fabricate printed electronics is still in the research and development phase, there has been some research showing that gravure printing could be a promising method [17, 18, 19, 20]. For the traditional printing processes, the resolution is in the range of 20 to 100 μm, and the speed of printing is on the order of 1 to 10 m/s [20, 21]. However, for printed electronics, this requires the lateral length scale as small as 100 nm [22]. Therefore, it requires a fundamental understanding of the physical mechanisms that governing printing processes to achieve such small scales.

For printed electronics, it is essential that enough ink is transferred from the cavities to the substrate to prevent broken circuits and failure of printed electronics. In traditional gravure printing, electric fields have been applied to improve ink transfer from one surface to another, a method known as electrostatic assist (ESA). However, the physical mechanisms underlying ESA are still not well understood. There is a knowledge gap and it is worth investigating the fundamentals of liquid transfer in the presence of an electric field. A better understanding of these mechanisms would allow for more systematic design of ESA systems, which could be used to make high-end graphics and might have potential to be applied in printed electronics. This thesis describes research addressing how the electric fields may influence liquid transfer in printing processes.

1.1 Background

1.1.1 Gravure Printing Processes

Printing processes are one of the most significant inventions in human history. Printing processes are used to produce many kinds of materials at high volumes, such as stamps and books. Printing techniques also have received significant attention for the manufacturing of various electronic devices because printing techniques may allow it to be faster and cheaper [23]. The gravure printing process, as shown in figure 1.2(a), has a

high potential for manufacturing printed electronics with a length scale of 10 μm or less [24]. Gravure printing processes involve formation of a liquid bridge and then transfer of ink from the gravure roll to the flexible substrate. A brief overview of gravure printing processes is given in this section.

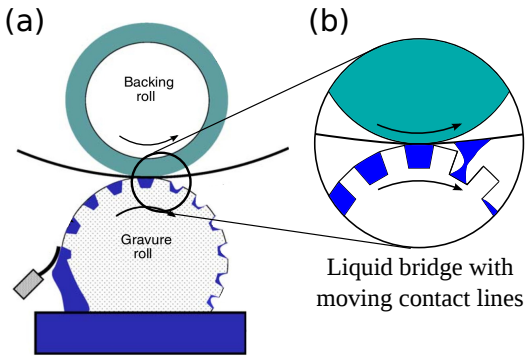

Figure 1.2: (a) Schematic of a gravure printing process. (b) Schematic of stretching liquid bridge.

Gravure printing is one of the most widely used and fastest printing methods in the world. This printing process involves an engraved gravure roll which carries the image, a doctor blade, and an impression backing roll. The cells of the engraved roll are filled with ink from the pool beneath it, and the doctor blade wipes off any excess fluid from the cylinder surface leaving only ink in the gravure cells. As shown in Fig. 1.2(b), a liquid bridge is formed and transferred from the cells onto the substrate of interest with the impression roll. The width of gravure printing cells is typically smaller than 100 μm [25], so this method is used for those products that require high resolution like books or magazines. However, the liquid transfer is often incomplete and leaves the liquid or residual solids in the cells. The accumulation of residual solids may cause printing defects because the effective cell volume and geometry have been altered [26].

Electrostatic assist (ESA) has been used for about 50 years to improve liquid transfer. Figure 1.3 shows that the difference between printing with and without the electrostatic assist. As can be seen in Fig. 1.3(a), such serious printing defects in gravure printing are known as dot skip. Increased impression pressure is used to overcome the problem. However, the high compression wears out the press components and degrades productivity [27]. Instead of using such high pressure to try to make the substrate closer to

Figure 1.3: The images printed with ESA off (left), and ESA on (right). Image from Ref. [3].

the cells, ESA provides a much better way to enhance ink transfer. As shown in Fig. 1.3(b), when the ESA is applied, it improves the quality of the print.

In the ESA system, the gravure roll is grounded, and an electric potential is applied to the conductive covering of the backing roll to form an electric field between two rollers [28, 29]. The electric potential difference required for the effectiveness is in the 100 to 200 volt per 0.001 inch range [27]. In addition, ESA system is suitable for most of the solvent used in gravure printing processes such as water, acetates, toluene, and ethanol [28]. Therefore, ESA is widely used in publication, packaging and woodgrain printing.

1.1.2 Contact Angle

Contact angles play an important role in liquid transfer. A brief introduction to contact angles is given in this section. The contact angle of a droplet is the angle between the solid-liquid interface and liquid-air interface (Fig 1.4). The equilibrium contact angle can be described by Young's equation:

$$\gamma_{lv}\cos(\theta_Y) = \gamma_{sv} - \gamma_{sl}, \tag{1.1}$$

where γ_{lv} is the liquid-vapor surface tension, γ_{sv} is the solid-vapor surface tension, γ_{sl} is the solid-liquid surface tension, and θ_Y is the Young contact angle.

Ideally, the Young contact angle should be constant in a given system, but a range of contact angles can be measured while moving the liquid, as in a liquid bridge being compressed or stretched. The upper limit is the advancing contact angle θ_a, which is

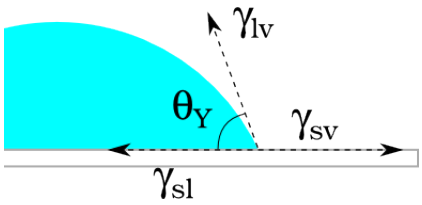

Figure 1.4: Schematic showing the quantities in Young's equation.

found as the contact line is about to move in the compression. The lower limit is the receding contact angle θ_r, when the contact line is about to retreat in the stretching. The difference between an advancing contact angle and a receding contact angle is known as contact angle hysteresis (CAH), θ_{hyst} [30].

1.1.3 Fundamentals of Electrohydrodynamics

Electric fields have been used to manipulate liquid behaviors during the 19th century and before [31]. In this section, we give a brief overview of electrohydrodynamics. Electrohydrodynamics describes the interaction between electric fields and fluid motions. The surface interaction plays a significant role in the EHD, and charges influence electric stresses on interface [32]. Three kinds of liquids can be described base on their conductivity. The first ones are perfect conductors such as mercury. The second ones are the opposite of the first ones and are called perfect dielectrics (apolar liquids such as benzene). The last ones are poorly conducting liquids called leaky dielectrics such as silicone oil or castor oil.

Most works of EHD focused on perfect conductors or perfect dielectrics until the 1960s [33]. The perfect dielectric is not a reasonable assumption for many electrical phenomena with moving liquids. Because many dielectrics still contain non-zero free charge, a non-zero tangential force will act at the interface if a non-zero electric field tangent to the interface is present. The viscous force is the only force that balances the tangential stress. This idea underlies the leaky dielectric model [34]. The character of leaky dielectrics is that the free charges accumulate on the liquid-air interface.

Taylor [35] and Melcher [32] pioneered the development of the leaky dielectric model to explain droplet behaviors under electric fields. The key to electrohydrodynamics is that electric fields exert forces on charge dipoles and free charge to create interfacial

stress. This electrostatic contribution to the interfacial stress can change the shape for different liquid structures such as liquid droplets, and liquid bridges. Therefore, electrohydrodynamics have been used to study the effects of electric fields on the stability and shape of droplets [36, 37], liquid bridges [38, 39], and thin films [40, 41]. These electrostatic effects are relevant to the application of inkjet printing [42], electrospinning [43, 34], and coating flows [44].

Inks used in printing processes are usually hydrocarbon solvent based, which are poor conductors [27]. The Taylor-Melcher leaky dielectric model is extensively used to explain liquid behavior in a steady field [33] and has been successfully compared with experiments [34, 39]. The perfect dielectric model can be obtained from the leaky dielectric model by setting the free charge and conductivity of liquid to zero [45]. A comparison of leaky and perfect dielectric models can help us understand the role of free charge in liquid bridge stretching.

1.2 Thesis Overview

For printed electronics to reach their full potential, better fundamental understanding of the liquid transfer process is essential. This thesis discusses here significantly contributes to this need by advancing our fundamental understanding of how factors such as electric field strength, surface wettability, and cavity shape influence liquid transfer.

Before studying the mechanism of ESA, we first develop models for liquid bridge stretching in the absence of an electric field and validate these models with experimental results. The key to printing processes involves the formation of a liquid bridge—a mass of liquid connecting two solid surfaces—and transfer of liquid from cavities to a substrate (Fig. 1.2(b)). During liquid transfer, the liquid bridge undergoes shearing, extensional, and rotational motion [46]. However, it is complex to consider all of the motions in the same time. This research mainly focuses on a model problem that the extension of a liquid bridge between two flat plates (Fig. 1.5) or a trapezoidal cavity and a flat plate.

A mass of liquid is initially deposited on the bottom surface. A second flat surface is brought down into contact with that liquid to form a liquid bridge. The top surface is then pulled vertically until the liquid bridge breaks. During this process, the contact lines (where air, liquid, and solid meet) move on the two flat surfaces. The central

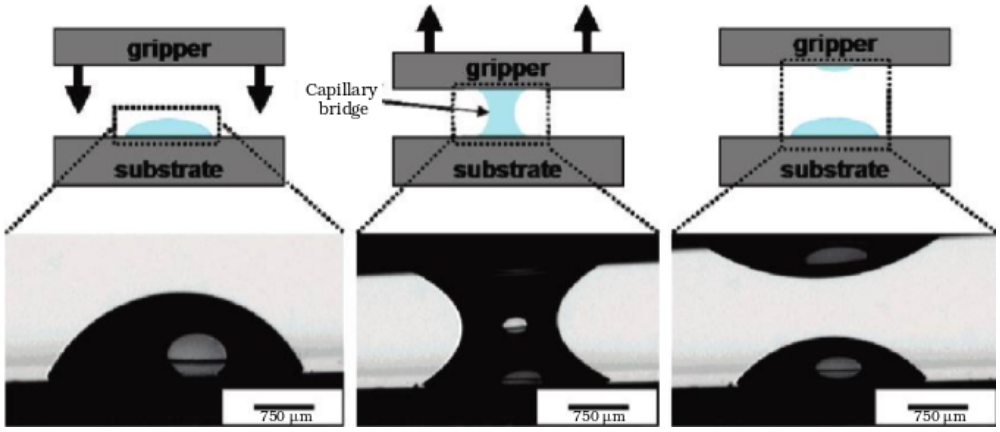

Figure 1.5: Schematic of the steps of liquid bridge stretching. The gripper surface is lowered until a liquid bridge is formed. Then, the gripper is retracted with a constant velocity until the liquid bridge breaks. Image from Ref. [4].

issue is to determine the amount of liquid transferred from the bottom surface (printing plate) to the top surface (substrate) as the two surfaces separate. This model problem is also highly relevant to other applications including adhesion [47], oil recovery [48], and microfluidics [49].

The remaining chapters of this thesis present three stages of the study the influence of electric field on the liquid transfer. We present a description each chapter in detail in the following paragraphs.

1.2.1 Stretching Liquid Bridges with Moving Contact Lines: Comparison of Model Predictions and Experiments

In this research, we develop two models of liquid bridge stretching and compare the resulting predictions with previously published experimental data. At relatively low stretching speeds, predictions from both models of the amount of liquid transferred agree well with the experimental data. Notably, the amount of liquid transferred is primarily governed by the overall bridge shape and is not significantly influenced by contact-line motion toward the end of bridge stretching. When the stretching speed is high enough, the models predict that each surface receives half the liquid, in agreement with experimental observations.

For intermediate values of the stretching speed, predictions from each model can

deviate substantially from the experimental data, which we speculate is due to the influence of surface defects that are not included in the models. In this regime, there can be significant differences between the predictions of the 1D and 2D models, which are due to the tendency of the contact line to slip more in the 1D model. This research provides the first systematic comparison between theory and experiment for liquid transfer in the absence of an electric field. It lays the necessary foundation for studying liquid transfer when an electric field is present.

1.2.2 Electrostatic Assist of Liquid Transfer between Flat Surfaces

In this research, the 1D model is modified to include electrostatic effects. The results show that electrostatic forces enhance liquid transfer to the more wettable surface for any stretching speed. The presence of the electric field increases the pressure difference inside the liquid bridge and drives liquid toward the more wettable surface.

The electric field also causes electric charge accumulate at the liquid-air interface. The surface charge and the electric field generate a tangential force, which can significantly increase the amount of liquid transferred. The direction of the tangential force can be adjusted by the direction of the electric field. Experimental results also confirm the enhancement of the amount of liquid transferred when the electric field is present, and the measured values are in good agreement with the predictions of the 1D model. This research provides the first systematic explanation for the physical mechanisms underlying ESA. It provides a necessary basis for extending the model to consider liquid transfer from cavities.

1.2.3 Electrostatic Assist of Liquid Transfer with Plates and Cavities

Roll-to-roll printing processes require formation and stretching of a liquid bridge to transfer liquid from one surface to another. Since inadequate liquid transfer can produce defects that are detrimental to printed products, electric fields are sometimes applied to enhance transfer, a method known as electrostatic assist (ESA). Because the physical mechanisms underlying ESA are not well understood, we examine here the influence of electric fields on liquid transfer in two model geometries, both of which involve liquid bridges with moving contact lines. The bridges are axisymmetric and confined between

two electrodes, one of which is flat and moves vertically upward, and the other which either is flat or has a cavity and is stationary. An electric field is applied in the axial direction, both perfect and leaky dielectric liquids are considered, and the governing equations are solved with the Galerkin finite-element method.

For liquid transfer between two flat plates, application of an electric field stabilizes the liquid bridge. This allows more time for the contact line to retract on the less wettable surface and leads to an increase in liquid transfer to the more wettable surface. Tangential stresses due to surface charge can significantly enhance liquid transfer, even to the less wettable surface if the tangential stresses point toward that surface. For liquid transfer between a flat plate and a cavity, the electric field increases the pressure gradient near the contact line on the cavity wall, causing the contact line to slip and more liquid to be transferred from the cavity. Notably, the effect is more pronounced for a deep cavity, resulting in a larger percentage of liquid transferred compared to a shallow cavity. In contrast to the case of liquid transfer between two flat plates, surface charge does not have as significant an influence on liquid transfer due to the way the cavity and electric field modify the interface shape near the contact line. The results of this work illustrate the physical mechanisms through which electric fields can improve liquid transfer, and provide guidance for optimizing ESA in industrial printing processes.

Chapter 2

Stretching liquid bridges with moving contact lines comparison of liquid-transfer predictions and experiments

2.1 Introduction

Printing processes play a key role in industrial manufacturing. Printing techniques are not only used for books and newspapers but they are also being developed for the production of electrical circuits [50], flexible displays [51], and solar cells [52, 53]. Because they provide a less-expensive alternative to silicon-based fabrication technologies, printing processes have great potential to dramatically reduce manufacturing costs [13, 14, 15, 24].[1]

Several key printing processes involve formation of a liquid bridge and then transfer of liquid from one surface to another, as illustrated in Figure 2.1. During liquid transfer, the liquid bridge is in general subject to shearing, extensional, and rotational motion, especially when the printing process operates in a roll-to-roll format [46]. In addition, the bounding solid surfaces may contain topographical (e.g., gravure printing) or chemical

[1] This chapter has been published in [54]

(e.g., lithographic printing) patterns. Because of the complexities involved in considering all of these factors at once, studies aimed at advancing fundamental understanding typically isolate limiting cases.

An important limiting case is the extension of a liquid bridge between two flat parallel plates where the contact lines can slip. Here, fundamental studies seek to understand how the amount of liquid transferred from one surface to the other depends on the problem parameters. The objective of the present paper is to compare predictions from models of this situation to previously published experimental observations. Below, we briefly review several of these prior studies before providing an overview of the present paper.

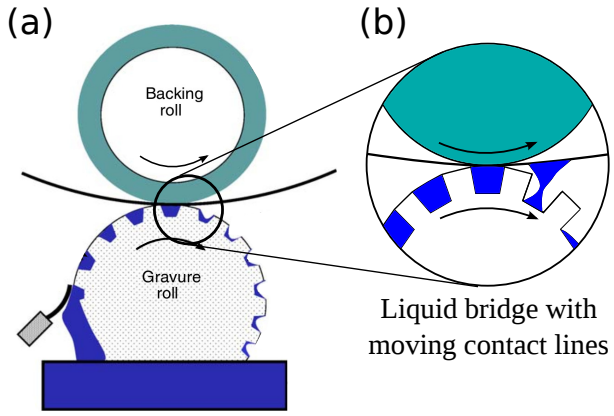

Figure 2.1: (a) Schematic of a gravure printing process. The ink in a cavity is transferred from an engraved roll to a substrate. (b) Illustration of a stretching liquid bridge.

2.1.1 Prior experimental work

As discussed in a recent review [46], there have been a number of studies focused on examining liquid transfer in the presence of extensional motion, beginning with the pioneering studies of Chadov and Yakhnin [55, 56]. Here, we review only those studies that have motivated the present work.

Chen *et al.* studied the stretching of water bridges at very low capillary numbers ($Ca \sim 10^{-7}$) [5]. The capillary number $Ca = \mu U/\sigma$ provides a measure of the ratio of viscous forces to surface-tension forces, where μ is the liquid viscosity, U is the characteristic stretching velocity, and σ is the surface tension. One (acceptor) surface

was kept the same in all the experiments while ten different materials were used for the other (donor) surface. The authors found that as the receding contact angle of the donor surface becomes larger relative to that of the acceptor surface, more liquid is transferred to the acceptor surface. These observations are in qualitative agreement with earlier finite-element simulations [57].

Chen *et al.* also measured contact radii and angles during bridge stretching, and argued that contact-angle hysteresis (CAH) plays an important role in determining the time-evolution of these quantities [5, 58, 59, 60]. Indeed, solutions of the Young-Laplace equation accounting for CAH yield predictions in good agreement with experiments [5, 58, 59, 60]. However, such calculations cannot be applied to describe experiments outside of the quasi-static regime, like those later performed by Chen *et al.* [6, 61]. Although CAH would be expected to be important in determining the behavior of local quantities such as contact radii and angles, it is not clear what influence it has on determining global quantities such as the amount of liquid transfer, which is controlled by where the bridge breaks. Comparison of dynamic calculations that neglect CAHwith the experimental data of Chen *et al.* would address this question.

Qian and Breuer performed experiments with water/glycerol bridges in which one contact line was free to move while the other was pinned [7]. They measured the radius of the droplet left on the bottom surface (where the contact line is free to move) and compared it to predictions from a one-dimensional (1D) slender-jet model. In their model, two different descriptions of the contact angle on the bottom surface were employed: (i) fixing the contact angle at its receding value, and (ii) applying an empirical equation relating contact angle to the contact-line speed [62].

The constant-contact-angle approach fails to accurately predict the time-evolution of the contact line, whereas the parameters in the empirical equation can be adjusted so that the model predictions match experimental results. While this good agreement might imply that the speed-dependence of the contact angle needs to be accounted for, another possibility is that the slender-jet model itself does not provide an accurate description of bridge behavior and the empirical law compensates for this [7, 63]. Calculations using a two-dimensional (2D) axisymmetric model with a fixed contact angle would help resolve this issue.

Gupta *et al.* [4] explored the influence of initial bridge shape through experiments

involving transfer of water and glycerol droplets from a poly(dimethyl siloxane) (PDMS) surface to a silicone surface. In one of their experiments, almost none of the water transferred to the silicone surface, which was more wettable. However, when the experiments were performed with a droplet having half the initial height and the same volume, nearly all the water transferred to the silicone.

In general, one would expect the bridge with the smaller initial height (and thus larger initial radius) to transfer more liquid since the contact lines would have more time to slip off the PDMS surface before the bridge breaks [57, 63]. However, experimental images (Figure 2(c) of Ref. [4]) indicate that the initial bridge shapes are asymmetric in the vertical direction, with the narrowest portion located near one of the plates. So, it is not clear whether this asymmetry or the different initial height is responsible for the large change in liquid transfer. Again, comparisons of the experimental observations with predictions from mathematical models could help shed light on this matter.

2.1.2 Overview of present paper

Motivated by the above experimental observations, we present in this paper results from 2D axisymmetric simulations of stretching liquid bridges with moving contact lines. Although similar simulations have been conducted previously [57, 63, 64], they were not performed in a parameter regime where the results could be quantitatively compared to the experimental observations discussed above. We also present in this paper results from calculations using a 1D slender-jet model, which is much less computationally demanding, to ascertain how well this simpler 1D approach can describe the experimental data. In addition to being relevant to printing processes, the results of this work are also important for other applications such as adhesion, tribology, microfluidics, and self-assembly [46, 65].

The mathematical models used in this paper are developed in section 2. Comparisons with the experiments of Chen *et al.* [5, 6] and Qian and Breuer [7] are made in sections 3 and 4, respectively. The influence of initial bridge shape (which has not been systematically studied in prior simulations) is examined in section 5, and comparisons are made to the experiments of Gupta *et al.* [4]. Concluding remarks are given in section 6.

2.2 Problem formulation

2.2.1 Governing equations

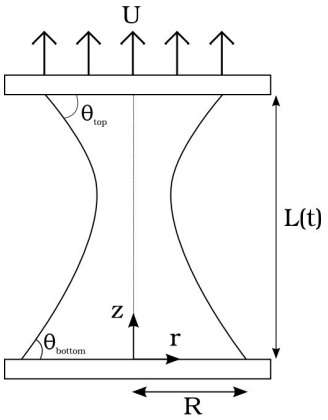

Figure 2.2: Schematic of liquid bridge and coordinate system. Note that $L(t=0) \equiv L$.

We consider an axisymmetric bridge of a Newtonian liquid with constant volume V, density ρ, viscosity μ, and surface tension γ (Figure 2.2). The bridge is confined between two plates, and we denote the initial bridge length by L and characteristic radius by R. The top plate is given a constant velocity U in the z-direction while the bottom plate is kept stationary. The contact angle for the bottom plate is θ_{bottom} and that for the top plate is θ_{top}. Although these angles could, in principle, depend on contact-line speed, we study here the limiting case where they are constants.

Scaling length by R, velocity by U, time by R/U, and pressure by $\mu U/R$, the dimensionless Navier-Stokes equations are:

$$\nabla \cdot \mathbf{v} = 0, \tag{2.1}$$

$$Re(\frac{\partial \mathbf{v}}{\partial t} + \mathbf{v} \cdot \nabla \mathbf{v}) = -\nabla P + \nabla^2 \mathbf{v}, \tag{2.2}$$

where $\mathbf{v}$ is the velocity, P is the pressure, and $Re = \rho U R/\mu$ is the Reynolds number.

At the liquid-air interface, the kinematic boundary condition holds:

$$\mathbf{n} \cdot (\mathbf{v} - \dot{\mathbf{x}}) = 0, \tag{2.3}$$

where $\mathbf{n}$ is outward unit normal to the interface and $\dot{\mathbf{x}}$ is the interface velocity.

The stress balance at the interface is:

$$\mathbf{n} \cdot \mathbf{T} = -\frac{\kappa}{Ca}\mathbf{n}, \tag{2.4}$$

where $\mathbf{T}$ is stress tensor, $Ca = \mu U/\gamma$ is the capillary number, $\kappa = \nabla_s \cdot \mathbf{n}$ is the interfacial curvature, $\nabla_s = (\mathbf{I} - \mathbf{nn}) \cdot \nabla$ is the surface gradient operator, and $\mathbf{I}$ is the identity tensor. The dynamics of the gas surrounding the liquid bridge are neglected.

To handle the dynamic contact lines, we apply a Navier slip condition and assume a constant contact angle:

$$\mathbf{t}_{wall} \cdot (\mathbf{n}_{wall} \cdot \mathbf{T}) = \frac{1}{\beta}\mathbf{t}_{wall} \cdot (\mathbf{v} - \mathbf{v}_{wall}), \tag{2.5}$$

$$\mathbf{n}_{wall} \cdot \mathbf{n} = \cos\theta, \tag{2.6}$$

where $\mathbf{n}_{wall}$ (which points toward the liquid side) and $\mathbf{t}_{wall}$ are vectors normal and tangent to the solid surfaces, $\mathbf{n}$ is the outward unit normal to the liquid-air interface, β is a dimensionless slip coefficient, and $\mathbf{v}_{wall}$ is the wall velocity. Here θ is equal to θ_{bottom} or θ_{top} depending on the plate under consideration. A no-penetration condition is applied at the solid surfaces:

$$\mathbf{n} \cdot \mathbf{v} = \begin{cases} 0 & \text{for } z = 0 \\ 1 & \text{for } z = L(t), \end{cases} \tag{2.7}$$

where $\mathbf{n}$ is the normal vector pointing in the z-direction and $L(t)$ denotes the location of the top plate.

2.2.2 2D axisymmetric model

In our 2D axisymmetric model, we solve equations (2.1) - (2.7) using the Galerkin finite-element method. As in our previous work [57, 63], we set $\beta = 10^{10}$ to produce a stress-free contact line that is free to slip (the results are independent of the value of β down to $\beta = 0.1$). Equations (2.5) and (2.6) are only applied at the node which is on the contact line and the no-slip condition is applied elsewhere; this corresponds to having a slip length less than the element size [57, 63].

Elliptic mesh generation is used to track the moving interface. The first three time steps are taken with a first-order backward Euler method to avoid abrupt oscillations;

the trapezoid rule with adaptive time-stepping is applied afterward [66]. When the liquid bridge is about to break, a thin liquid thread connecting droplets on each plate is formed. The computation is ended when the elements in the thread become excessively long and overlapped, which is usually when the minimum bridge radius is $O(10^{-3})$.

To ensure mass conservation, we also track the variation of volume, V_{var} =100(V_{max}-V_{min})/V_{ini}, where V_{max}, V_{min}, and V_{ini} are the maximum, minimum, and initial volumes of the liquid bridge. When the value of V_{var} is less than 0.1%, the variation of the final bridge radius and bridge shape is generally negligible as the mesh and time step are refined. If the value of V_{var} is larger than 0.1%, we refine the mesh or time step, repeat the simulation, and continue this procedure until V_{var} is less than 0.1% [57].

2.2.3 1D slender-jet model

To complement the 2D axisymmetric model, we also perform calculations with a much simpler slender-jet model. Previous work indicates that predictions from this 1D model agree qualitatively, and in some cases quantitatively, with predictions from the 2D axisymmetric model [63].

The liquid bridge radius is assumed to be much smaller than its length, so that their ratio defines a small parameter ϵ. An asymptotic expansion is then performed on the axial velocity v and pressure P:

$$v(r,z,t) = v_o(z,t) + (\epsilon r)v_1(z,t) + (\epsilon r)^2 v_2(z,t) + \cdots , \tag{2.8}$$

$$P(r,z,t) = P_o(z,t) + (\epsilon r)P_1(z,t) + (\epsilon r)^2 P_2(z,t) + \cdots . \tag{2.9}$$

The radial dependence is given explicitly in the expansion, so the correction functions of both variables only depend on the axial coordinate and time.

Equations (2.8) and (2.9) are substituted into into equations (2.1),(2.2),(2.3), and (2.4) to obtain leading-order equations [67]. After dropping the subscripts "o" for clarity, these equations are:

$$Re(v_t + vv_z) = -\frac{1}{Ca}\kappa_z + \frac{3}{h^2}(h^2 v_z)_z, \tag{2.10}$$

$$h_t = -vh_z - \frac{1}{2}v_z h, \tag{2.11}$$

where h is the position of liquid-air interface and κ is the interfacial curvature,

$$\kappa = \frac{1}{h(1+h_z^2)^{\frac{1}{2}}} - \frac{h_{zz}}{(1+h_z^2)^{\frac{3}{2}}}. \tag{2.12}$$

The indices t and z indicate differentiation with respect to those variables. Note that the full curvature is retained to obtain a more accurate description of the interface [31, 63, 67, 68, 69, 70].

Equations (2.10), (2.11), and (2.12) are solved with a finite-element method [63, 69]. To lower the highest-order derivative in those equations, a new variable Ω is introduced:

$$\Omega - \frac{\partial h}{\partial z} = 0. \tag{2.13}$$

The no-penetration boundary condition is

$$v(z=0,t) = 0, v(z=L(t),t) = 1. \tag{2.14}$$

The contact angle appears through a geometric relation:

$$\Omega = \frac{\partial h}{\partial z} = \cot(\theta), \tag{2.15}$$

where θ is θ_{top} or θ_{bottom}. The slip law does not appear at leading order and so cannot be imposed [63]. However, the contact line is still free to slip, allowing for consistent comparison of results with those from the 2D axisymmetric model [63]. As with those calculations, we monitor the variation of volume to ensure convergence of results.

2.2.4 Parameter values

The values of various dimensionless parameters characterizing the experiments discussed in section 1.1 are shown in Table 1. The small values of the Bond number suggest that gravitational effects can be neglected, as we have done in the equations above. The small values of the Reynolds number and Weber number suggest that inertial forces can be neglected, and in what follows we set $Re = 0$. We thus focus on the influence of the capillary number and initial aspect ratio of the bridge.

2.3 Comparison to experiments of Chen *et al.*

In this section, we compare model predictions with the experimental observations of Chen *et al.* described in section 1.1. We first consider the quasi-static experiments [5]

Table 2.1: Dimensionless problem parameters. The Bond number is denoted by Bo, the Weber number by We, and the initial aspect ratio of the bridge by Λ.

Parameter	Definition	Physical meaning	Value
Bo	$\rho g R^2/\gamma$	Gravitational forces/Surface-tension forces	$10^{-2} - 10^{-1}$
Re	$\rho U R/\mu$	Inertial forces/Viscous forces	$10^{-3} - 10^{-1}$
Ca	$\mu U/\gamma$	Viscous forces/Surface-tension forces	$10^{-7} - 10^{1}$
We	$\rho U^2 R/\gamma$	Inertial forces/Surface-tension forces	$10^{-9} - 10^{-1}$
Λ	$L/2R$	Initial bridge length/Initial bridge diameter	0.1 - 1

(relatively low stretching speeds), and then turn to the dynamic experiments [6] (higher stretching speeds).

2.3.1 Quasi-static experiments

The experiments conducted by Chen *et al.* at relatively low stretching speeds ($\sim$5 $\mu m/s$) [5] have Ca values of $O(10^{-7})$. We refer to this as the quasi-static regime. As discussed in section 1.1, an open issue regarding these experiments is the extent to which dynamic calculations that neglect CAH can accurately describe the experimental data. Since such dynamic calculations can also be applied to study liquid transfer at higher Ca, simulations of the quasi-static regime also represent an important validation step.

One of the important challenges in conducting dynamic simulations at very low capillary numbers is the vast separation between the convective time scale L/U and the capillary time scale $\sigma/\mu L$. This separation makes the dynamic equations very stiff, and as a consequence, limits the lowest value of Ca we can simulate to $O(10^{-3})$.

To overcome this limitation, we use an extrapolation procedure. The 2D axisymmetric model is used to determine the relationship between the transfer ratio (percentage of liquid transferred to the top plate) and Ca. The transfer ratio is determined by identifying the narrowest point of the bridge at the end of a simulation, and assigning all the liquid above that point to the top plate and all the liquid below to the bottom plate.

Figure 2.3 shows the results of such calculations for the case where the contact angle at the top plate is set to $\theta_{\text{top}} = 60^\circ$ (approximately equal to the receding contact angle in the experiments) while the values of the contact angle at the bottom plate are varied from 40° to 60° (these are assumed to be receding contact angles). The

initial condition of the bridge is taken to be a cylinder with a height equal to half the diameter (the contact angles achieve their prescribed values after the first time step of the simulation). We denote the difference between the contact angles of the bottom and top plates by $\Delta\theta_r$, where θ_r denotes receding contact angle and positive values mean that the bottom plate has a higher contact angle.

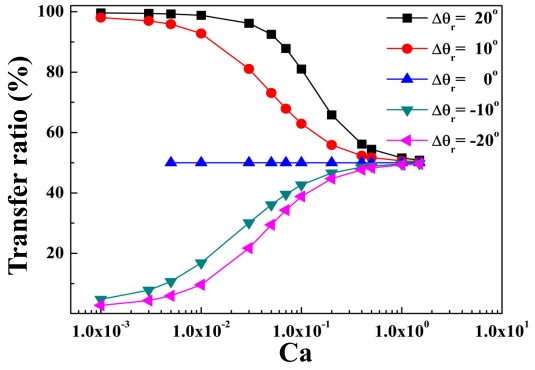

Figure 2.3: Relationship between liquid transfer ratio and Ca for different values of $\Delta\theta_r$. Here θ_{top}=60° and θ_{bottom} is varied.

Figure 2.3 shows that when $\Delta\theta_r = 0$, the transfer ratio is 50% for all Ca as expected (since the liquid does not preferentially wet either plate). In addition, for all values of $\Delta\theta_r$, the transfer ratio approaches 50% as Ca increases, which corresponds to viscous forces becoming stronger and reducing the influence of wettability differences. It can also be seen that the transfer ratio decreases as Ca increases when $\Delta\theta_r$ is positive, and increases as Ca increases when $\Delta\theta_r$ is negative. These trends reflect the observation that liquid will transfer to the more wettable surface, with the effects of wettability differences being more pronounced at low Ca.

When Ca is less than ~0.01, the transfer ratio reaches a plateau, which corresponds to the quasi-static regime. Here, the transfer ratio varies very slowly and approximately linearly with Ca. We can then use a linear relationship and extrapolate to low capillary numbers to predict the transfer ratio at values of Ca characteristic of the experiments. If the extrapolation shows 100% liquid transfer at values of Ca larger than in the experiments, then we assume a prediction of 100% transfer. The same strategy is used to generate predictions from the 1D model.

Calculations like those shown in Figure 2.3 were performed using initial bridge aspect

ratios and values of $\Delta\theta_r$ similar to those in the experiments. The predicted values of the transfer ratio from the 2D and 1D models are shown in Figure 2.4(a), along with the experimental values [5]. The transfer ratio increases as $\Delta\theta_r$ increases until it reaches 100%. As can be seen, both models predict the transfer ratio very well when $|\Delta\theta_r| > 10°$. For values of $|\Delta\theta_r| < 10°$, the calculations overestimate the transfer ratio when $0° < \Delta\theta_r < 10°$ and underestimate it when $-10° < \Delta\theta_r < 0°$.

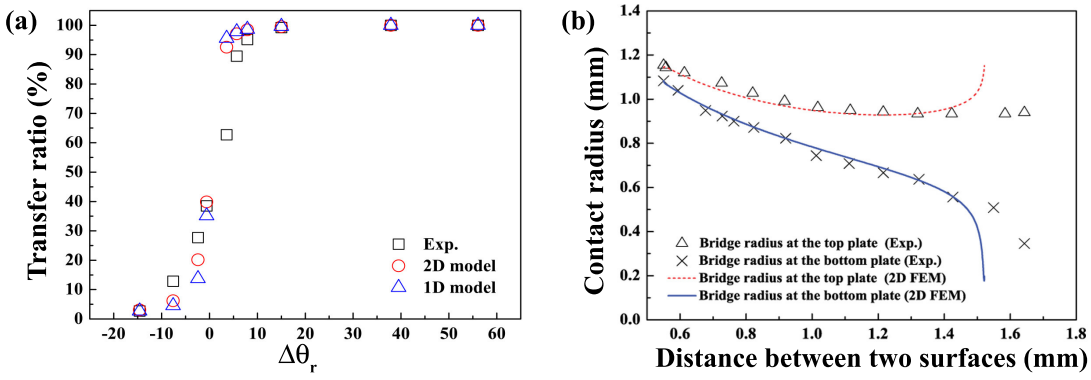

Figure 2.4: (a) Comparison of predicted liquid transfer ratios with experimental results [5]. (b) Position of the contact lines on both surfaces during the stretching process for case 8 in Ref. [5] where $\Delta\theta_r = 15°$. For the simulations, Ca=10^{-3}.

For $|\Delta\theta_r| < 10°$ (where the discrepancies between theory and experiment are largest), liquid transfer may be very sensitive to surface heterogeneities, which are not included in the models. Differences in initial conditions between the calculations and experiments probably play a lesser role since calculations using an equilibrium bridge as an initial condition give the same transfer ratio.(Such initial conditions are obtained by setting the velocity of the top plate to zero and running a simulation until a steady state is reached.) In addition, the transfer ratio is very sensitive to the value of $|\Delta\theta_r|$ in this regime (relative to when $|\Delta\theta_r| > 10°$). Small errors (which may be caused by surface heterogeneities) in the measured contact angles relative to their actual values could thus lead to large deviations between predicted and measured transfer ratios since the models use the measured contact angles as an input.

We also note that since the receding contact angles from the experiments are used in the calculations, it is these contact angles that largely govern liquid transfer, consistent with the observation of Ref. [5]. Since our calculations do not incorporate contact-angle

hysteresis, we conclude that CAH is not always important for predicting the amount of liquid transferred in the quasi-static experiments of Chen *et al.* [5], except perhaps when $|\Delta\theta_r|$ is small enough to make surface heterogeneities very important.

For values of $|\Delta\theta_r| < 10^\circ$, the 2D model appears to yield slightly better predictions of the transfer ratio than the 1D model (Figure 2.4(a)). In general, the 1D model predictions show more retention or transfer of liquid than the 2D model when $\Delta\theta_r$ is negative or positive, respectively. This difference is due to differences in contact-line motion predicted by the models. As discussed in previous work [63], the contact line tends to move more in the 1D model, and this leads to underestimates or overestimates of the transfer ratio relative to what the 2D model predicts.

To further study the influence of contact-line motion on liquid transfer, we compare predictions of contact-line motion on both plates with experimental observations in Figure 2.4(b). Since the 2D model tends to give more accurate predictions of contact-line motion (as noted above), we use it to generate the predictions. The experimental observations correspond to case 8 in Ref. [5], where $\Delta\theta_r = 15^\circ$. The initial condition for this simulation is a liquid bridge that has the same volume and initial radii as in the experiments (This initial condition produces the same transfer ratio as that obtained when starting from a cylindrical bridge.)

Figure 2.4(b) shows that the contact radius on the bottom plate keeps decreasing during the experiments, whereas the contact radius on the top plate becomes approximately constant toward the end of the experiments. The 2D model predicts the position of the contact line on both plates well only when the distance between the plates is less than $\sim$1.4 mm. Beyond this point, the model predicts that the contact lines move much more rapidly than they do in the experiments. As a consequence, the model predicts that the bridge stretches to a shorter maximum length ($\sim$1.5 mm) than the experimental value ($\sim$1.65 mm).

However, this discrepancy does not have a large effect the transfer ratio: the model prediction (99.51%) is very close to the experimental result (99.23%). When the contact radius on the bottom plate shrinks fast at the end of the stretching, the liquid bridge breaks near the bottom plate. Therefore, most of the liquid is transferred to the top plate and the exact values of the contact radii at this late time have only a minor influence on the amount of liquid transferred. In cases like this where the contact line on one

of the plates keeps moving throughout the entire transfer process, CAH is expected to also play a minor role.

While accurately describing the contact-line motions on both plates may not be critical for correctly predicting the amount of liquid transferred, it is important for correctly predicting the adhesion force, which depends strongly on the contact radii on both plates. Indeed, while our model generally predicts values of the adhesion force of the same order of magnitude observed in the experiments [5], the agreement is typically not as good as seen with the transfer ratio (results not shown). To obtain better predictions, it may be necessary to account for the speed-dependence of the contact angles, which may prevent the rapid changes in contact-line position that occur near bridge breakup when a constant contact angle is assumed (Figure 2.4(b)).

2.3.2 Dynamic experiments

We now turn to the dynamic experiments of Chen *et al.* [6]. Figure 2.5 shows the experimentally measured transfer ratio as a function of Ca for four different experiments. The top plate in these experiments is a surface coated with poly(ethyl methacrylate) (PEMA) ($\theta_r = 61.7°$). The bottom plate in each panel is a surface coated with (a) Teflon ($\theta_r = 106.7°$), (b) octadecyltrichlorosilane (OTS) ($\theta_r = 83.9$), and (c) polystyrene (PS) ($\theta_r = 56.6$), and (d) a silicon surface ($\theta_r = 37.3$). Also shown are predictions from the 1D and 2D models, with initial conditions similar to the experiments (initial bridge length of 0.45 mm and same initial volume).

Figure 2.5(a) shows the case of liquid transfer from Teflon to PEMA, where $\Delta\theta_r = 45°$. Predictions from both models agree well with the experimental values at low Ca (< 0.03), as might be expected from the results of section 3.1. For the intermediate value of $Ca = 0.2$, both models overpredict the transfer ratio by a considerable amount. For $Ca = 2$, the prediction from the 2D model is much closer the experimental value of 50%, whereas the 1D model still predicts that all of the liquid is transferred to the PEMA-coated plate.

Figure 2.5(b) shows the case of liquid transfer from OTS to PEMA, where $\Delta\theta_r = 22.2°$. Here, behavior similar to that shown in figure 2.5(a) is observed. At low Ca, the models yield predictions close to the experimental values, but at intermediate Ca, their predictions worsen. At $O(1)$ values of Ca, the 2D model again yields predictions closer

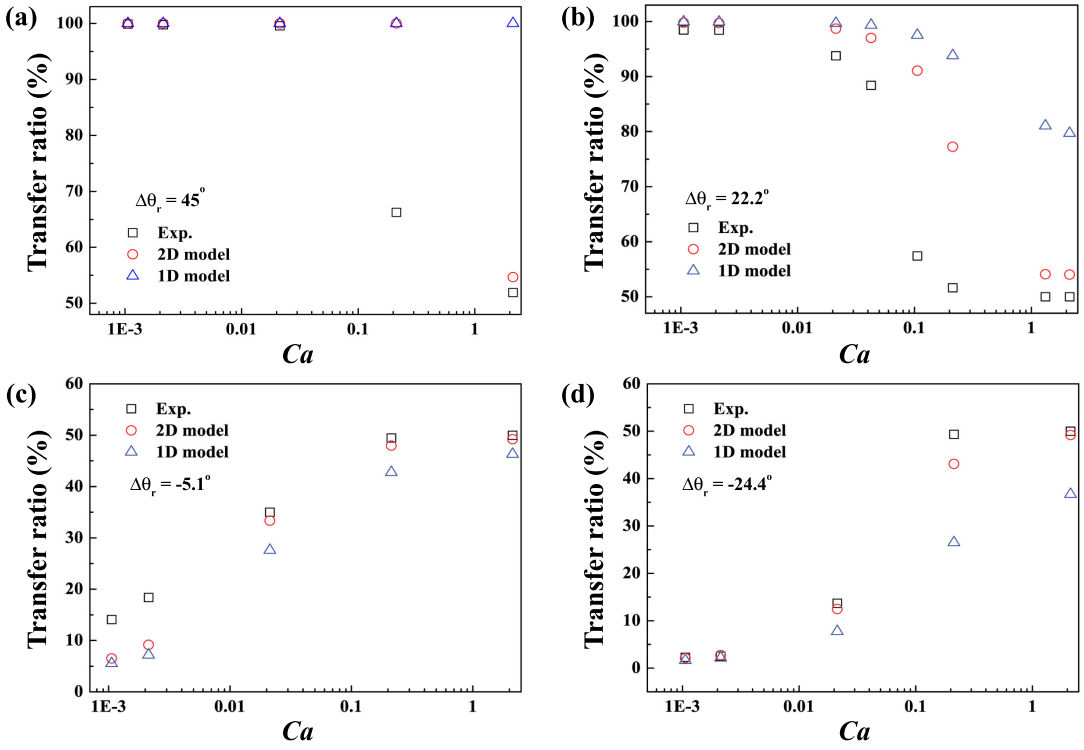

Figure 2.5: Comparison of predicted liquid transfer ratios with experimental results [6]. (a) Transfer from Teflon (θ_r=106.7) to PEMA (θ_r=61.7). (b) Transfer from OTS (θ_r=83.9) to PEMA. (c) PS (θ_r=56.6) to PEMA. (d) Transfer from silicon (θ_r=37.3) to PEMA.

to the experimental values of 50%.

Figure 2.5(c) shows the case of liquid transfer from PS to PEMA, where now $\Delta\theta_r = -5.1°$. At low Ca, both models underpredict the amount of liquid transfer. The worse agreement here at low Ca relative to the previous two cases might be expected based on the results of section 3.1, where the most disagreement was seen for relatively small contact-angle differences. As Ca increases, the predictions from the 2D model come closer to the experimental results and approach 50%. Again, the predictions from the 1D model are not as good in this regime.

Figure 2.5(d) shows the case of liquid transfer from silicon to PEMA, where $\Delta\theta_r = -24.4°$. As with the cases in panels (a) and (b), both models yield predictions in good agreement with the experimental values at low Ca, with the agreement worsening at intermediate Ca. At $O(1)$ values of Ca, the 2D model yields predictions in good agreement with the experimental values, whereas the predictions from the 1D model are not as good.

From the above panels, we see that both models yield predictions in good agreement with the experimental data at low Ca provided that $|\Delta\theta_r|$ is sufficiently large. If $|\Delta\theta_r|$ is small enough, the model predictions are still consistent with each other but differ from the experimental values, as also observed in section 3.1.

As noted in section 3.1, the 1D and 2D models make different predictions of the contact-line motion for the same initial conditions. At low Ca, where liquid transfer is primarily governed by wettability differences, the different predictions of contact-line motion do not lead to significantly different predictions of the transfer ratio.

As Ca increases, viscous forces become stronger relative to surface-tension forces, and thus wettability differences. As a consequence, the differences in predicted contact-line motion become more influential, and the 1D and 2D models can yield very different predictions of the transfer ratio (Figure 2.5). As seen in figure 2.5, the 1D model tends to overpredict the transfer ratio relative to the 2D model when $\Delta\theta_r > 0$ and underpredict it when $\Delta\theta_r < 0$ (similar behavior was also observed in Figure 2.4(a)). The 1D model neglects radial variations in the problem variables, but the 2D model shows that near the contact lines there are strong radial pressure gradients. Since the 1D model neglects any viscous dissipation due to these radial pressure gradients, it predicts greater contact-line movement, and as a consequence, more transfer or retention of liquid relative to the 2D

model.

At $O(1)$ values of Ca, the viscous forces become strong enough to overcome the effects of wettability differences and the transfer ratio approaches 50%. The 2D model correctly predicts this limit, as seen in figure 2.5. The 1D model sometimes gets close to this limit (Figure 2.5(c) and (d)), but in other cases it does not (Figure 2.5(a) and (b)). For the latter cases, the 1D model predicts that the contact line on the bottom plate retracts more quickly relative to what the 2D model predicts, yielding the result that most of the liquid to transfers to the top plate.

The largest discrepancies between the predictions of the 2D model and the experimental values tend to occur at intermediate values of Ca (except when $|\Delta\theta_r|$ is small enough, as noted earlier (Figure 2.5 (c))). In this regime, neither wettability differences nor viscous forces are dominant, so we suspect that liquid transfer may be very sensitive to surface heterogeneities (similar to the case of low Ca and small enough values of $|\Delta\theta_r|$, discussed in section 3.1). It is also possible that three-dimensional effects may come into play, and these are not accounted for in our model.

2.4 Comparison to experiments of Qian and Breuer

In this section, we compare model predictions with the experimental observations of Qian and Breuer [7] described in section 1.1. Because of the low capillary numbers in these experiments (3×10^{-4} to 8×10^{-4}), we use if needed an extrapolation procedure similar to that described in section 3.1 to determine the transfer ratio and the radius of the droplet deposited on the bottom plate (where the contact line is free to slip and $\theta_r = 85°$). The initial condition is a liquid bridge in the shape of a cylinder with the same volume as used in the experiments and a radius equal to that of the top plate (where the contact line is pinned).

Figure 2.6 shows the radius of the droplet deposited on the bottom plate as a function of the speed U of the top plate for several different bridge volumes V. The largest speed (600 μm/s) corresponds to $Ca = 8 \times 10^{-4}$, which is the smallest Ca value we were able to simulate. The experimental data show that the droplet radius increases with the speed of the top plate and the droplet volume. The simulation results also predict an increase in droplet radius with droplet volume but a much weaker dependence on U.

Notably, the 2D model always underpredicts the radius of the deposited droplet.

Although not shown here for brevity, the 1D model yields values of the droplet radius that are slightly smaller than the predictions from the 2D model. Qian and Breuer also observed that the 1D model with a constant contact angle underpredicts the experimentally observed droplet radii [7]. Given that the 2D model underpredicts the experimental observations as well, the failure of the 1D model is likely not due to the geometrical approximations it makes. We will return to this issue below when discussing the time-evolution of the contact line.

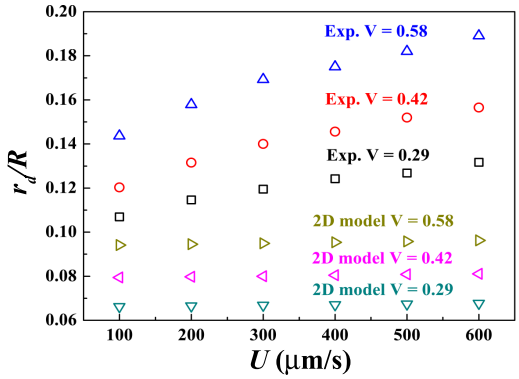

Figure 2.6: Radius of droplet deposited on bottom plate r_d non-dimensionalized with the radius of the top plate R as a function of the speed of the top plate U. The dimensionless bridge volume is $V = v/\pi\ R^3$, where v is the dimensional volume. The experimental data are from Figure 9 of Ref. [7].

While the 2D model underpredicts the droplet radii, this does not necessarily imply that it will make poor predictions of the amount of liquid transferred. Although Qian and Breuer [7] do not report values of the amount of liquid transferred, they do show one image after bridge breakup in which droplets rest on the top and bottom plates (Figure 2 of Ref. [7], where $U = 100$ μ/s and $V = 0.42$). Using a spherical-cap approximation to estimate the volume of the droplets yields a transfer ratio of 99.55%, i.e., most of the liquid transfers to the top plate. The 2D and 1D models predict that the transfer ratio is 99.96% and 99.80%, respectively. Thus, although the models underestimate the radius of the droplet on the bottom plate, they predict the transfer ratio well.

To better understand this behavior, we show in Figure 2.7(a) the droplet radius (i.e., contact-line position) on the bottom plate as a function of bridge length. The model

predictions are for $Ca = 8 \times 10^{-4}$ (the lowest value we can simulate), which is larger than the value in the experiments by a factor of six (corresponding experimental data for larger values of Ca are not reported). Despite this discrepancy, both models predict the evolution of the droplet radius well until close to bridge breakup, where the radius decreases rapidly with bridge length. The models predict a smaller radius at breakup than what is observed experimentally, consistent with the results of Figure 2.6.

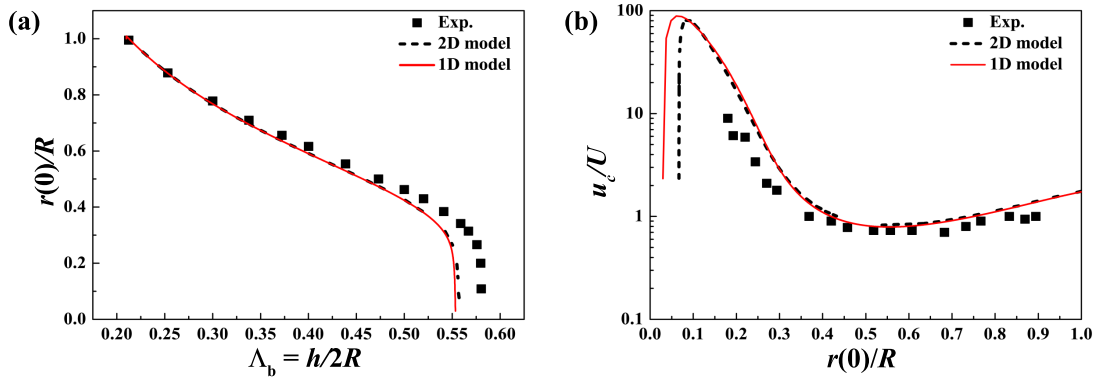

Figure 2.7: (a) Droplet radius (contact-line position) on bottom plate $r(0)$ versus bridge height h. Both quantities are non-dimensionalized using the radius of the top plate R. Experimental data are from Figure 2 of Ref. [7], where $U = 100$ μm/s. (b) Contact-line velocity u_c as a function of contact-line position. Here, U is the velocity of the top plate (600 μm/s). Note that increasing time corresponds to decreasing $r(0)$. Experimental data are from Ref. [7].

In Figure 2.7(b), we show the contact-line velocity on the bottom plate as a function of contact-line position. Here, experimental data are reported for $Ca = 8 \times 10^{-4}$, so we show it and the corresponding model predictions. The calculations are started when the dimensionless contact-line position is unity (right-end of x-axis). For relatively low contact-line speeds, both models yield predictions in good agreement with experimental data.

Close to bridge breakup, the models predict that the contact-line speed increases rapidly before suddenly dropping. The predicted speeds in this regime are much larger than what is observed experimentally. (A similar phenomenon was seen in Figure 2.4(b).) These larger speeds are the reason the predicted droplet radius is smaller than the experimental value (Figure 2.7(a)). Note that the 1D model predicts a larger contact-line speed and thus a smaller droplet radius than the 2D model.

The good agreement between the predictions of the 1D and 2D models shown in Figure 2.7 again indicates that the failure of the 1D model observed by Qian and Breuer [7] is likely not due to the geometrical approximations it makes. Most of the discrepancy between the model predictions and experimental data occurs toward the end of stretching. To accurately describe contact-line motion in this regime (where the contact-line velocity rapidly increases), it may well be necessary to account for the speed-dependence of the contact angle as pointed out by Qian and Breuer [7].

However, as noted above, accurate predictions of the transfer ratio can still be made by models that assume a constant contact angle. The transfer ratio appears to be primarily governed by the overall bridge shape, particularly the position where the bridge breaks. Because the models accurately predict the contact-line position and speed (and thus bridge shape) during the earlier stages of stretching where the overall bridge shape is largely set, the discrepancy toward the end of stretching does not have much of an influence on the overall bridge shape and the transfer ratio.

2.5 Effect of initial bridge shape

As noted in section 1.1, the experiments of Gupta *et al.* [4] show that the initial shape of the liquid bridge can have a significant influence on liquid transfer. Although there have been previous computational studies of liquid transfer, the influence of initial bridge shape has not been systematically explored [46, 57]. In this section, we first present results from a brief parametric study highlighting the influence of initial bridge shape, then make comparisons between model predictions and the experimental observations of Gupta *et al.* [4].

2.5.1 Parametric study

For our parametric study, the initial shape of the bridge is taken to be a cylinder with length L and radius R. The cylinder aspect ratio is given by $\Lambda = L/2R$. Increasing Λ corresponds to increasing the initial length while keeping the initial radius fixed. Although the bridge volume increases as Λ does, we can isolate the effect of initial bridge length on the transfer ratio. Because the 2D model is more accurate, we only report in this section results obtained using that model.

Figure 2.8(a) shows the transfer ratio (percentage of liquid transferred to top plate) for the case where the contact line on the top plate is pinned and the contact line on the bottom plate is free to slip. Here, we have set $Ca = 0.1$ and varied θ_{bottom} over a wide range of values. As θ_{bottom} increases, the transfer ratio increases too, reflecting the tendency of more liquid to transfer from the bottom plate as it becomes less wettable. As Λ increases, the transfer ratio decreases, except at relatively large values of θ_{bottom} ($> \sim 100°$) where nearly all the liquid transfers to the top plate.

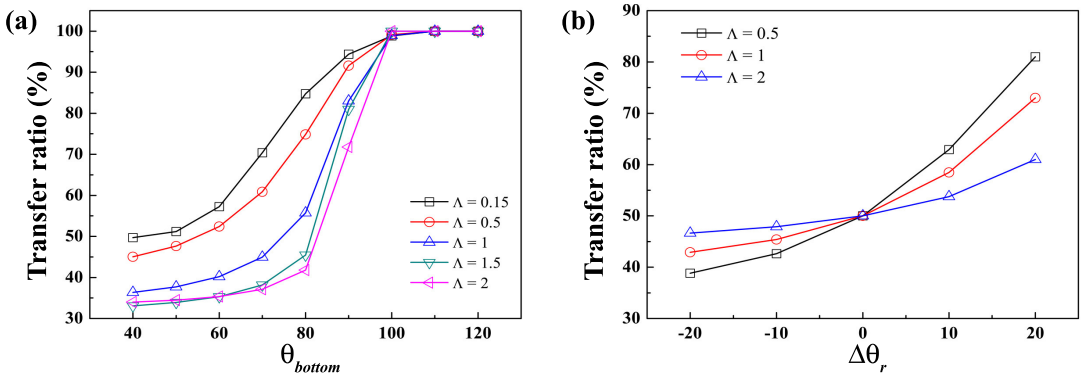

Figure 2.8: (a) Transfer ratio as a function of θ_{bottom} for different bridge aspect ratios Λ. Here, the contact line on the top plate is pinned. (b) Transfer ratio as a function of $\Delta\ \theta_r = \theta_{\text{bottom}}$ - θ_{top} for different bridge aspect ratios Λ. Here, $\theta_{\text{bottom}} = 60°$. For all the calculations in this figure, $Ca = 0.1$.

The decrease in the transfer ratio as Λ increases can be rationalized by recognizing that there is a competition between bridge breakup and contact-line spreading. The Rayleigh-Plateau stability limit for a cylindrical column corresponds to $\Lambda = \pi$ [71, 72], suggesting that longer bridges will break up sooner (We note that for liquid bridges, the stability criteria are more complicated than the Rayleigh-Plateau result and must be determined numerically in general [73, 74, 75].)

For values of θ_{botttom} less than $\sim 80°$ the liquid tends to spread on the bottom surface. The sooner the bridge break breaks, the less time there is for the liquid to spread and the transfer ratio is lower. For values of θ_{bottom} greater than $\sim 90°$, the liquid tends to retract on the bottom surface. Here, the bridge tends to break near the bottom surface, so increasing the initial bridge length does not have as strong an influence on the transfer ratio.

Figure 2.8(b) shows the transfer ratio for the case where the contact line is allowed to slip on both surfaces. Here, $\theta_{\text{bottom}} = 60^\circ$ while θ_{top} is varied. If $\Delta\ \theta_r = \theta_{\text{bottom}}$ - $\theta_{\text{top}} < 0$, then increasing Λ causes an increase in the transfer ratio. In this situation, the bridge breaks sooner as Λ increases, leaving less time for the liquid to spread on the (more wettable) bottom surface. As a result, more liquid is transferred to the top surface. Conversely, if $\Delta\theta_r = \theta_{\text{bottom}}$ - $\theta_{\text{top}} > 0$, increasing Λ causes a decrease in the transfer ratio. Again the bridge breaks sooner as Λ increases, but now there is less time for the liquid to slip off the (less wettable) bottom surface. Therefore, to transfer more liquid from a more (less) wettable to surface to a less (more) wettable surface, longer (shorter) initial bridges are beneficial.

We make several other observations related to Figure 2.8(b). First, increasing Λ drives the transfer ratio closer to 50% over the entire range of $\Delta\theta_r$. As Λ increases, the bridge breaks more quickly, leaving less time for wettability differences to be effective. Second, results of other runs we have performed but not shown here indicate that increasing Ca will also drive the transfer ratio closer to 50%. In this case, the increasing strength of viscous forces relative to surface-tension forces as Ca increases makes wettability differences less important [57]. Similarly, decreasing the value of Ca increases the effect of wettability differences. Third, calculations using an equilibrium bridge as an initial condition were performed.

With these initial bridge shapes, the narrowest point in the bridge occurs near the more hydrophobic surface, so the bridge tends to break there first. As a result, relative to the case of a cylindrical initial condition, the transfer ratio is smaller when $\Delta\theta_r < 0$ and larger when $\Delta\theta_r > 0$. Making the value of Λ large enough again pushes the transfer ratio closer to 50%.

2.5.2 Comparison to experiments of Gupta *et al.*

As discussed in section 1.1, one of the experiments performed by Gupta *et al.* [4] involved studying transfer of a water droplet (1.7 μL) from a PDMS surface ($\theta_r = 85^\circ$) to a silicone surface ($\theta_r = 65^\circ$). The speed of the top (silicone) plate was 50 μm/s, which corresponds to a value of $Ca \sim 7 \times 10^{-7}$. When the initial droplet height was 1 mm, almost none of the water transferred to the silicone, which was more wettable. However, when the droplet was compressed so its initial height was 0.5 mm, nearly all

the water transferred tothe silicone.

The greater transfer observed for the smaller initial height could simply be due its larger initial radius (since the volume is constant), which allows more time for the contact line to slip off the PDMS before the bridge breaks. But it could also be due to asymmetry in the initial bridge shape, which can be seen in the experimental images (Fig. 2(c) of Ref. [4]). The bridge with the 1 mm initial height has its narrowest portion near the top (silicone) plate, whereas the bridge with the 0.5 mm initial height has its narrowest portion near the bottom (PDMS) plate.

To better understand these experimental observations, we performed simulations with both the 1D and 2D models. In the simulations, we set $Ca = 0.001$ for computational efficiency as discussed earlier (section 3.1). Although this is larger than the value in the experiments, based on our results in earlier sections we expect that this difference will not have a significant effect on the amount of liquid transferred because Ca is still small enough to be in the quasi-static regime. For initial conditions, we used both perfect cylinders and equilibrium shapes.

Both the 1D and 2D simulations predict that nearly 100% of the liquid is transferred to the silicone surface for each initial condition whether the initial height is 1 mm or 0.5 mm. The predictions for the 0.5 mm initial height are consistent with the experiments, but the predictions for the 1 mm initial height are opposite to what is observed.

As noted above, the experimental images show that the bridge with the 1 mm initial height has its narrowest portion near the silicone surface. We suspect that this is caused by surface defects that pin the contact line and prevent it from further spreading on the top plate. As a consequence, the initial radius on the top plate is narrower than that on the bottom plate in the experiments. During the bridge stretching experiments, the contact line on the top plate actually recedes. The bridge breaks near the top plate and very little liquid is transferred there. Indeed, if we use a highly distorted initial condition in the simulations where the initial radius on the silicone is much smaller than that on the PDMS, we find that almost none of the liquid will transfer to the silicone when the initial height is 1 mm, consistent with the experiments.

Gupta *et al.* also performed experiments examining the influence of contact angle, initial volume, and stretching speed (Figs. 2(a), (b), and (d) of Ref. [4]). In some of these experiments, most of the liquid transfers to the top plate even though the initial

bridge shape is narrowest near the top plate. In other experiments, most of the liquid remains on the bottom plate. Results from corresponding simulations we have performed show that nearly all the liquid should transfer to the top plate. Again, we suspect that contact-line pinning plays a very important role in the experiments of Gupta *et al.* [4]. In some cases, this prevents the contact line from spreading on the silicone, and leads to very little liquid transfer. In other cases, even though the initial radius is smaller on the silicone (due to pinning by surface defects), motion of the contact line caused by bridge stretching is able to overcome the pinning and almost all the liquid transfers to the silicone.

Finally, we recall that the model predictions of liquid transfer at low Ca and large contact-angle differences agreed well with the experimental observations of Chen *et al.* [5] (section 3.1). Given that similar conditions exist in the experiments of Gupta *et al.* [4], we might have expected similar agreement. The discrepancies suggest that contact-line pinning is much less important in the experiments of Chen *et al.* [5] at low Ca when the contact-angle difference is sufficiently large. Thus, the results of Gupta *et al.* [4] indicate that even if the contact-angle difference is large ($\sim 20^\circ$), liquid transfer in the quasi-static regime can be very strongly inflected by contact-line pinning.

2.6 Conclusions

The results of our calculations indicate that it is not always necessary to account for contact-angle hysteresis (CAH) to accurately predict liquid transfer. In particular, for very low capillary numbers (Ca), both the slender-jet and two-dimensional (2D) axisymmetric model yield predictions in good agreement with experimental observations provided that the the difference in receding contact angles ($|\Delta\theta_r|$) between the plates is sufficiently large (section 3.1). In this regime, liquid transfer is primarily governed by wettability differences. Contact-line motion during the earlier stages of stretching largely sets the overall bridge shape and thus the transfer ratio. As a consequence, the models predict the transfer ratio well even if contact-line motion is not predicted accurately toward the end of bridge stretching.

However, if $|\Delta\theta_r|$ is small enough (section 3.1) or the surface heterogeneities are prominent enough (section 5), then wettability differences may not be strong enough

to overcome the influence of surface heterogeneities, and accounting for CAH becomes important even at low Ca. In this regime, predictions of the transfer ratio will also be very sensitive to errors in the measured contact angles.

For $O(1)$ values of Ca, the models predict that each plate ends up with the same amount of liquid, in agreement with experimental observations (section 3.2). In this regime, viscous forces overwhelm the influence of wettability differences. For intermediate values of Ca (section 3.2), predictions of the transfer ratio from each model can deviate substantially from the experimental data. In this regime, neither wettability differences nor viscous forces are dominant, so surface heterogeneities (which are not included in the models) may strongly influence liquid transfer. Since the 1D model neglects radial pressure variations (and thus the associated viscous dissipation), it predicts greater contact-line movement relative to the 2D model. As a consequence, the 2D model generally yields more accurate values of the transfer ratio.

Nevertheless, our results also indicate that the simpler 1D model can provide qualitatively accurate descriptions of the transfer ratio as a function of $|\Delta\theta_r|$ and Ca. In some cases, it even provides quantitatively accurate estimates. Thus, the 1D model may be a useful tool for exploratory studies that incorporate other physical effects (e.g., electrostatics). For both the 1D and 2D models, our results suggest that it may be necessary to account for the speed-dependence of the contact angle to accurately describe contact-line motion near bridge breakup, where the contact-line speed increases rapidly (section 4).

As noted in section 1, stretching liquid bridges with moving contact lines play a central role in the operation of roll-to-roll printing processes. These processes may operate under conditions (e.g., intermediate values of Ca) where models of bridge behavior neglecting CAH do not yield quantitatively accurate predictions of liquid transfer. Nevertheless, the results of the present work demonstrate that such models can yield qualitatively accurate predictions. We expect that these predictions will ultimately aid the optimization of gravure and other printing processes for manufacturing of printed electronic devices.

Chapter 3

Electrostatic Assist of Liquid Transfer between Flat Surfaces

3.1 Introduction

Although printing processes have been used for centuries to make books and newspapers, they are increasingly being developed for large-scale manufacturing of electronic devices including transistors [14, 50, 76, 77], solar cells [52], and antennas [78]. In these printing processes, the inks are conductive materials that are deposited onto flexible substrates such as paper [79] or thin plastic films [80]. A flexible substrate is unwound from a cylindrical roll and then wound onto another roll after printing. Such roll-to-roll printing techniques have potential to significantly reduce production costs, speed up manufacturing processes [46], and reduce waste disposal [81].[1]

One important printing process is gravure printing (Fig. 3.1(a)). The gravure roll is a metal cylinder that has been engraved with a large number of micron-scale cavities. The cavities are filled with ink from a liquid pool, and the ink then transfers from the cavities to a substrate. A backing roll is used to force contact between the substrate and gravure roll.

For printed electronics, it is essential that enough ink be transferred from the cavities to the substrate to prevent broken circuits and failure of electronic devices. However,

[1] This chapter has been published in [82]

it has been found that only 50% of the ink transfers to the substrate at high printing speeds. An electrostatic potential difference between the substrate and gravure roll is sometimes applied to improve ink transfer in traditional printing processes [3, 27, 83, 84], a method is known as electrostatic assist (ESA) (Fig. 3.1(a)). However, the physical mechanisms underlying ESA remain a mystery. If these mechanisms were better understood, then ESA could be effectively applied to the printing of electronic devices, thereby reducing the number of defects. This paper describes research addressing this issue.

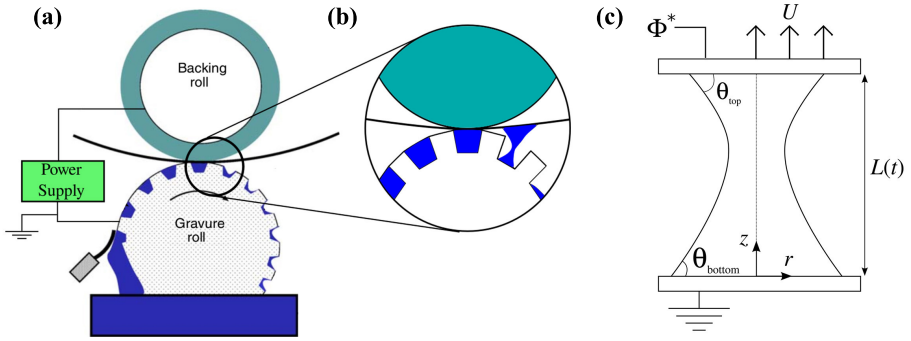

Figure 3.1: (a) Schematic of a gravure printing process with electrostatic assist. The ink in a cavity is transferred from an engraved roll to a substrate. (b) Illustration of a stretching liquid bridge. (c) Schematic of a stretching liquid bridge subject to an electric field.

The key to printing processes involves the formation of a liquid bridge, which is a mass of liquid connecting two solid surfaces, and transfer of liquid from one surface to another (Fig. 3.1(b)). This paper focuses on an important model problem concerning liquid transfer, shown in Fig. 3.1(c). A mass of liquid is initially deposited on the bottom surface. A second flat surface is lowered so that it comes into contact with that liquid to form a liquid bridge. An electrostatic potential difference is applied between the two flat surfaces, and the top surface is then pulled vertically until the liquid bridge breaks. During this process, the contact lines (where air, liquid, and solid meet) move on the two flat surfaces. The central issue is to determine the amount of liquid transferred from the bottom surface (printing plate) to the top surface (substrate) as the two surfaces separate. Although gravure printing involves liquid transfer from cavities (Fig. 3.1(b)), the model problem considered here (Fig. 3.1(c)) provides a necessary foundation for

understanding the more complex problem involving cavities. This model problem is also highly relevant to other applications including adhesion [47], oil recovery [48], and microfluidics [49].

There have been a number of prior studies investigating liquid transfer between two flat surfaces subject to extensional motion in the absence of an electric field [5, 6, 46, 54, 57, 61]. A key parameter characterizing the problem is the capillary number, $Ca = \mu U/\gamma$, which represents the ratio of viscous forces to surface-tension forces, where μ is the liquid viscosity, U is the stretching speed, and γ is the liquid-air surface tension. Experimental results and model predictions show that when Ca is smaller than $\sim 10^{-2}$, liquid transfer is determined by the wettability difference between the two surfaces. When Ca is ~ 1, viscous forces become stronger and reduce the influence of wettability differences. As a consequence, the amount of liquid transferred is close to 50%. It is thus a major challenge to transfer more than 50% of the liquid at high printing speeds. Other forces, such as those arising from applied electric fields (Fig. 3.1(a)), could be an effective way to enhance liquid transfer at high capillary numbers.

Because the liquid bridge becomes long and thin during stretching, slender-jet models have been applied to describe bridge dynamics [7, 54, 63, 69]. These models are based on the assumption that the variation of the interface shape is small relative to the bridge length, so to leading order the bridge shape and axial velocity depend only on the axial coordinate and time [69]. Predictions from slender-jet models of the amount of liquid transferred agree qualitatively and sometimes quantitatively with experimental observations [7, 54]. Slender-jet models thus provide an efficient way to describe the shape of stretching liquid bridges with moving contact lines. Electrostatic effects have been incorporated into slender-jet models to describe electrospinning [34, 43, 85], and the goal of the present paper is to make a similar effort to describe liquid transfer.

The paper is organized as follows. The mathematical model, which consists of an axisymmetric Newtonian liquid bridge between two surfaces of different wettability that are subject to an electric field and can separate vertically (Fig. 3.1(c)), is developed in Sec. 2. Results for perfect dielectric (non-conducting) liquids and leaky dielectric (weakly conducting) liquids are presented in Secs. 3 and 4, respectively. Complementary flow visualization experiments have also been performed, and these are reported and compared to the model predictions in Sec. 5. In Sec. 6, we summarize our results and

provide some concluding remarks.

3.2 Problem formulation

An axisymmetric Newtonian liquid bridge with constant density ρ, viscosity μ, and surface tension γ is confined between two flat electrodes (Fig. 3.1(c)). Air is outside the bridge and assumed to have no influence on the liquid flow. The top electrode has a constant electrostatic potential ϕ^* and is moved in the z-direction (vertically) with a constant velocity U, while the bottom electrode is grounded and remains stationary. Note that because the potentials are constant, the magnitude of the electric field decreases during bridge stretching. The contact angle for the top electrode is denoted as θ_{top}, and that for the lower electrode is θ_{bottom}. Even though these contact angles may depend on the speed of contact line, we consider here the limiting case where they are constant.

In this study, we consider two types of liquids. The first is a perfect dielectric, for which the conductivity and charge are zero but polarization can occur. The other is a leaky dielectric [32, 33, 35], which is polarizable but weakly conductive. Charges inside the liquid accumulate at the liquid-air interface and are assumed to be negligible in the bulk. Air is modeled as a perfect dielectric fluid with relative permittivity $\epsilon = 1$. The relative permittivity of the liquid is $\epsilon = \epsilon^*$, its conductivity is K, and the free-space permittivity is ϵ_o.

3.2.1 Governing equations

We scale length by a characteristic initial bridge radius R, velocity by U, time by R/U, pressure by $\mu U/R$, electrostatic potential by ϕ^*, electric field by $E^* = \phi^*/L(0)$ (where $L(0)$ is the initial bridge length), charge density by $\epsilon_o E^*$, and conductivity by $K^* = RK/U\epsilon_o$. The mass conservation equation is

$$\nabla \cdot \mathbf{v} = 0. \tag{3.1}$$

Electric charge conservation at the liquid-air interface requires that

$$\frac{\partial \sigma}{\partial t} + \mathbf{v} \cdot \nabla_s \sigma = \sigma \mathbf{n} \cdot (\mathbf{n} \cdot \nabla)\mathbf{v} + \parallel -K^* \mathbf{E} \parallel \cdot \mathbf{n}, \tag{3.2}$$

where σ is the surface charge density, t is time, $\nabla_s = (\mathbf{I} - \mathbf{nn}) \cdot \nabla$ is the surface gradient operator, $\mathbf{E}$ is the electric field, $\| \ ... \ \|$ is the jump operator which yields the quantities in the air phase minus those in liquid phase, and $\mathbf{n}$ is the outward unit normal to the interface. The electric field is related to the electrostatic potential through

$$\mathbf{E} = -\nabla\phi. \tag{3.3}$$

The momentum conservation equation is

$$Re(\frac{\partial \mathbf{v}}{\partial t} + \mathbf{v} \cdot \nabla\mathbf{v}) = -\nabla P + \chi \nabla \cdot \boldsymbol{\sigma}^M + \nabla^2\mathbf{v}, \tag{3.4}$$

where $\mathbf{v}$ is the velocity vector and P is the pressure. The two parameters that appear are the electroviscous number $\chi = RE^{*2}\epsilon_o/\mu U$, which provides a ratio of electrostatic to viscous forces, and the Reynolds number $Re = \rho U R/\mu$, which provides a ratio of inertial to viscous forces.

In Eq. (3.4), $\boldsymbol{\sigma}^M$ is the Maxwell stress tensor which is given by $\epsilon\epsilon_o\mathbf{EE} - \frac{1}{2}\epsilon\epsilon_o\mathbf{E} \cdot \mathbf{EI}$, where $\mathbf{I}$ is the identity tensor. The divergence of the Maxwell stress tensor is zero for perfect and leaky dielectrics [33]. Hydrodynamic and electrostatic phenomena are coupled through the normal and tangential stress balances at the liquid-air interface [45]. The dynamics of the air phase are assumed negligible.

At the liquid-air interface, we have the kinematic boundary condition,

$$\mathbf{n} \cdot \mathbf{v} = 0. \tag{3.5}$$

The normal stress balance is

$$\| \ \mathbf{n} \cdot \mathbf{T} \cdot \mathbf{n} \ \| = -\frac{\kappa}{Ca}, \tag{3.6}$$

where $\mathbf{T} = -P\mathbf{I} + \mu[\nabla\mathbf{v} + (\nabla\mathbf{v})^T] + \boldsymbol{\sigma}^M$ is total stress tensor, $\kappa = \nabla_s \cdot \mathbf{n}$ is the interfacial curvature, and $Ca = \mu U/\gamma$ is the capillary number, which provides a ratio of viscous to surface-tension forces. The tangential stress balance is

$$\| \ \mathbf{n} \cdot \mathbf{T} \cdot \mathbf{t} \ \| = 0, \tag{3.7}$$

where $\mathbf{t}$ is the unit tangent vector to the liquid-air interface. Gravitational forces are assumed to be negligible relative to surface-tension forces, which corresponds to a small Bond number, $Bo = \rho g R^2/\gamma$.

At each solid surface, the no-slip and no-penetration conditions are

$$\mathbf{t}_{wall} \cdot \mathbf{v} = 0 \quad \text{at } z = 0, L(t), \tag{3.8}$$

$$\mathbf{n}_{wall} \cdot \mathbf{v} = \begin{cases} 0 & \text{for } z = 0 \\ 1 & \text{for } z = L(t), \end{cases} \tag{3.9}$$

where $\mathbf{n}_{wall}$ is the normal vector pointing in the positive axial direction, $\mathbf{t}_{wall}$ is the tangential vector pointing in the radial direction, and $L(t)$ represents the location of the top electrode. We note that near moving contact lines, the no-slip boundary condition breaks down and is usually replaced by a slip law, a point we address in Sec. 3.2.3.

The electrostatic potential ϕ in each phase is governed by Laplace's equation,

$$\nabla^2 \phi = 0. \tag{3.10}$$

The boundary conditions for the top and bottom electrode are

$$\phi = \begin{cases} 0 & \text{for } z = 0 \\ 1 & \text{for } z = L(t). \end{cases} \tag{3.11}$$

The tangential components of the electric field are continuous at the interface, and a jump in the normal component of the electric field is related to the surface charge density σ [33],

$$\parallel \epsilon \mathbf{E} \parallel \cdot \mathbf{n} = \sigma. \tag{3.12}$$

3.2.2 1D slender-jet model

The liquid bridge radius is assumed to be much smaller compared to its length, so a small parameter $\epsilon_s \equiv R/L(0)$ can be defined. We then perform an asymptotic expansion on the axial velocity v, axial electric field E, and pressure P [54, 63, 69]:

$$v(r, z, t) = v_o(z, t) + (\epsilon_s r) v_1(z, t) + (\epsilon_s r)^2 v_2(z, t) + \cdots, \tag{3.13}$$

$$E(r, z, t) = E_o(z, t) + (\epsilon_s r) E_1(z, t) + (\epsilon_s r)^2 E_2(z, t) + \cdots, \tag{3.14}$$

$$P(r, z, t) = P_o(z, t) + (\epsilon_s r) P_1(z, t) + (\epsilon_s r)^2 P_2(z, t) + \cdots. \tag{3.15}$$

Because the dependence on the radial coordinate r is given explicitly in the expansion, the correction functions of these three variables only depend on time and the axial coordinate.

Equations (3.13)-(3.15) are substituted into Eqs. (3.1)-(3.12) to reduce them to a one-dimensional (1D) problem [67]. After keeping the leading order terms and dropping the subscripts "o" for simplicity, the governing equations become

$$Re(v_t + vv_z) = -\frac{1}{Ca}\kappa_z + \frac{3}{h^2}(h^2 v_z)_z + \chi(\beta E E_z + \sigma\sigma_z + \frac{2\sigma E}{h}), \tag{3.16}$$

$$h_t = -vh_z - \frac{1}{2}v_z h, \tag{3.17}$$

$$E - E_\infty + \ln(\Lambda)((\sigma h)_z - \frac{\beta}{2}(Eh^2)_{zz}) = 0. \tag{3.18}$$

$$\sigma_t + v\sigma_z + \frac{\sigma}{2}v_z - K^*(h_z E + \frac{h}{2}E_z) = 0, \tag{3.19}$$

where h is the position of the liquid-air interface (i.e., bridge radius), E_∞ is the electric field in the absence of the liquid, $\Lambda = L(0)/2R$ is the initial bridge aspect ratio, $\beta = \epsilon^* - 1$ is the permittivity constant, and κ is the interfacial curvature,

$$\kappa = \frac{1}{h(1+h_z^2)^{\frac{1}{2}}} - \frac{h_{zz}}{(1+h_z^2)^{\frac{3}{2}}}. \tag{3.20}$$

The indices t and z indicate differentiation with respect to those variables. The full curvature is kept to gain a more accurate description of the interface [31, 63, 67, 68, 69, 70]. The electric field inside the bridge is determined by the induced charges or free charges at the interface. Equation (3.18), which has been previously used by Feng [43] and Hohman *et al.* [34] to describe electrospinning, is derived from an integral solution (in cylindrical coordinates) to Laplace's equation [86].

3.2.3 Solution method

Equations (3.16)-(3.19) are solved with a finite-element method [54, 63, 69]. To lower the highest-order derivative in these equations, two new variables, Ω and ω, are introduced,

$$\Omega - \frac{\partial h}{\partial z} = 0, \tag{3.21}$$

$$\omega - \frac{\partial (h^2 E)}{\partial z} = 0. \tag{3.22}$$

The no-penetration boundary condition is

$$v(z=0,t)=0, v(z=L(t),t)=1. \tag{3.23}$$

The boundary conditions on electrostatic potential are

$$\phi(z=0,t)=0, \phi(z=L(t),t)=1. \tag{3.24}$$

No-flux boundary conditions are applied on σ,

$$\frac{\partial\sigma}{\partial z}(z=0)=0, \frac{\partial\sigma}{\partial z}(z=L(t))=0. \tag{3.25}$$

The contact angle appears through a geometric relation

$$\Omega=\frac{\partial h}{\partial z}=\cot(\theta), \tag{3.26}$$

where θ is θ_{top} or θ_{bottom}. It turns out that the slip law (3.2.1) does not appear at leading order and so cannot be imposed [63]. However, the contact line is still free to move when Eq. (3.26) is applied [63]. As a consequence no boundary condition needs to be applied on h.

When the liquid bridge is about to pinch off, the droplet on each surface is connected by a thin liquid thread. We stop the simulations when the narrowest bridge radius is 1% of its initial radius. At this point, the overall bridge shape has largely been set, and thus the transfer ratio, which is the percentage of liquid transferred to the top surface (plate), does not change significantly even if the bridge thins further.

To ensure mass conservation, we monitor the variation of volume, $V_{var}=100(V_{max}-V_{min})/V_{ini}$, where V_{max}, V_{min}, and V_{ini} are the maximum, minimum and initial bridge volume, respectively. If V_{var} is larger than 0.1%, we increase the number of elements or decrease the time step, then rerun the simulation and repeat this process until V_{var} is less than 0.1% [57].

3.2.4 Parameter values

Order-of-magnitude values of the dimensional parameters are listed in Table 3.1, and the corresponding dimensionless parameters are shown in Table 3.2. In this work we choose to focus on regime of small Bond numbers (Bo) and thus neglect gravitational effects,

as we have done in Eqs. (3.4) and (3.16). Similarly, we choose to focus on the regime of small Reynolds numbers (Re), and thus neglect inertial forces by setting $Re = 0$. We thus investigate the influence of the capillary number, Ca, and electroviscous number, χ. The dimensionless conductivity, K^*, is the ratio of the time scale for bridge stretching to the charge relaxation time and appears when considering leaky dielectrics. In our calculations, the initial bridge aspect ratio (ratio of initial length to initial diameter) is around unity. As the bridge stretches, the aspect ratio increases and the slender-jet model is expected to provide an increasingly accurate approximation.

Table 3.1: Order-of-magnitude values of dimensional parameters

Parameter	Typical Values
Bridge radius R and bridge length L (mm)	$10^{-3} - 1$
Liquid viscosity μ (cP)	$1 - 10^2$
Surface tension γ (mN/m)	$10^1 - 10^2$
Stretching speed U (mm/s)	$1 - 10^2$
Voltage V (volt)	$10^2 - 10^4$
Conductivity K (S/m)	$10^{-12} - 10^{-2}$

Table 3.2: Dimensionless problem parameters

Parameter	Definition	Physical meaning	Value
Bo	$\rho g R^2/\gamma$	$\frac{\text{Gravitational forces}}{\text{Surface-tension forces}}$	$10^{-7} - 1$
Re	$\rho U R/\mu$	$\frac{\text{Inertial forces}}{\text{Viscous forces}}$	$10^{-5} - 10^2$
Ca	$\mu U/\gamma$	$\frac{\text{Viscous forces}}{\text{Surface-tension forces}}$	$10^{-5} - 1$
χ	$RE_o^2\epsilon_o/\mu U$	$\frac{\text{Electrostatic forces}}{\text{Viscous forces}}$	$10^{-2} - 10^8$
ϵ		Relative permittivity	$1 - 10^1$
β	$\epsilon^* - 1$	Polarizability difference between liquid and air phases	$1 - 10^1$
K^*	$(R/U)/(\epsilon_o/K)$	$\frac{\text{Time scale for stretching}}{\text{Time scale for charge relaxation}}$	$10^{-6} - 10^9$
Λ	$L(0)/2R$	$\frac{\text{Initial bridge length}}{\text{Initial bridge diameter}}$	1

3.3 Results: Perfect dielectrics

3.3.1 Liquid transfer

In the absence of an electric field, the transfer ratio (percentage of liquid transferred to the top plate) is determined by the wettability difference between the two plates when Ca is low (< 0.01) [54, 57]. As Ca increases, viscous forces become stronger relative to

surface-tension forces, and as a result, the transfer ratio approaches 50% regardless of the wettability difference. Here, we explore how an electric field influences this behavior for perfect dielectric liquids. This corresponds to setting $\sigma = 0$ and $K = 0$, and solving Eqs. (3.16)-(3.18).

In this section, the initial shape is taken to be a cylinder with length $L(0)$ and radius R. This choice allows us to isolate the influence of the electric field; the influence of initial bridge shape is explored in Sec. 3.3. The initial cylinder aspect ratio ($\Lambda = L(0)/2R$) is 1. The capillary number Ca is set to 0.1 or 1, and the electroviscous number χ ranges from 0 (no electric field applied) to 100. The permittivity constant $\beta = 1.74$, which corresponds to the permittivity of silicone oil. We choose this value because silicone oil has been used in experiments examining the stability of liquid bridges in electric fields [38, 39, 87, 88]. For computational convenience, we rotate the liquid bridge 90° clockwise, so the top/bottom plate is on the right/left side in the figures showing bridge shapes.

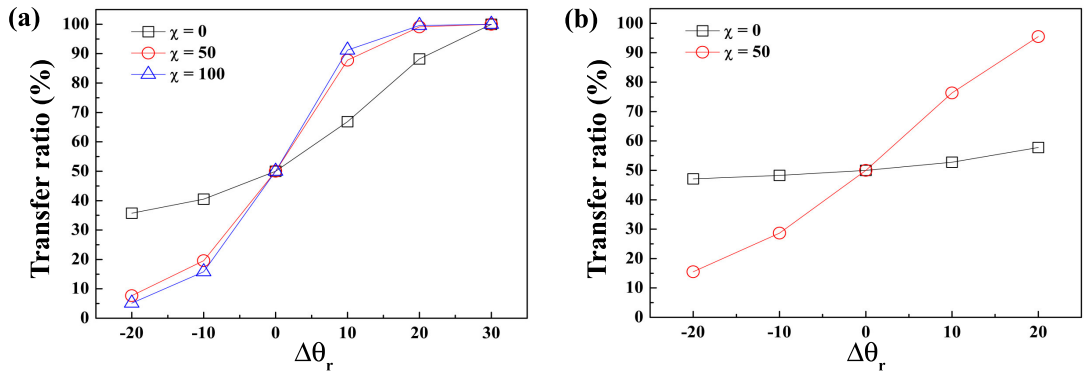

Figure 3.2: Relationship between transfer ratio and wettability difference for different values of χ for (a) $Ca = 0.1$ and (b) $Ca = 1$. Here, θ_{top} is 60° and θ_{bottom} varies from 40° to 80°. The wettability difference is $\Delta\theta_r = \theta_{\text{bottom}} - \theta_{\text{top}}$, and the parameter $\beta = 1.74$.

Figure 3.2 shows the transfer ratio for the cases where the top contact angle $\theta_{\text{top}} = 60°$ and the bottom contact angle θ_{bottom} ranges from 40° to 90°. These angles are assumed to be receding contact angles [54]. The wettability difference $\Delta\theta_r = \theta_{\text{bottom}} - \theta_{\text{top}}$, so a positive $\Delta\theta_r$ means the top plate is more wettable than the bottom plate.

When $Ca = 0.1$, the transfer ratio increases as $\Delta\theta_r$ increases when $\chi = 0$ (Fig. 3.2(a)). Because the bottom plate becomes less wettable when $\Delta\theta_r$ increases, more

liquid is transferred to the top plate. When Ca is $O(1)$ and no electric field is present (Fig. 3.2(b)), viscous forces are stronger and reduce the effect of surface wettability differences, so the transfer ratios are nearly 50% for all values of $\Delta\theta_r$. We note that for values of $Ca < 0.1$, the influence of the electric field is considerably weaker since χCa, the ratio of electrostatic forces to surface tension forces, becomes smaller.

Both Figs. 3.2(a) and 3.2(b) show that when χ increases from 0 to 50, the transfer ratio of the electrified bridge is higher than that for the non-electrified bridge when $\Delta\theta_r$ is positive. However, when $\Delta\theta_r$ is negative, the presence of an electric field decreases the amount of liquid transferred. These results show that the electrostatic forces enhance liquid transfer to the more wettable surface even when viscous forces are strong ($Ca = O(1)$). In Fig. 3.2(a), when χ is doubled from 50 to 100, the transfer ratio only slightly increases or decreases. Therefore, we will focus on the cases $\chi = 0$ and 50.

As mentioned in the introduction, the transfer ratio is only about 50% at high printing speeds, and this represents a major challenge to print quality. Figure 3.2(b) shows that application of an electric field can significantly increase the transfer ratio when $\Delta\theta_r$ is positive and Ca is $O(1)$. This finding is consistent with the use of ESA (Sec. 1) to improve liquid transfer in industrial printing processes.

We now characterize how the electric field changes the bridge shape and contact-line movement. Figures 3.3(a) and 3.3(b) shows the final bridge shapes when $\chi = 0$ (no electric field) and 50 for $Ca = 0.1$ and 1. The wettability difference $\Delta\theta_r$ is 10°. In both Figs. 3.3(a) and 3.3(b), the contact line positions on the top (right) plate for both $\chi =$ 0 and 50 are almost the same. However, the contact line of the electrified liquid bridge on the bottom (left) plate (which is less wettable than the top plate) has slipped more relative to that of the non-electrified liquid bridge. This result shows that the presence of the electric field increases the transfer ratio by pushing more liquid away from the less wettable surface. The mechanism for this will be discussed in Sec. 3.2.

Figures 3.3(c) and 3.3(d) show the time-evolution of the contact-line positions. In Fig. 3.3(c) ($Ca = 0.1$), both the top and bottom contact radii (i.e., radii at top/bottom plates) of the electrified bridge are always smaller than those of the non-electrified bridge, but the top contact radius of the electrified bridge eventually reaches a similar value to that of the non-electrified bridge. However, the bottom contact line of the electrified bridge retreats much faster than that of the non-electrified bridge. Therefore,

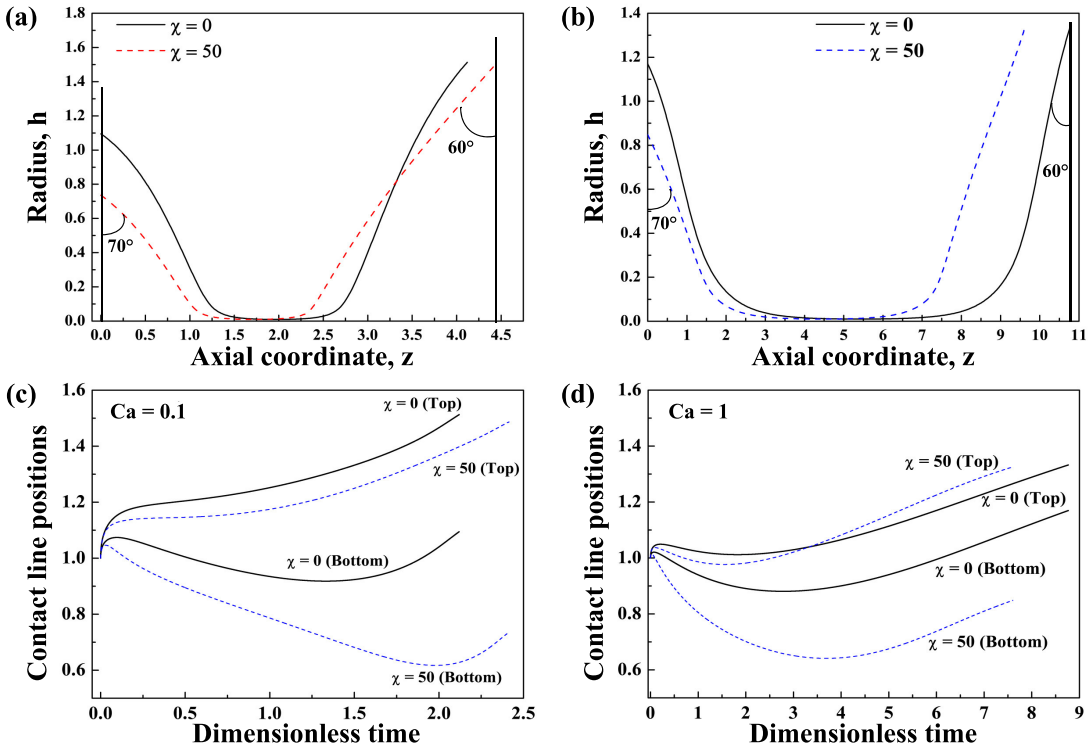

Figure 3.3: Comparison of final bridge shapes and contact-line positions for the cases $\chi = 0$ (solid lines) and 50 (dashed lines). (a,c) $Ca = 0.1$; the breakup times for $\chi = 0$ and 50 are 2.1 and 2.4, respectively. (b,d) $Ca = 1$; the breakup times for $\chi = 0$ and 50 are 8.8 and 7.6, respectively. Values of other parameters are $\theta_{\text{bottom}} = 70°$, $\theta_{\text{top}} = 60°$, $\Delta\theta_r = 10°$, and $\beta = 1.74$.

less liquid remains on the bottom plate (Fig. 3.3(a)) and the transfer ratio increases when the electric field is present. Similar behavior is seen in Fig. 3.3(d) ($Ca = 1$), although here the top contact radius of the electrified bridge can become larger than that of the non-electrified bridge. The contact radii increase with time at later times because of the high pressure that develops near the bridge center. The resulting pressure gradients drive liquid toward the contact lines, causing the contact radii to increase.

In practice, the contact lines could pin during bridge stretching due to surface heterogeneities. We briefly discuss the influence of the electric field when one contact line is pinned. When both contact lines are pinned, the electric field does not affect the transfer ratio due to symmetry.

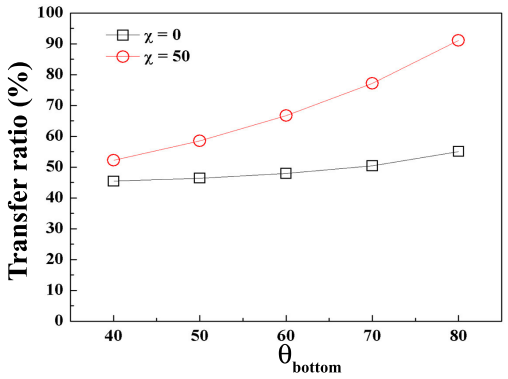

Figure 3.4: Relationship between transfer ratio and the value of bottom contact angle for different values of χ. The top contact line is pinned and θ_{bottom} is varied. Values of other parameters are $Ca = 1$ and $\beta = 1.74$.

Figure 3.4 shows transfer ratio with different bottom contact angles when the top contact line is pinned and $Ca = 1$. We only discuss the case where $Ca = 1$ because the effect of the electric field on liquid transfer at lower Ca is qualitatively similar. When $\chi = 0$, the transfer ratio is around 50%. This can be understood by recognizing that when viscous forces are strong enough, the contact line does not slip much along the plate. The pinch-off point is near the center of the bridge, and the bottom contact line is close to its original position.

When $\chi = 50$, the transfer ratio increases as the bottom contact angle increases. The reason is similar to the cases where both contact lines can move. The top plate can be rationalized as a surface with such a small receding contact angle that the contact

angle on the top plate does not reach the receding value and the contact line is pinned during stretching. The bottom contact line of the electrified bridge retreats much more than that of the non-electrified bridge. As a result, the transfer ratio increases when the electric field is present. However, if we pin the bottom contact line and allow the top contact line to slip, the results (not shown) are the mirror images of the case where the top contact line is pinned. Therefore, the transfer ratios are less compared to the case where there is no electric field and the bottom contact line is pinned.

Figures 3.3(c), 3.3(d), and 3.4 illustrate that the presence of an electric field has a significant influence on contact-line motion, especially on the less wettable surface. As a consequence, the transfer ratio is significantly affected. We now discuss the physical mechanism underlying these phenomena by analyzing the pressure in the liquid bridge.

3.3.2 Physical mechanisms

For perfect dielectric liquids, the only way the Maxwell stress tensor affects the liquid bridge is through the normal stress balance (Eq. (3.6)). The resulting expression for the liquid pressure in the slender-jet approximation is

$$P = \frac{\kappa}{Ca} - v_z - \chi\frac{\beta}{2}E^2. \tag{3.27}$$

Note that in the slender-jet approximation, the pressure depends spatially only on the axial coordinate. The three terms on the right-hand side of Eq. (3.27) represent contributions from surface-tension, viscous, and electrostatic forces, respectively. The electrostatic term arises from the polarizability difference (β) between the liquid and air phase, and always acts to decrease the value of the pressure. Note that increasing the value of β will tend to enhance electrostatic effects.

In determining physical mechanisms, it is useful to define a relative pressure, which is the difference between the pressure and the minimum pressure in the liquid bridge. We set $Ca = 1$ because of its relevance to high-speed printing, and first consider the case $\Delta\theta_r = 0^\circ$ to remove the influence of wettability differences.

Figure 3.5(a) compares bridge shapes when $\chi = 0$ and 50 at $t = 1$, and the corresponding relative pressure profiles are shown in Fig. 3.5(b). In Fig. 3.5(a), the contact radii of the electrified bridge are smaller than those of the non-electrified bridge. In

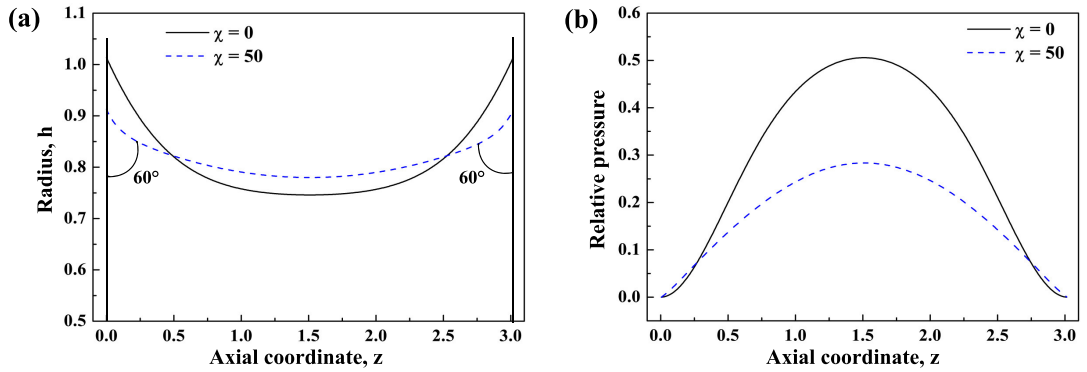

Figure 3.5: (a) Comparison of bridge shapes for the cases $\chi = 0$ (solid line) and 50 (dashed line) at $t = 1$. (b) Comparison of relative pressure for the cases $\chi = 0$ (solid line) and 50 (dashed line) at $t = 1$. Values of other parameters are $Ca = 1$, $\theta_{\text{bottom}} = 60°$, $\theta_{\text{top}} = 60°$, $\Delta\theta_r = 0°$, and $\beta = 1.74$.

addition, the narrowest radius of the electrified bridge is greater than that of the non-electrified bridge. These features can be explained by examining the pressure in the bridge (Fig. 3.5(b)). The pressure of both bridges is highest at the center and lowest at each contact line due to the axial variation of the radius. However, the highest pressure of the electrified bridge is smaller than that of the non-electrified bridge due to the presence of the electric field.

In Eq. (3.27), the electrostatic term is always negative since χ and β are always positive. Note that the E in Eq. (3.27) represents the electric field tangent to the interface. The normal component of the electric field is negligible due to the slender-jet assumption. Therefore, the magnitude of the electrostatic term is greater near the center than near each contact line. As a consequence, the maximum pressure difference of the electrified bridge is smaller than that of the non-electrified bridge.

As the bridge extends, the contact radii decrease to conserve mass. However, since the bridge radius is narrowest at the center, liquid is pumped from the center toward the contact lines. When the electric field is applied, the smaller maximum pressure difference results in less liquid being driven away from the bridge center, leading to a larger value of the narrowest radius and smaller values of the contact radii.

We now consider the case where $\Delta\theta_r = 10°$ to examine how the electric field enhances liquid transfer to the more wettable surface. Figure 3.6(a) shows bridge shapes and the

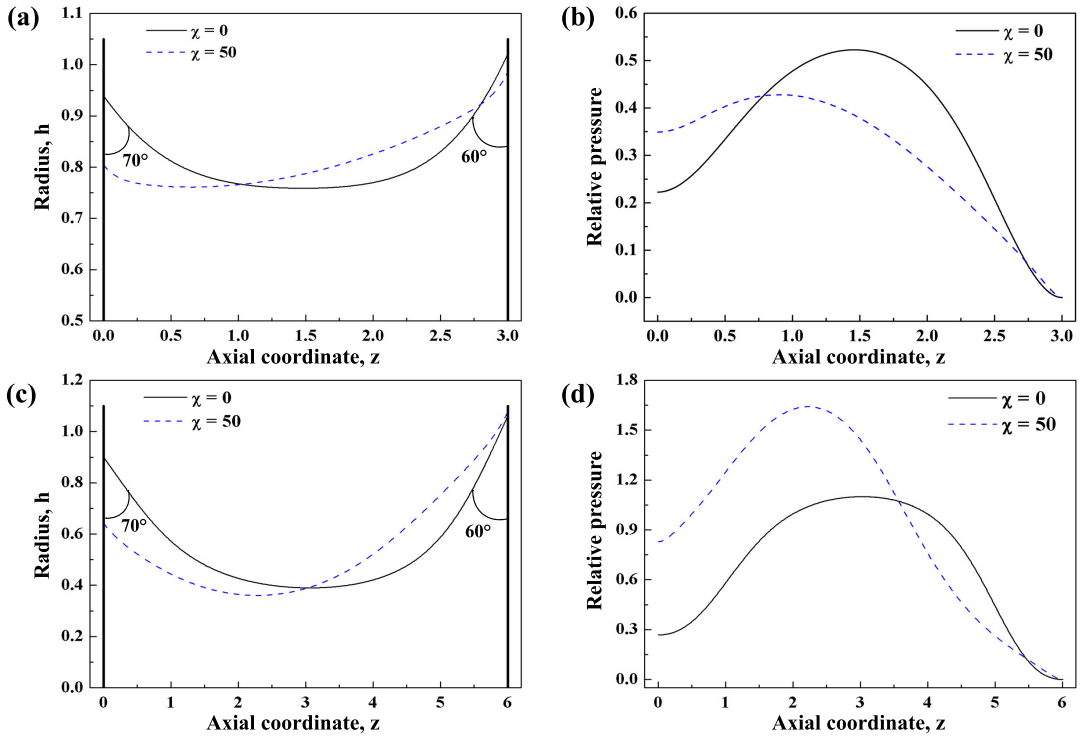

Figure 3.6: Comparison of bridge shapes (a,c) for the cases $\chi = 0$ (solid line) and 50 (dashed line) with corresponding relative pressures (b,d) at (a,b) $t = 1$ (c,d) $t = 4$. Values of other parameters are $Ca = 1$, $\theta_{\text{bottom}} = 70°$, $\theta_{\text{top}} = 60°$, $\Delta\theta_r = 10°$, and $\beta = 1.74$.

corresponding relative pressure profiles at $t = 1$. In Fig. 3.6(a), the bottom contact radius of the electrified bridge is smaller than that of the non-electrified bridge. In addition, the narrowest radius of the electrified bridge is located closer to the bottom (left) plate, which means that the bridge would break closer to the bottom plate when an electric field is applied.

As can be seen in Fig. 3.6(b), when the electric field is present, the difference between the maximum pressure and the pressure at the top (right) plate is larger than the difference between the maximum pressure and the pressure at the bottom (left) plate. Since the bottom contact angle is greater than the top contact angle, the magnitude of the tangential component of the electric field at the bottom is greater than that at the top. Therefore, the electric field has a greater influence on the pressure near the bottom plate, and the difference between the maximum pressure and the pressure at the bottom plate decreases significantly when an electric field is applied. As a consequence, liquid is driven from the region of maximum pressure (near the bottom plate) to the top plate, causing the bottom contact radius to decrease even more.

The decrease in the bottom contact radius at later times ($t = 4$) is seen in Fig. 3.6(c). Because the bottom contact radius of the electrified bridge is considerably smaller than that of the non-electrified bridge, the electrified bridge has a smaller minimum bridge radius. As a result, the maximum relative pressure in the electrified bridge becomes larger than that in the non-electrified bridge, and so does the difference in relative pressures between the maximum and the top (right) plate, as seen in Fig. 3.6(d). The subsequent flow causes the electrified bridge to break earlier than the non-electrified bridge when $Ca = 1$ (Fig. 3.3(b)), and leads to more liquid being transferred to the more wettable surface. Note that since the magnitude of the electric field decreases during stretching (due to a constant voltage difference between the top and bottom plates), the electrostatic contribution to the pressure is not able to stabilize the bridge as breakup is approached.

When $Ca = 0.1$, the mechanism for the increase in liquid transfer to the more wettable surface in the presence of the electric field is the same as in the case where $Ca = 1$ (results not shown). Because viscous forces are weaker relative to surface-tension forces (which drive liquid away from the narrowest part of the bridge) when $Ca = 0.1$, the bridge cannot be stretched as far before breakup compared to the case

where $Ca = 1$ (Fig. 3.3). However, the shorter breakup length means that electrostatic forces are more effective at stabilizing the bridge. As a result, the electrified bridge can be stretched longer than the non-electrified liquid bridge when $Ca = 0.1$ (or lower) (Fig. 3.3(a)).

When the two surfaces have the same wettability ($\Delta\theta_r = 0°$), we also observe that an electrified bridge cannot be stretched as far before breakup compared to a non-electrified bridge when $Ca = 1$ (results not shown). At early times, the maximum pressure in the electrified bridge (which occurs at the point of narrowest radius) is lower compared to that in the non-electrified bridge due to the stabilizing effect of the electric field. However, at later times, the maximum pressure in the electrified bridge becomes larger than that in the non-electrified bridge due to the weakening of electrostatic forces as the bridge length increases. The larger maximum pressure leads to larger pressure gradients that rapidly drive liquid away from the narrowest part of the bridge, leading to a shorter breakup time for the electrified bridge.

3.3.3 Influence of initial bridge shape

In general, the initial liquid bridge shape in experiments will not be a perfect cylinder [5, 4]. For example, if an equilibrium shape is used, the contact line positions on each surface will be different due to differences in surface wettability. In this section, we report results from a brief parametric study examining the influence of using equilibrium bridge shapes as initial conditions.

To obtain an equilibrium bridge shape, we start with a cylinder having a length equal to its diameter ($\Lambda = 1$), set the velocity of both plates to zero, and solve the governing equations numerically until an equilibrium state is reached. Because the velocity of the top plate is zero, a new velocity scale is needed. We choose this to be γ/μ, and the corresponding time scale is $R\mu/\gamma$. Therefore, a new dimensionless parameter representing the ratio of electrostatic forces to surface-tension forces arises, the electrocapillary number $Ca_E = RE_o^2\epsilon_o/\gamma$. Equation (3.16) now becomes

$$0 = -\kappa_z + \frac{3}{h^2}(h^2 v_z)_z + Ca_E \beta E E_z, \tag{3.28}$$

but Eqs. (3.17) and (3.18) remain the same.

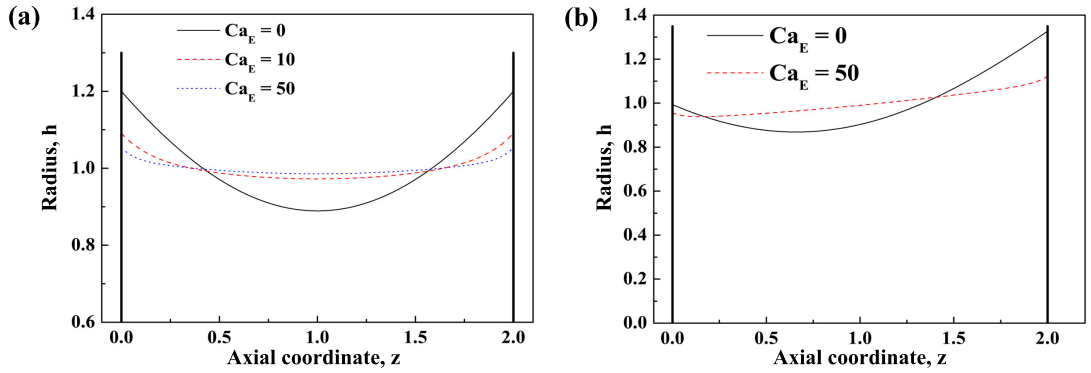

Figure 3.7: (a) Equilibrium bridge shapes for $Ca_E = 0$ (solid line), 10 (dashed line), and 50 (dotted line) when $\Delta\theta_r$ is 0° ($\theta_{\text{bottom}} = 60°$, $\theta_{\text{top}} = 60°$). (b) Equilibrium bridge shapes for $Ca_E = 0$ (solid line) and 50 (dashed line) when $\Delta\theta_r$ is 10° ($\theta_{\text{bottom}} = 70°$, $\theta_{\text{top}} = 60°$). Here, $\beta = 1.74$.

Figure 3.7(a) shows equilibrium bridge shapes for $Ca_E = 0$, 10, and 50 when $\Delta\theta_r$ is 0°. The results are similar to those in Fig. 3.5. The electrostatic contribution to the pressure reduces the pressure difference in the bridge, leading to flatter shape as Ca_E increases. (The initial radius is 1). However, if we use these equilibrium shapes as initial conditions and stretch the bridge, the transfer ratio is still 50% due to the absence of a wettability difference. Therefore, we use the equilibrium bridge shapes shown in Fig. 3.7(b), where $\Delta\theta_r = 10°$, as initial conditions. We again focus on relatively high stretching speeds and set $Ca = 1$.

In Fig. 3.7(b), because the top surface is more wettable, the top contact radius is larger than the bottom contact radius when both the electrified and non-electrified bridges reach equilibrium. As a consequence, the narrowest bridge radius is closer to the bottom plate in both cases. When the equilibrium shape is taken to be the initial condition, the transfer ratio of the non-electrified bridge is 72%, and the transfer ratio of the electrified bridge is 79% (Table 3.3). The transfer ratio of both bridges increases compared to the case where perfect-cylinder initial conditions are used. Even though the transfer ratio of the non-electrified bridge increases about 20% with this change in initial condition, the transfer ratio of the electrified bridge is still larger than that of the non-electrified bridge.

The transfer ratio of the non-electrified bridge increases about 20% because more

Table 3.3: Comparison of transfer ratios for different initial bridge shapes

Initial shape	$\chi = 0$	$\chi = 50$
Perfect cylinder	53%	76%
Equilibrium shape	72%	79%

than 50% of the liquid is initially close to the top surface. Figure 3.7(b) shows the top contact radius of non-electrified liquid bridge is 30% larger than its bottom contact radius. Since the contact-line motion is relatively small due to the weaker surface-tension forces when $Ca = 1$, the initial shape has a significant influence on the final bridge shape and thus the transfer ratio.

The transfer ratio of the electrified bridge only increases 3% when an equilibrium initial shape is used. Because the electrostatic contribution to the pressure leads to a flatter bridge shape, the contact radii are still close to 1 (Fig. 3.7(b)) like with a perfect-cylinder initial shape. However, when an equilibrium initial shape is used, the amount of liquid transferred is still higher when the electric field is present. This suggests that even with equilibrium initial shapes, applying an electric field can still enhance the amount of liquid transferred.

3.4 Results: Leaky dielectrics

For leaky dielectric liquids, the governing equations are Eqs. (3.16)-(3.19). Two more parameters need to be considered: the surface charge density σ and the liquid conductivity K. The surface charge can produce a tangential stress when an electric field is present. This tangential stress can be obtained by substituting Eq. (3.12) into the Maxwell-stress part of Eq. (3.7) [33] and keeping the leading-order term. In dimensionless form we have

$$\| \mathbf{n} \cdot \boldsymbol{\sigma}^M \cdot \mathbf{t} \| = \sigma \chi E. \tag{3.29}$$

The magnitude of this stress is determined by the surface charge density (σ) and the strength of the electric field (χE) along the liquid-air interface. Note that the sign of this term depends on the signs of σ and E (since $\chi > 0$).

3.4.1 Role of tangential stresses

We first study how the surface charge density and liquid conductivity influence the equilibrium bridge shape. The initial shape is a perfect cylinder with an initial aspect ratio of $\Lambda = 1$. Both the top and bottom contact angles are set to 60°, which means that the wettability difference $\Delta\theta_r = 0$. The electrocapillary number Ca_E is set to 0 or 50 (The electroviscous number χ in Eq. (3.29) is replaced by Ca_E when the plates are stationary (Sec. 3.3).) We set the dimensionless conductivity K^* to 1, and the initial surface charge density σ_o to 0 or 0.1 (the latter corresponds to 8.9 $\times 10^{-7}$ C/m^2 for a potential difference of 1 kV over a 1 mm distance). The value of σ_o we use is smaller compared to the values used by Feng [43] when studying electrospinning, but this value is enough to have a significant influence on the bridge shape.

Figure 3.8(a) shows that when the initial surface charge density is 0.1, the bridge shape is asymmetric even though no wettability difference is present. In contrast, the bridge shape is symmetric when no initial surface charge is present, and is very close in shape to what is observed for the corresponding perfect-dielectric case.

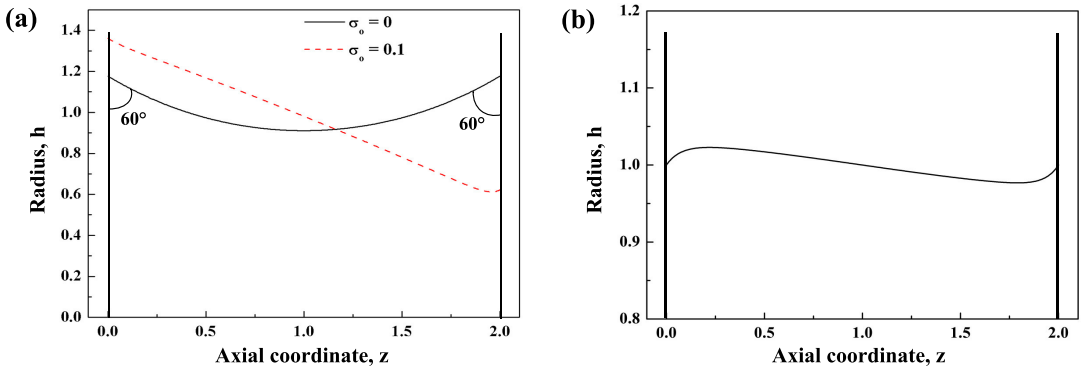

Figure 3.8: (a) Comparison of equilibrium bridge shapes between the cases where $\sigma_o = 0$ (solid line) and 0.1 (dashed line). The wettability difference $\Delta\theta_r = 0°$ with both the top and bottom contact angles set to 60°. (b) Equilibrium bridge shape for the case where $\sigma = 0.1$ and both contact lines are fixed at 1. Values of other parameters are $Ca_E = 50$, $K^* = 1$, and $\beta = 1.74$.

To remove the effect of contact-line motion and understand the influence of the surface charge density, we perform additional calculations in which the contact lines are fixed. Figure 3.8(b) shows the equilibrium bridge shape with fixed contact lines when σ_o

= 0.1. When the bridge reaches equilibrium, the radius of the bridge near the bottom plate increases about 2%. As in Fig. 3.8(a), this indicates that the presence of surface charge tends to push liquid to the bottom plate.

We now discuss the reason why liquid is pushed from top plate to the bottom plate when σ_o is sufficiently large. The key is the sign of the electrostatic contribution to the tangential stress, given by Eq. (3.29). When this quantity is negative, the tangential electrostatic stress points in the negative-z direction. In our calculations, the electrocapillary number Ca_E and the surface charge density are positive. Because the top plate has a positive electrostatic potential and $E = -\nabla\phi$, the direction of electric field points toward the bottom plate. Therefore, the direction of the tangential electrostatic stress is from the top to the bottom plate. If we want the tangential electrostatic stress to point the top plate, we would either need the initial surface charge density to be negative or we could reverse the direction of the electric field by using a positive electrostatic potential at the bottom plate while keeping the top plate grounded. This suggests that the direction of the tangential electrostatic stress can be manipulated to enhance liquid transfer to the top surface.

Figure 3.8(a) also implies that conductivity alone does not induce enough surface charge to significantly influence bridge shape. Additional calculations we have performed indicate that even if the conductivity is increased by an order of magnitude, the bridge shape changes very little when $\sigma_o = 0$. In contrast, if the initial surface charge density is taken to be 0.1 and the conductivity is lowered to 0, the bridge shape closely resembles that obtained when $K^* = 1$ (Fig. 3.8(a)), although the asymmetry is not as pronounced. This indicates that the initial surface charge density plays a dominant role in determining bridge shape.

3.4.2 Liquid transfer

We now study liquid transfer in leaky dielectrics. The initial bridge is again a cylinder with an initial aspect ratio $\Lambda = 1$, the top contact angle is 60° while the bottom contact angle varies, and the electroviscous number χ is set to 0 or 50.

From Fig. 3.8, we see that liquid is pushed to the bottom surface when $\sigma_o = 0.1$. Such an initial shape may decrease the transfer ratio relative to the case where electrostatic effects are absent. To increase the amount of liquid transferred to the top

surface, the tangential electrostatic stress should point toward that surface. Therefore, here we set the initial surface charge density to $\sigma_0 = -0.1$ which is opposite to the sign used in the previous section.

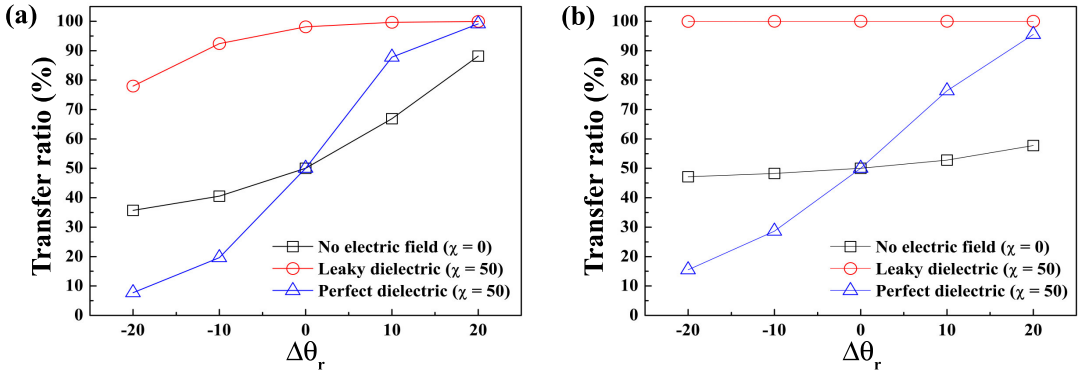

Figure 3.9: Relationship between transfer ratio and wettability difference when $\chi = 0$ and $\chi = 50$ at (a) $Ca = 0.1$ and (b) $Ca = 1$. Here θ_{top} is 60° and θ_{bottom} varies. Values of other parameters are $K^* = 1$, σ = -0.1, and $\beta = 1.74$.

Figure 3.9 shows the transfer ratio with and without the presence of an electric field at $Ca = 0.1$ and 1. Also plotted are the transfer-ratio values from Fig. 3.3 for the case of perfect dielectrics. For leaky dielectrics, the transfer ratio increases significantly even when the bottom plate is more wettable than the top plate ($\Delta\theta_r < 0$). When the electric field is not present and $\Delta\theta_r$ is negative, the transfer ratio is less than 50% for both capillary numbers. However, for leaky dielectrics, the tangential electrostatic stress significantly enhances the amount of liquid transferred. Since the electric field is pointing in the negative-z direction and the sign of the surface charge is negative, the tangential electrostatic stress is always positive (pointing in the positive-z direction) and drives more liquid to the top plate.

Figure 3.10 illustrates the electrified and non-electrified bridge shapes at different times when $Ca = 0.1$ and shows how the tangential electrostatic stress enhances liquid transfer to the top surface. At the beginning of stretching (Fig. 3.10(a)), both bridges quickly evolve to have shapes that satisfy the contact-angle boundary conditions. The bottom contact line of the electrified liquid bridge retreats faster than that of the non-electrified liquid bridge because the tangential electrostatic stress drives liquid to the top plate. At $t = 0.71$ (Fig. 3.10(b)), the bottom contact-line position of the electrified

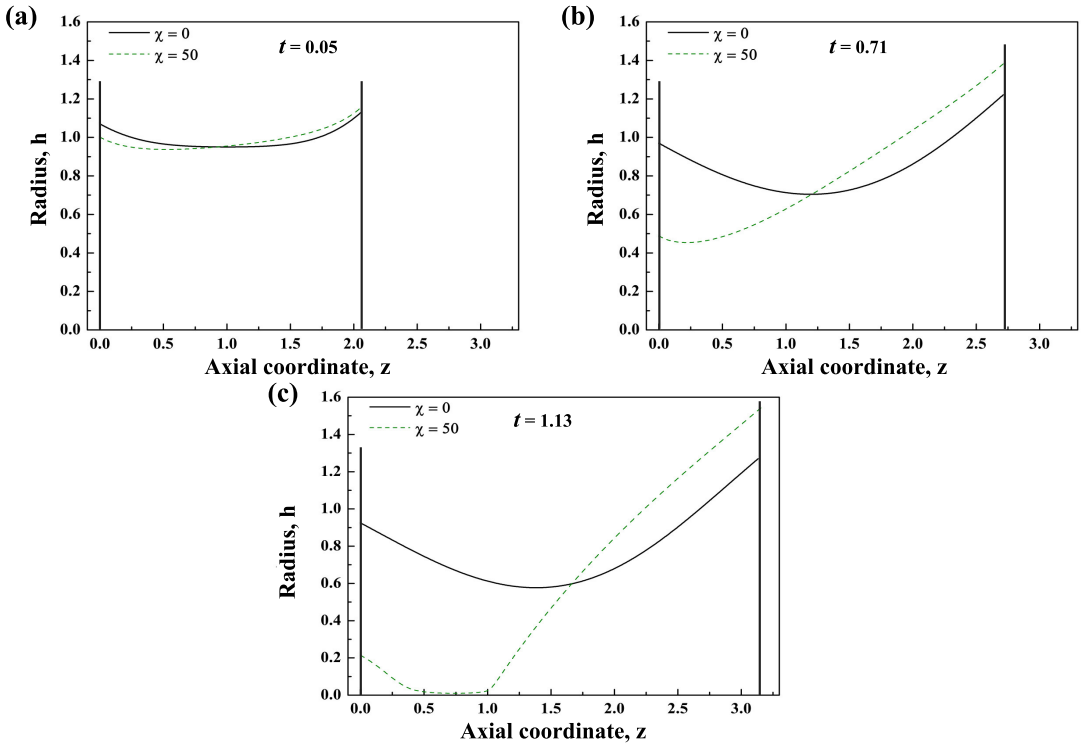

Figure 3.10: Comparison of electrified and non-electrified bridge shapes at different times for the case where $\Delta\theta_r = 10^\circ$ ($\theta_{\text{bottom}} = 70^\circ$, $\theta_{\text{top}} = 60^\circ$) at $Ca = 0.1$. Values of other parameters are σ_o = -0.1, $K^* = 1$, and $\beta = 1.74$. The breakup time for the electrified bridge is 1.1 and the breakup time for the non-electrified bridge is 2.1.

liquid bridge is only half of its initial value, and the minimum bridge radius is very close to the bottom plate. As a result, most of the liquid transfers to the top plate when the electrified bridge breaks at $t = 1.1$ (Fig. 3.10(c)). In contrast, the non-electrified bridge breaks at $t = 2.1$. Thus, not only is the transfer ratio enhanced in leaky dielectric materials, the breakup time is also reduced. The breakup time for the corresponding perfect dielectric case is 2.4, which is larger than that for the non-electrified bridge due to the electrostatic stabilization (Sec. 3.2).

We now summarize the results of some additional calculations we have performed. First, if we pin the top contact line and let the bottom contact line slip (similar to Fig. 3.4), nearly all of the liquid is transferred to the top plate (similar to Fig. 3.9) due to the tangential electrostatic stress. Second, similar behavior to that shown here is observed if an equilibrium bridge is used as the initial condition rather than a perfect cylinder. Third, as in the static case, the initial surface charge density plays a more dominant role than conductivity. If the calculations are repeated for the same value of σ_o but with $K^* = 0$, the behavior of the transfer ratio is similar to that for the case of non-zero conductivity (with the transfer ratio being slightly smaller). If the calculations are repeated with non-zero conductivity but zero initial surface charge density, the behavior of the transfer ratio is similar to that for perfect dielectrics due to the small amount of induced charge. Thus for leaky dielectrics, electrostatic effects are strongest when both the initial surface charge density and conductivity are non-zero, and weakest when the initial surface charge density is zero. This is consistent with Eq. (3.29), which shows that the tangential electrostatic stress is directly proportional to the surface charge density.

3.5 Experiments

Although the primary purpose of this paper is to use slender-jet models to advance fundamental understanding of electrostatic assist, we have also performed some simple flow visualization experiments to further examine how electrostatic forces can influence liquid transfer.

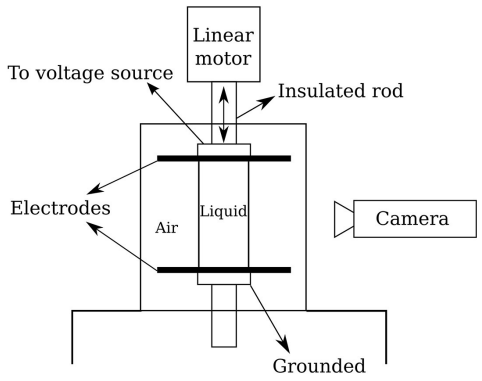

Figure 3.11: Schematic of experimental apparatus

3.5.1 Experimental setup

The experimental apparatus is shown in Fig. 3.11. This apparatus consists of two parallel plates made of polished aluminum (12.6 mm diameter; Ted Pella, Inc.) in an enclosed container. To provide a wettability contrast, for some experiments a polystyrene (PS)-covered polished aluminum bottom plate was used. The PS covered plate was fabricated by spin coating a 1 wt% solution of PS (MW 12000; Polysciences Inc.) in toluene at 2000 rpm for 60 s using a Headway Research Inc. PWM32 spinner system. The plates are separated using a motor (Parker Compumotor), and a voltage difference can be applied (Spellman SL-130 Series High Voltage Power Supply).

An 88 wt% glycerol-distilled water solution is used in the experiments. Its viscosity is 119.6 ± 1.0 cP (Brookfield DV-II viscometer), surface tension is 66.5 ± 0.2 mN/m (Kruss Digital Tensiometer K10ST), relative permittivity is 45.9 ± 0.4 (Scientifica 870 Dielectric Constant Meter), and conductivity is 0.4 ± 0.1 μS/cm (Thermo Scientific Orion Conductivity Benchtop Meter). The receding contact angles of the solution on the polished aluminum specimen and PS-coated surfaces were measured to be $13^\circ \pm 2^\circ$ and $58^\circ \pm 2^\circ$, respectively (Kruss DSA30S).

A high-speed camera (Photron FASTCAM-ultima APX with an NEC Navitar Zoom 6000 lens system) is used to visualize bridge stretching with the help of a light source on the other side of the apparatus. The experimental results are analyzed using the ImageJ software. We use Pappus' theorem to calculate the volumes of the initial bridge and of the droplets that rest on the plates after stretching is complete [89]. Pappus'

theorem generates the volume of a liquid droplet by revolution of the droplet's cross-sectional area in the r-z plane. This method assumes that the droplet is axisymmetric. Even though the droplets in the experiments will not be perfectly axisymmetric, the calculated total droplet volume before and after bridge stretching is typically within 5% of the expected volume of 2 μL.

3.5.2 Results: Two identical surfaces

As a benchmark, we first present results for the case where both plates are identical. In the absence of electrostatic forces, we would expect a transfer ratio of 50% (assuming that gravitational effects are negligible) due to the symmetry of the problem. In the presence of electrostatic forces, we would expect a transfer ratio of 50% if the liquid behaves like a perfect dielectric (Sec. 3). However, if the initial surface charge density plays a significant role, this would break the problem symmetry and we would expect a much different value of the transfer ratio (Sec. 4).

We performed experiments using the polished aluminum plates. A 2 ± 0.06 μL drop of the glycerol-water solution was placed on the bottom plate. The top plate was lowered to come into contact with the droplet until the distance between two surfaces was about 0.45 mm, which enabled us to obtain initial contact radii that were approximately equal on both plates. We then increased the distance between the two plates to approximately 1.1 mm to prevent electrostatic discharge upon application of an electrostatic potential difference. After this step, an electrostatic potential difference of 1 kV ($Ca_E \approx 0.1$) was applied in one set of experiments until the bridge reached an equilibrium (static) shape (This value of the potential difference is large enough to cause a change in bridge shape but low enough to avoid discharge.) Then, the bridge was stretched until it broke. Each experiment (with and without the electric field) was repeated at least three times.

A stretching speed of approximately 6.25 mm/s was used. Scaling length with the characteristic bridge radius, which is $\sim$ 1 mm, yields $Ca \sim 0.01$, $Re \sim 0.06$, and $Bo \sim 0.1$, respectively. These values imply that surface-tension forces are considerably stronger than viscous, inertial, and gravitational forces. The electroviscous number is $\chi \approx 10$, and the value of the electrocapillary number is $Ca_E = \chi Ca \approx 0.1$. The value of the latter parameter implies that although electrostatic forces are weaker than surface-tension forces, they could still influence bridge behavior. The charge relaxation

time $\epsilon\epsilon_o/K$ is $\sim$10 μs, which is much smaller than the time scale for the completion of stretching, $\sim$ 0.1 s. This implies that conductivity will likely play a minor role.

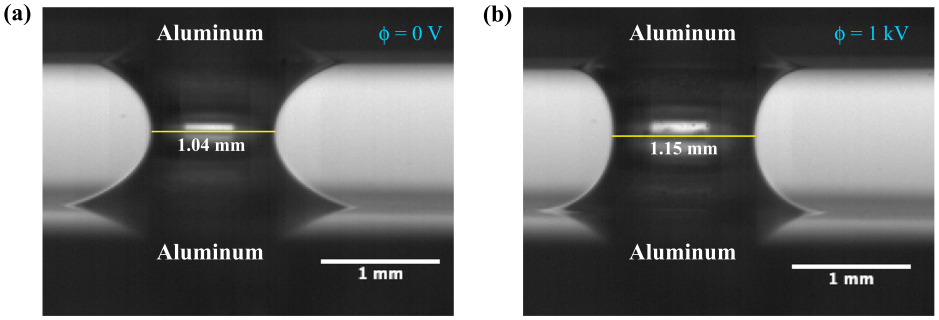

Figure 3.12: Visualizations of static liquid bridge shapes between two aluminum surfaces (a) without an electrostatic potential difference ($Ca_E = 0$) and (b) with an electrostatic potential difference of 1 kV ($Ca_E \approx 0.1$).

Figure 3.12 shows visualizations of static liquid bridge shapes. In the absence of an electrostatic potential difference, the narrowest bridge diameter is 1.04 mm (Fig. 3.12(a)). In the presence of an electrostatic potential difference, the narrowest bridge diameter is larger, 1.15 mm (Fig. 3.12(b)). These experimental results are qualitatively consistent with the 1D model predictions (Fig. 3.7).

Table 3.4: Mean transfer ratios and bridge breakup lengths when both surfaces are identical

	Transfer ratio	Breakup length
$\phi = 0$ V	49.7% $\pm$ 1%	1.66 $\pm$ 0.05 mm
$\phi = 1$ kV	50.2% $\pm$ 1%	2.63 $\pm$ 0.03 mm

After characterizing static bridge shapes, experiments involving bridge stretching were performed, and the results are summarized in Table 3.4. When the electrostatic potential difference is absent, the mean transfer ratio is 49.7% $\pm$ 1%. When the eletrostatic potential difference is present, the mean transfer ratio is 50.2% $\pm$ 1%. Based on these results, we conclude that there is no significant difference in the transfer ratio when the plates are identical and an electric field is applied. These results suggest that the influence of surface charge (and the associated tangential stresses) are negligible in these experiments. We note that in these experiments, the contact lines appear to be pinned, possibly due to the presence of surface heterogeneities.

Table 3.4 also shows that the bridge breakup length is larger when the electric field is present (2.63 ± 0.03 mm vs. 1.66 ± 0.05 mm). Since electrostatic forces tend to stabilize the bridge, the bridge can be stretched longer without breaking compared to the case where the electric field is absent. These results are qualitatively consistent with the predictions of the perfect dielectric model (Fig. 3.3(a)).

3.5.3 Results: Two different surfaces

We now consider the case where the two surfaces are different. Polished aluminum is used for the top plate, and PS-coated aluminum is used for the bottom plate. We found that by using the method described in Sec. 5.2, we had difficulty obtaining initial bridge shapes that were consistent for each run, presumably due to surface heterogeneities. Instead, we used a slightly different method for creating the bridges.

A 2 ± 0.06 μL drop of the glycerol-water solution was placed on the bottom plate. The top plate was lowered until the distance between the two plates was approximately 1 mm (This distance was controlled by plastic shims (Artus Corp.)) At this distance, the top plate is not yet in contact with the droplet. An electrostatic potential difference of about 1 kV was then applied, causing the droplet to stretch and come into contact with the top plate, forming a liquid bridge. In some experiments, the electrostatic potential was then turned off until the bridge reached an equilibrium shape and then the bridge was stretched. In other experiments, the electrostatic potential difference was increased to 1.5 kV ($Ca_E \approx 0.27$), an equilibrium bridge shape was reached, and then the bridge was stretched. Each set of experiments was performed at least three times. We used the same stretching speed as in Sec. 3.2, so surface-tension forces are again expected to play a key role.

Figure 3.13 shows images of bridge shapes before stretching and right after breakup. Table 3.5 summarizes the results. In the experiments without the electric field, both top and bottom contact lines are pinned during stretching, which we suspect occurs due to the presence of surface heterogeneities. In the experiments with the electric field, the top contact line remains pinned but the bottom contact line retreats and then expands during stretching. The transfer ratio without the electric field is 34% ± 2%, and the transfer ratio with the electric field is 42% ± 2%. These results show that the transfer ratio increases when the electric field is present. Furthermore, the average breakup

length of the non-electrified bridge is 2.06 ± 0.01 mm (Fig. 3.13(b)), but the average breakup length of the electrified bridge is longer, 3.03 ± 0.08 mm (Fig. 3.13(d)).

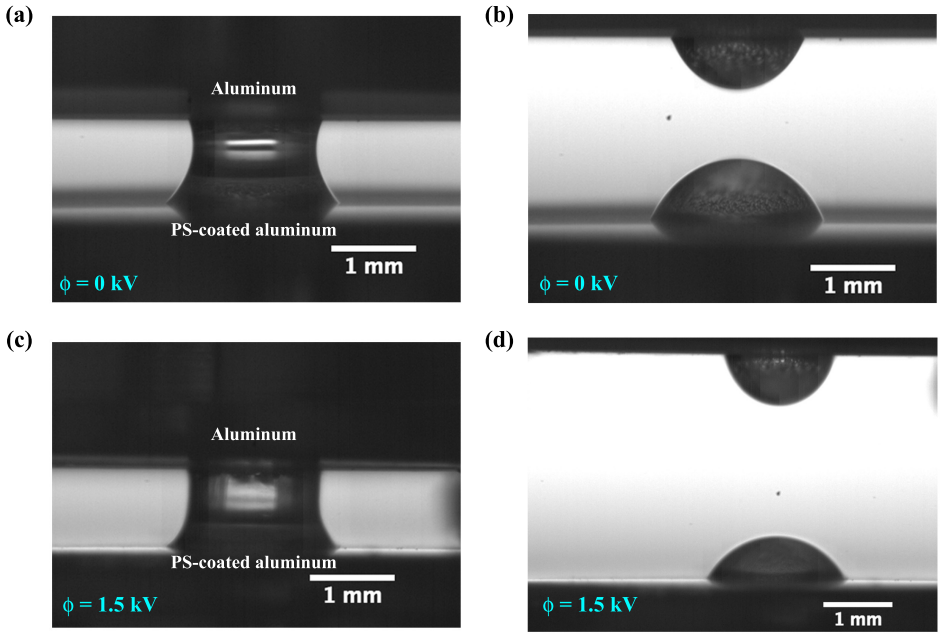

Figure 3.13: Visualizations of the liquid bridge (a) before stretching and (b) after liquid bridge breaks without application of an electrostatic potential difference ($\chi = 0$). Visualizations of the liquid bridge (c) before stretching and (d) after application of an electrostatic potential difference of 1.5 kV ($\chi \approx 27$).

Table 3.5: Contact line motion, transfer ratio and the breakup length in the experiments with two different surfaces

	Top contact line	Bottom contact line	Transfer ratio	Breakup length
$\phi = 0$ V	Pinned	Pinned	34% ± 2%	2.06± 0.01 mm
$\phi = 1.5$ kV	Pinned	Free	42% ± 2%	3.03 ± 0.08 mm

We now discuss how the electric field influences bridge deformation and thus the transfer ratio. Before the bridge is stretched, the shapes of both liquid bridges are slightly different. The mean top and bottom contact radii of both bridges are 0.80 ± 0.03 mm and 1.10 mm ± 0.02 mm, respectively. The mean narrowest bridge diameter of the electrified bridge is 1.54 ± 0.01 mm, which is larger than that of the non-electrified bridge (1.46 ± 0.03 mm) (Figs. 3.13(a) and (c)).

During stretching, both contact lines of the non-electrified bridge are pinned. Therefore, the contact radii at the upper and lower plates have the same values after bridge breakup. For the electrified bridge, the top contact line does not slip, but the bottom contact line retreats at the beginning of stretching. The bottom contact line then expands when the bridge is about to break. The final bottom contact radius is slightly smaller (~ 0.03 mm) than its initial value.

The top contact lines for both cases are pinned. This pinning may be due to the receding contact angle of the polished aluminum surface being so small (13°) that the bridge breaks before the top contact angle reaches the receding value. When the electric field is not present, the bottom contact line is pinned, which may also be due to the small contact angle. However, the bottom contact line retreats for the electrified bridge.

When the electric field is present, electrostatic forces stabilize the bridge by increasing the narrowest bridge radius. Liquid must flow from the region near both contact lines to the middle of the bridge, so both the top and bottom contact angles decrease before stretching. As a consequence, the bottom contact angle reaches its receding value during stretching and the bottom contact line retreats, causing the transfer ratio to increase.

3.5.4 Comparison to model predictions

The experimental results suggest that the presence of the electric field can significantly influence contact-line motion. Thus, in comparing our model predictions to the experimental results, we examine all combinations of boundary conditions to advance fundamental understanding. These include the cases where (i) both the top and bottom contact lines are free to move, (ii) both the top and bottom contact lines are pinned, (iii) the top contact line is pinned and the bottom contact line is free to move, and (iv) the top contact line is free to move and the bottom contact line is pinned.

Figure 3.14(a) shows the initial bridge shapes used in our calculations. The initial shapes represent static bridge shapes and are generated using the procedure described in Sec. 3.3. The radii at the top and bottom plates have been chosen to match those in the experiments. As can be seen in Fig. 3.14(a), the contact angles at both the top and bottom plates of the electrified bridge are smaller than those of the non-electrified bridge. Also, the narrowest bridge radius of the electrified bridge is (0.74 mm) is slightly

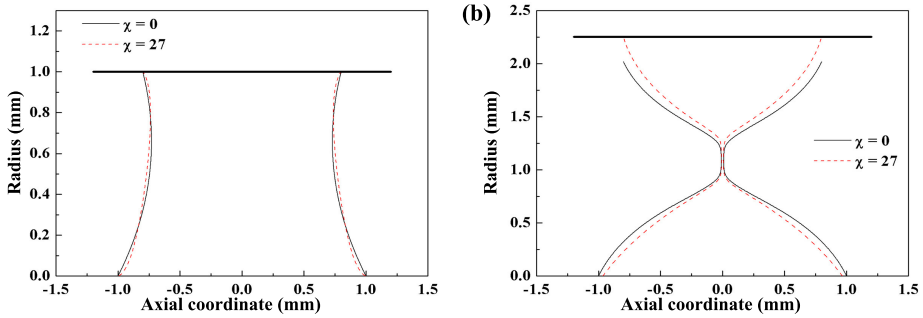

Figure 3.14: (a) Initial bridge shapes and (b) final bridge shapes with ($\chi = 27$; dashed line) and without ($\chi = 0$; solid line) the electric field. Both top contact radii are fixed at 0.8 mm. The bottom contact radius for the case where $\chi = 0$ is fixed at 1 mm, while the bottom contact radius for the case where $\chi = 27$ is free to move and the contact angle is 58°. Here, $\beta = 44.9$.

greater than that of the non-electrified bridge (0.73 mm). These values are comparable to what is observed in the experiments (0.77 ± 0.01 mm for the electrified bridge and 0.73 ± 0.01 mm for the non-electrified bridge); the discrepancy may be due to the lack of perfect axisymmetry in the experiments.

Table 3.6: Predicted transfer ratio and breakup length for different boundary conditions. The entries in boldface correspond to the conditions observed in the experiments.

Electric potential	Contact line boundary conditions			
	Top contact line	Bottom contact line	Transfer ratio	Breakup length
$\phi = 0$ V	**Pinned**	**Pinned**	**34.72%**	**2.03 mm**
	Pinned	Free	43.76%	2.16 mm
	Free	Pinned	62.92%	1.57 mm
	Free	Free	95.85%	1.35 mm
$\phi = 1.5$ kV	Pinned	Pinned	34.72%	2.03 mm
	Pinned	**Free**	**45.45%**	**2.25 mm**
	Free	Pinned	63.43%	1.57 mm
	Free	Free	95.93%	1.35 mm

Table 3.6 shows the calculated transfer ratios and breakup lengths for different boundary conditions. The entries in boldface correspond to the conditions observed in the experiments. We first compare these predictions with the experimental results, then discuss the influence of different boundary conditions.

In the experiments without the electric field, both contact lines are pinned during stretching. The transfer ratio and breakup length predicted by the 1D model with these

boundary conditions are 34.72% and 2.03 mm, respectively. These results agree well with the experimental results shown in Table 3.5. In the experiments with the electric field, the top contact line is pinned but the bottom contact line is free to move. Here, the predicted transfer ratio is 45%, which is close the experimental value of $42 \pm 2\%$. In the calculations, the bottom contact line first retreats and then expands when the liquid bridge is close to pinchoff. At the end of stretching, the bottom contact radius of the electrified liquid bridge decreases from 1 mm to 0.97 mm, which agrees well with the experimental result (0.97 mm).

Figure 3.14(b) shows the predicted bridge shapes after breakup. Note that the pinch-off points of both bridges are nearly the same, but the final length of the electrified bridge (2.25 mm) is larger than that of the non-electrified bridge (2.03 mm). Because the electrostatic forces decrease the pressure difference between the narrowest region of the liquid bridge and the bottom contact line as discussed in Sec. 3.2, the pinch-off point of the electrified bridge is closer to the bottom surface (Fig. 3.14(b)). Therefore, although the bottom contact line position decreases just 0.03 mm, the transfer ratio can increase by approximately 8%.

However, the predicted breakup length of the electrified bridge (2.25 mm) is smaller than the experimental value (3.03 mm). Since the transfer ratio is set by the overall bridge shape rather than the breakup length, the transfer ratio predicted by the 1D model still agrees well with the experiments. The discrepancy in the breakup length between experiment and theory may be due to neglecting the effect of the normal component of the electric field in the 1D model. Capturing this effect would require development of a full 2D model, a task we leave for future work.

Table 3.6 illustrates that the contact-line boundary conditions significantly influence the transfer ratio. Whether or not electrostatic effects are present, allowing one of the contact lines to move increases the transfer ratio. Allowing the bottom contact line to move has a larger influence, presumably due to the fact the narrowest diameter of the bridge is located near the bottom plate. The largest transfer ratio (and smallest breakup length) occurs when both contact lines are free to move.

Notably, even when the electric field is absent, allowing the bottom contact line to move yields a transfer ratio close to the experimental value. This indicates that the primary influence of electrostatics is through its influence on the boundary conditions.

Indeed, for the same boundary conditions, application of the electric field leads to an increase in the transfer ratio by only a modest amount. This can be rationalized by noting that the ratio of electrostatic to surface-tension forces, which is given by χCa, is equal to 0.27. Unfortunately, we were unable to further increase the strength of the electric field in the experiments due to electrostatic discharge. If we attempt to increase the capillary number by raising the liquid viscosity or stretching speed, the contact lines on both surfaces tend to pin since the stronger viscous forces oppose the capillary pressure gradients that drive contact-line slip.

Nevertheless, application of the electric field still has a significant influence on the transfer ratio since it leads to depinning of the contact line on the bottom plate. As discussed above, application of the electric field modifies the interface shape and causes the contact angle to drop below the receding value, thereby depinning the contact line.

3.6 Conclusions

In this work we have used slender-jet models to advance fundamental understanding of how electric fields can be used to improve liquid transfer. Application of an electric field lowers the pressure inside the liquid bridge. This causes the pressure difference between the bridge center and the more wettable plate to become larger relative to the pressure difference between the bridge center and the less wettable plate. As a result, more liquid is driven toward the more wettable plate. For leaky dielectrics, the electrostatic contribution to the tangential stress also plays a key role. If the sign of the initial surface charge density and the direction of the electric field are chosen appropriately, nearly all the liquid can be driven to the more wettable plate. More generally, our results suggest that the surface charge and electric field can be used to augment or oppose flows driven by wettability differences.

One of major challenges in high-speed printing is obtaining a transfer ratio greater then 50%. Our results indicate that application of electric fields can help overcome this challenge, and our work thus advances fundamental understanding of electrostatic assist (ESA), a method used in inudstrial printing processes to improve liquid transfer. Results from our flow visualization experiments reveal that electric fields can also significantly influence contact-line motion. Surface heterogeneities, which are not present in our

models, are likely important in the experiments and can lead to contact-line pinning. Electric fields can deform the liquid-air interface and cause the contact lines to unpin. By accounting for the different boundary conditions observed in the experiments, our models yield predictions consistent with the experimental observations.

Gravure printing, an industrial process to which ESA is applied, involves liquid transfer from a cavity to a flat surface. Describing liquid transfer in this configuration is beyond the reach of the slender-jet approach and requires full 2D (and even 3D [64]) models. Such models, along with more comprehensive experiments, will be necessary to more effectively apply ESA in the manufacturing of printed electronic devices.

Chapter 4

Electrostatic Assist of Liquid Transfer with Plates and Cavities

4.1 Introduction

4.1.1 Motivation

Printing processes have been widely used to make newspapers and books, and they are increasingly being applied to fabricate electronic devices such as transistors [14, 76, 77], solar cells [90], and radio frequency identification tags [78, 91]. In these printing processes, functional inks are deposited onto flexible substrates made of materials such as plastic [80, 92] or paper [79]. The flexible substrates are first unwrapped from a cylindrical roll and then wound up onto another cylindrical roll after printing and drying. Such roll-to-roll printing techniques have the potential to significantly reduce production costs and material waste [81] while still having high throughout ($\sim$1 m/s) [46, 77].

A printing process of particular interest for electronics-related applications is gravure printing (Fig. 4.1) [20]. The gravure roll contains a pattern of pixelated micron-scale cavities on its surface. After the cavities are filled with printing ink (often from a pan into which the gravure roll enters and then leaves), ink is transferred from the cavities to a substrate (supported by a backing roll). Gravure has the potential to create patterns having length scales of 10 μm or less [20].

For printed electronics, insufficient ink transfer from the cavities could lead to broken

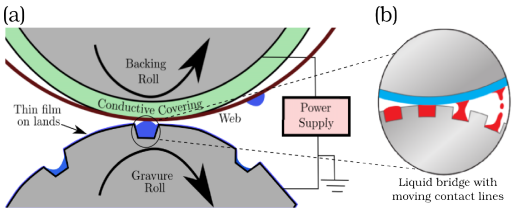

Figure 4.1: (a) Schematic of a gravure printing process with electrostatic assist (ESA). Ink is transferred from a cavity to a substrate, sometimes with the help of an electrostatic potential difference. (b) Schematic of a stretching liquid bridge.

circuits and failure of electronic devices. It has long been known that application of an electric field between the gravure roll and the substrate can help improve ink transfer, a technique is known as electrostatic assist (ESA) (Fig. 4.1) [3, 27, 83, 84]. However, the physical mechanisms underlying ESA remain poorly understood. A better understanding of these mechanisms would allow for more systematic design of ESA systems, which in turn would greatly help in reducing printing defects. The objective of this paper is to address this issue by examining the influence of electric fields on liquid transfer in two model geometries.

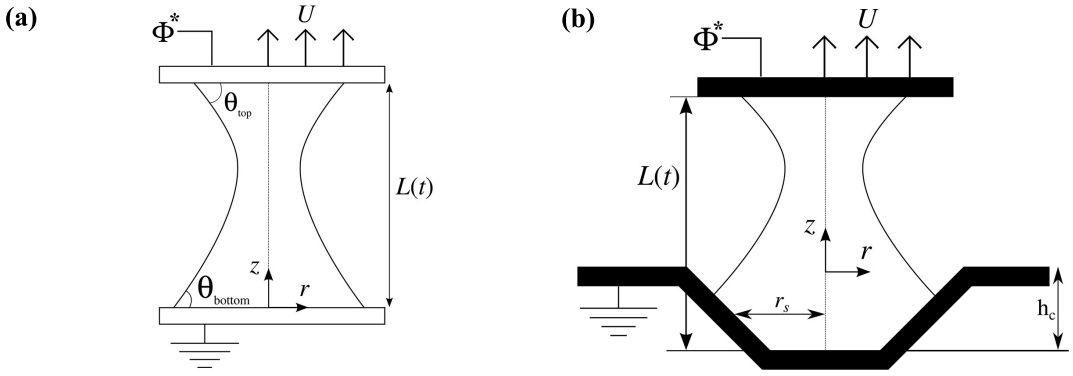

Figure 4.2: Schematic of model geometries considered in this work. A liquid bridge between (a) two flat surfaces (b) a flat surface and a cavity. The cavity bottom is located at $z = 0$.

Gravure printing processes involve the formation of a liquid bridge when ink transfers from a cavity to the substrate (Fig. 4.1). During liquid transfer, the liquid bridge is, in general, subject to extensional, shear, and rotational motions [26, 64]. Here, we consider the important limiting case of extensional motion where the liquid bridge is

stretched between a vertically moving flat plate and a stationary (i) flat plate or (ii) cavity. Schematics of the two model geometries are shown in Fig. 4.2. A constant electrostatic potential is applied to the top surface, while the bottom surface remains grounded. The contact lines (where the air, liquid, and solid intersect) may slip along each solid surface. We seek to determine how the electric field influences the dependence of liquid transfer on surface wettability and the geometry of the bottom surface.

4.1.2 Summary key findings from recent previous work

There have been a number of recent experimental [5, 6, 61] and theoretical [46, 54, 57, 63, 64, 93] studies on liquid transfer between two flat plates in the absence of an electric field. We provide here a summary of the key findings.

For liquid transfer in printing processes, inertial and gravitational forces are often negligible relative surface-tension and viscous forces due to the small length scales involved. Thus, the key parameter characterizing liquid transfer is the capillary number $Ca = \mu U/\gamma$, the ratio of viscous to surface-tension forces. Here, μ is the liquid viscosity, U is the stretching speed, and γ is the liquid surface tension. When Ca is less than $\sim$0.01, liquid transfer is dominated by the wettability of the surfaces [5, 54]. When Ca is $\sim$1, the stronger viscous forces tend to hinder contact-line movement and make wettability less important. As a result, only about 50% of the liquid is transferred from one surface to the other for a large range of wettability differences [6, 54].

There have also been a number of recent experimental [94] and theoretical [57, 63, 93, 95, 96, 97] studies on liquid transfer between a flat plate and a cavity in the absence of an electric field. In general, it is found that the amount of liquid transferred from the cavity is considerably less than 50%, even in the absence of a wettability difference between the cavity and flat plate. This occurs because of an apparent pinning of the contact line on the inclined walls of the cavity [57, 94]. Increasing Ca tends to increase the amount of liquid transferred because the stronger viscous forces reduce the slippage of the contact line on the flat plate [57]. However, it does not get above 50%.

The above results suggest that liquid transfer at high printing speeds is not influenced by wettability differences, and that transferring liquid from cavities is considerably more difficult than transferring liquid from a flat surface. As mentioned in section 4.1.1, one way to overcome these limitations is to apply an electric field. Although there is previous

work examining the influence of electric fields on liquid bridges that have pinned contact lines and are not being stretched [38, 39, 87, 88], very little work has been done to examine the fundamentals of stretching liquid bridges with moving contact lines in the presence of an electric field.

To address this knowledge gap, Huang and Kumar [82] developed a one-dimensional (1D) slender jet model of stretching liquid bridges with moving contact lines in the presence of an electric field. The considered both perfect dielectric and leaky dielectric liquids. They found that the electric field modifies the pressure differences inside the liquid bridge, and as a consequence, drives liquid toward the more wettable surface. For leaky dielectrics, charge can accumulate the liquid-air interface and further enhance liquid transfer, even to the less wettable surface. Thus, at high printing speeds ($Ca \sim 1$), application of an electric field can allow one to overcome the 50% limit on liquid transfer.

To complement their modeling work, Huang and Kumar [82] also performed a limited number of flow visualization experiments. These showed that application of an electric field modifies the shape of the liquid bridge and can cause depinning of the contact line (whereas it would remain pinned in the absence of the electric field). For the pair of surfaces considered by Huang and Kumar [82], measured values of the amount of liquid transferred are in good agreement with predictions of the 1D slender-jet model for perfect dielectrics.

4.1.3 Overview of present paper

Although the 1D slender-jet model is computationally efficient, it tends to overestimate contact-line motion as shown in our previous work on stretching liquid bridges in the absence of electric fields [54]. While it sometimes yields predictions that agree well with experiments [54, 82], an important open issue is how well predictions of the 1D model compare to those from a 2D axisymmetric model over a wide range of wettability differences in the presence of an electric field. Moreover, liquid transfer from a cavity cannot be described by a 1D model since the cavity geometry varies in the radial direction, making this an inherently 2D problem. Thus, in the present work we perform 2D calculations to advance fundamental understanding of how electric fields influence liquid transfer in the two model geometries shown in Fig. 4.2.

The mathematical model and computational scheme used in this work are presented

in section 2. In section 3, results are presented and discussed for liquid transfer between two flat plates. Both perfect dielectric and leaky dielectric liquids are considered, and predictions from the 2D model are compared to those from the 1D model of our previous work [82]. In section 4, liquid transfer from a cavity is considered, including an examination of the influence of cavity depth. Conclusions are summarized in section 5.

4.2 Problem formulation

Figure 4.2 shows the model geometries used in this work. We consider axisymmetric bridges of Newtonian liquids with constant density ρ, surface tension γ, viscosity μ, relative permittivity ϵ, and conductivity K confined between two electrodes. The top electrode is a flat horizontal plate moved vertically with a constant velocity U in the z-direction, and has a fixed electrostatic potential ϕ^*. The bottom electrode is stationary and grounded. It can either be flat and horizontal (Fig. 4.2(a)) or have the shape of a trapezoidal cavity (Fig. 4.2(b)).

The contact angle on the top electrode is θ_{top}, and that on the bottom electrode is θ_{bottom}. These contact angles may be a function of contact-line speed [75, 98], but we consider here the important limiting case where they are constant. We neglect any flow in the air outside the bridge. Table 4.1 lists order-of-magnitude values of key dimensional parameters.

Table 4.1: Order-of-magnitude values of key dimensional parameters

Parameter	Typical Values
Bridge radius R and bridge length L (mm)	$10^{-3} - 1$
Liquid viscosity μ (cP)	$1 - 10^2$
Surface tension γ (mN/m)	$10^1 - 10^2$
Stretching speed U (mm/s)	$1 - 10^2$
Voltage V (volt)	$10^2 - 10^4$
Conductivity K (S/m)	$10^{-12} - 10^{-6}$

Both perfect and leaky dielectric liquids are considered [32, 33, 35]. Perfect dielectrics are non-conductive but polarizable. Leaky dielectrics are also polarizable, but a finite conductivity allows charge to accumulate at the liquid-air interface when an electric field is present (charge is assumed to be negligible in the bulk). Thus, the electric field can act on both the polarized charge and the interfacial charge in leaky dielectrics.

The air phase is assumed to be a perfect dielectric with a relative permittivity of unity.

4.2.1 Governing equations

In the equations below, length is scaled by a characteristic initial bridge radius R, velocity by the constant stretching speed U, time by R/U, pressure by $\mu U/R$, electrostatic potential by ϕ^*, electric field by $E^* = \phi^*/L(0)$ where $L(0)$ is a characteristic initial bridge length, and charge density by $\epsilon_o E^*$ where ϵ_o is the free-space permittivity.

The electric field in each phase is given by $\mathbf{E}_i = -\nabla\phi_i$, where the electrostatic potentials ϕ_i are governed by Laplace's equation,

$$\nabla^2\phi_i = 0, \tag{4.1}$$

with $i = 1$ for liquid and $i = 2$ for air. The boundary conditions at the top and bottom electrode are

$$\phi_i = \begin{cases} 0 & \text{for } z = 0 \\ 1 & \text{for } z = L(t). \end{cases} \tag{4.2}$$

At the liquid-air interface, the surface charge density q is equal to the jump in the normal component of the electric field [33],

$$q = \parallel \epsilon_i \mathbf{E}_i \parallel \cdot\mathbf{n}, \tag{4.3}$$

where ϵ_i is the relative permittivity of each phase, $\mathbf{n}$ is the outward unit normal vector pointing into the air, and $\parallel ... \parallel$ is the jump operator which denotes the quantities in the air phase minus those in the liquid phase. Note that we set $\epsilon_1 = \epsilon$ and $\epsilon_2 = 1$. The tangential components of the electric field are continuous at the liquid-air interface,

$$\parallel \mathbf{E}_i \parallel \cdot\mathbf{t} = 0, \tag{4.4}$$

where $\mathbf{t}$ is the unit tangent vector to the liquid-air interface.

The charge at the liquid-air interface is governed by the conservation equation

$$\frac{\partial q}{\partial t} + \mathbf{v}\cdot\nabla_s q = q\mathbf{n}\cdot(\mathbf{n}\cdot\nabla)\mathbf{v} + \parallel -K^*\mathbf{E}_i \parallel \cdot\mathbf{n} + \frac{1}{Pe}\nabla_s^2 q, \tag{4.5}$$

where $\mathbf{v}$ is the velocity vector, $\nabla_s = (\mathbf{I} - \mathbf{nn})\cdot\nabla$ is the surface gradient operator, $K^* = RK/U\epsilon_o$ is the dimensionless conductivity, and $Pe = RU/D_s$ is the Peclet number

with D_s being the surface-charge diffusion coefficient. The last term corresponds to charge diffusion along the interface and is usually neglected [33]. However, we keep this term to resolve large charge gradients that form near the contact lines [44]. No-flux conditions are applied to the charge at each solid surface.

With the scales mentioned above, we can define a Reynolds number $Re = \rho UR/\mu$, Bond number $Bo = \rho g R^2/\gamma$, and electroviscous number $\chi = RE^2\ \epsilon_o/\mu U$, where g is the acceleration due to gravity. The physical meaning and typical values of these and other dimensionless parameters are listed in Table 4.2. We choose to focus on the regime where Bo and Re are small so that gravitational and inertial forces can be neglected and thus set $Bo = Re = 0$.

Table 4.2: Dimensionless problem parameters

Parameter	Definition	Physical meaning	Value
Bo	$\rho g R^2/\gamma$	$\frac{\text{Gravitational forces}}{\text{Surface-tension forces}}$	$10^{-7} - 1$
Re	$\rho UR/\mu$	$\frac{\text{Inertial forces}}{\text{Viscous forces}}$	$10^{-5} - 10^{2}$
Ca	$\mu U/\gamma$	$\frac{\text{Viscous forces}}{\text{Surface-tension forces}}$	$10^{-5} - 1$
χ	$RE_o^2\epsilon_o/\mu U$	$\frac{\text{Electrostatic forces}}{\text{Viscous forces}}$	$10^{-5} - 10^{11}$
Ca_E	$RE_o^2\epsilon_o/\gamma$	$\frac{\text{Electrostatic forces}}{\text{Surface-tension forces}}$	$10^{-10} - 10^{11}$
ϵ		Relative permittivity	$1 - 10^{1}$
K^*	$(R/U)/(\epsilon_o/K)$	$\frac{\text{Time scale for stretching}}{\text{Characteristic time for electric phenomena}}$	$10^{-6} - 10^{5}$
Λ	$L(0)/2R$	$\frac{\text{Initial bridge length}}{\text{Initial bridge diameter}}$	1

The velocity and pressure in each phase are denoted as $\mathbf{v}_i$ and P_i. Because we neglect the dynamics of the air phase, we set $\mathbf{v}_2 = 0$ and $P_2 = 0$, and let $\mathbf{v}_1 = \mathbf{v}$ and $P_1 = P$. The mass and momentum conservation equations for the liquid are

$$\nabla \cdot \mathbf{v} = 0, \tag{4.6}$$

$$-\nabla P + \chi \nabla \cdot \boldsymbol{\sigma}_1^M + \nabla^2 \mathbf{v} = 0, \tag{4.7}$$

where $\boldsymbol{\sigma}_i^M = \epsilon_i \mathbf{E}_i \mathbf{E}_i - \frac{1}{2}\epsilon_i \mathbf{E}_i \cdot \mathbf{E}_i \mathbf{I}$ is the dimensionless Maxwell stress tensor, with $\mathbf{I}$ being the identity tensor (We have scaled $\boldsymbol{\sigma}_i^M$ by $\epsilon_o (E^*)^2$.) Because the divergence of the Maxwell stress tensor is zero for perfect and leaky dielectrics [33], electrostatic and hydrodynamic phenomena are connected through the normal and tangential stress balances (Eq. (4.9) and (4.10)) at the liquid-air interface [45].

At the liquid-air interface, we impose the kinematic condition,

$$\mathbf{n} \cdot (\mathbf{v} - \dot{\mathbf{x}}) = 0, \tag{4.8}$$

where $\dot{\mathbf{x}}$ is the interface velocity. The normal stress balance is given by

$$\| \mathbf{n} \cdot \mathbf{T}_i \cdot \mathbf{n} \| = -\frac{\kappa}{Ca}, \tag{4.9}$$

where $\mathbf{T}_i = -P_i\mathbf{I} + [\nabla\mathbf{v}_i + (\nabla\mathbf{v}_i)^T] + \chi\boldsymbol{\sigma}_i^M$ is the total stress tensor, Ca is the capillary number, and $\kappa = \nabla_s \cdot \mathbf{n}$ is the interface curvature. The tangential stress balance is

$$\| \mathbf{n} \cdot \mathbf{T}_i \cdot \mathbf{t} \| = 0, \tag{4.10}$$

where $\mathbf{t}$ is the unit tangent vector to the liquid-air interface. The normal and tangential components of the Maxwell stress can be written as

$$\| \mathbf{n} \cdot \boldsymbol{\sigma}_i^M \cdot \mathbf{n} \| = \frac{\chi}{2} \| \epsilon_i(\mathbf{E}_i \cdot \mathbf{n})^2 - \epsilon_i(\mathbf{E}_i \cdot \mathbf{t})^2 \|, \tag{4.11}$$

$$\| \mathbf{n} \cdot \boldsymbol{\sigma}_i^M \cdot \mathbf{t} \| = q\chi(\mathbf{E}_i \cdot \mathbf{t}). \tag{4.12}$$

Note that the tangential component of the electric field is continuous at the liquid-air interface (Eq. (4.4)).

We apply the no-penetration and no-slip conditions at each solid surface,

$$\mathbf{n}_{\text{wall}} \cdot \mathbf{v} = \begin{cases} 0 & \text{for } z = 0 \\ 1 & \text{for } z = L(t), \end{cases} \tag{4.13}$$

$$\mathbf{t}_{\text{wall}} \cdot \mathbf{v} = 0 \quad \text{at } z = 0, L(t), \tag{4.14}$$

where $\mathbf{n}_{\text{wall}}$ is the unit normal vector pointing in the positive z-direction, $\mathbf{t}_{\text{wall}}$ is the unit tangential vector pointing in the radial direction, and $L(t)$ is the location of the top plate.

We apply symmetry boundary condition at the bridge axis,

$$\mathbf{t}_{\text{symm}} \cdot (\mathbf{n}_{\text{symm}} \cdot \mathbf{T}) = 0, \tag{4.15}$$

$$\mathbf{n}_{\text{symm}} \cdot \mathbf{v} = 0, \tag{4.16}$$

where $\mathbf{n}_{\text{symm}}$ and $\mathbf{t}_{\text{symm}}$ are the unit vectors normal and tangent to the symmetry line.

To deal with the dynamic contact line, we replace Eq. (4.14) with a Navier slip condition at each contact line, and fix the contact angle instead of the contact-line position,

$$\mathbf{t}_{\text{wall}} \cdot (\mathbf{n}_{\text{wall}} \cdot \mathbf{T}) = \frac{1}{\beta}\mathbf{t}_{\text{wall}} \cdot (\mathbf{v} - \mathbf{v}_{\text{wall}}), \tag{4.17}$$

$$\mathbf{n}_{\text{wall}} \cdot \mathbf{n} = \cos\theta, \tag{4.18}$$

where $\mathbf{n}_{\text{wall}}$ (which points toward the liquid side) and $\mathbf{t}_{\text{wall}}$ are unit normal and tangent vectors to each solid surface, β is a dimensionless slip coefficient, and $\mathbf{v}_{\text{wall}}$ is the wall velocity. For all computations, the value of β is set to 10^{10} to produce a contact line with negligible shear stress [54, 57, 63], but the results are essentially independent of β down to value of 0.1. Here, $\theta = \theta_{\text{bottom}}$ at the bottom surface and $\theta = \theta_{\text{top}}$ at the top surface. Note that we only impose Eq. (4.17) and (4.18) at the node located on the contact line and no-slip condition is applied on the rest of the solid surface, i.e., the slip length is less than the size of an element [54, 57, 63].

As shown in Fig. 4.2, we consider two model geometries. The cavity wall (Fig. 4.2(b)) is defined by a hyperbolic tangent function [54, 57, 63],

$$z = \frac{1}{2}\delta\left(1 + \tanh\left(\frac{r - r_s}{r_d}\right)\right), \tag{4.19}$$

where z and r are axial and radial positions of the cavity wall, δ is the depth of the cavity, r_s represents the distance from the midpoint of the cavity wall to the symmetry axis, and r_d controls to the slope of the cavity and the curvature of the corner.

In this work, we study the transfer ratio (mass fraction of liquid transferred to top plate) as a function of the capillary number Ca and electroviscous number χ (Table 4.2). For leaky dielectrics, the dimensionless conductivity K^* and initial surface charge density also come into play.

4.2.2 Solution method

Equations (4.1) – (4.18) are solved using the Galerkin finite-element method [54, 57, 63, 95] with elliptic mesh generation to track the moving interface. A first-order backward Euler method is applied in the first two time steps to prevent abrupt oscillations. A second-order trapezoid rule is then used to perform time integration [66].

When the liquid bridge nears breakup, a thin thread connecting a droplet on each solid surface is formed. Eventually, the elements in the thread become extremely deformed and elongated, causing the simulation to fail. At the end of the simulation, the narrowest bridge radius is roughly 0.1% of its initial radius. The overall bridge shape has primarily been determined at this point, so the transfer ratio will likely not vary

significantly even if the bridge stretches further. After a simulation ends, we check whether the variation from the initial bridge volume is less than 0.1% to ensure mass conservation. If the change of volume is greater than 0.1%, we rerun the simulation with a refined mesh or time step.

4.3 Results - Flat Plates

When a liquid bridge is stretched between two flat plates without an electric field, both theoretical and experimental results show that the transfer ratio (mass fraction of liquid transferred to top plate) is mainly determined by the wettability difference between the two plates at low Ca (< 0.01) [5, 54]. When Ca is large enough (~ 1), the transfer ratio is about 50% and independent of the wettability difference [6, 54]. In this section, we explore how electric fields influence liquid transfer when both plates are flat. The results presented here complement those obtained in our earlier work using a 1D slender-jet model [82].

The initial bridge shape is a cylinder with length $L(0)$ and radius R. Although the initial bridge shape can significantly influence liquid transfer [54], we use a cylinder here since initial-shape effects have been studied previously [54] and we would now like to isolate the influence of electric fields. For simplicity, we set $L(0) = 2R$ so that the aspect ratio is unity.

The top contact angle θ_{top} is set to 60°, while the bottom contact angle θ_{bottom} ranges from 40° to 80°. The wettability difference $\Delta\theta_r = \theta_{\text{bottom}} - \theta_{\text{top}}$, so positive $\Delta\theta_r$ means that the bottom plate is less wettable than the top plate. We fix the value of ϵ to the representative value of 2.74 (silicone oil); increasing this will tend to enhance the effect of electric fields. Two values of the capillary number Ca (0.1 and 0.5) are considered, and the electroviscous number χ is set to 0 (no electric field) or 40.

4.3.1 Perfect dielectric

Liquid transfer

We begin by examining transfer of a perfect dielectric liquid between two flat plates by setting $q = 0$ and $K^* = 0$. Figure 4.3(a) shows the relationship between the transfer ratio

and wettability difference $\Delta\theta_r$ at $Ca = 0.1$. When $\chi = 0$, the transfer ratio increases as $\Delta\theta_r$ increases. Because the bottom plate becomes less wettable as $\Delta\theta_r$ increases, more liquid is transferred to the top plate. When χ increases from 0 to 40, the transfer ratio increases when $\Delta\theta_r$ is positive. However, when $\Delta\theta_r$ is negative, the transfer ratio decreases when an electric field is present. These results indicate that electric fields enhance liquid transfer to the more wettable surface.

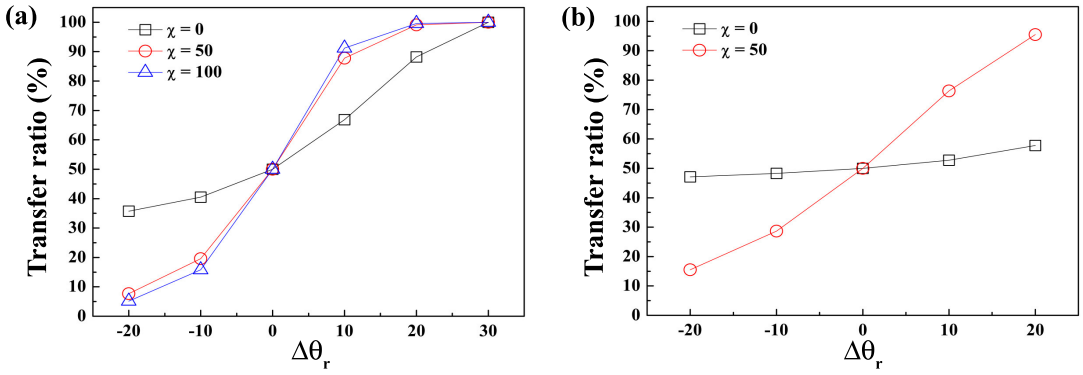

Figure 4.3: Relationship between transfer ratio and wettability difference for different values of χ at (a) $Ca = 0.1$ and (b) $Ca = 0.5$. Here, $\theta_{\text{top}} = 60°$, and θ_{bottom} varies from 40° to 80°. The wettability difference $\Delta\theta_r = \theta_{\text{bottom}} - \theta_{\text{top}}$.

Figure 4.3(b) presents the transfer ratio as a function of $\Delta\theta_r$ at $Ca = 0.5$. When $\chi = 0$, the transfer ratio also increases as $\Delta\theta_r$ increases. However, the transfer ratios are $50\% \pm 3\%$ for all values of $\Delta\theta_r$ since the viscous forces are stronger at higher Ca and reduce the influence of wettability differences. This represents a limit on how much liquid can be transferred at high printing speeds.

As can be seen in Fig. 4.3(b), the presence of the electric field enhances the influence of wettability differences when $Ca = 0.5$. This suggests that electric fields may be a useful tool for increasing liquid transfer at high printing speeds. Note that the electro-capillary number $Ca_E = \chi Ca$ provides a measure of the strength of electrostatic forces to surface-tension forces, and is smaller for fixed χ at smaller Ca. Thus, the electric field does not influence the transfer ratio as much at lower Ca (Fig. 4.3(a)) compared to higher Ca (Fig. 4.3(b)).

Results from the 1D slender-jet model used in our previous work [82] show qualitatively similar behavior. However, the 1D model predicts much more liquid transfer

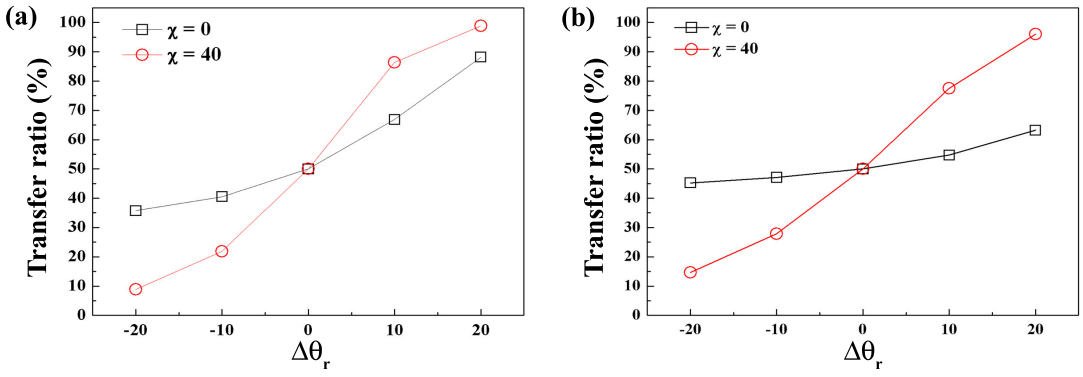

Figure 4.4: Relationship between transfer ratio and wettability difference predicted by the 1D slender-jet model for different values of χ at (a) $Ca = 0.1$ and (b) $Ca = 0.5$. Here, $\theta_{\text{top}} = 60°$, and θ_{bottom} varies from 40° to 80°. The wettability difference $\Delta\theta_r = \theta_{\text{bottom}} - \theta_{\text{top}}$.

compared to the 2D model. Figure 4.4 shows the relationship between the transfer ratio (mass fraction of liquid transferred to top plate) and wettability difference $\Delta\theta_r$ predicted by the 1D slender-jet model for $Ca = 0.1$ and $Ca = 0.5$ in the absence and presence of an electric field. The 1D model predicts a much larger change in liquid transfer compared to the 2D model.

For $Ca = 0.1$ and $\Delta\theta_r = 20°$, the 1D model predicts an increase in the transfer ratio of ∼10%, whereas the 2D model predicts an increase of only ∼4%. Similarly, for $Ca = 0.5$ and $\Delta\theta_r = 20°$, the 1D model predicts an increase of ∼33%, whereas the 2D model predicts an increase of only ∼4%.

The reason for the differences between the predictions of the 1D and 2D models can be understood from our earlier work in the absence of electric fields [54]. In contrast to the 2D model, the 1D model neglects radial pressure gradients, and the contact line moves in such a way as to satisfy the specified contact angle. As a result, the 1D model predicts more contact-line movement than the 2D model, and more transfer orretention of liquid relative to the 2D model. These differences can become especially pronounced at intermediate values of Ca, where viscous forces become just as important as wettability differences in determining liquid transfer.

We now consider the case where $\Delta\theta_r = 20°$ and $Ca = 0.5$ to characterize contact-line motion and bridge shapes. Figure 4.5(a) shows the time-evolution of contact-line

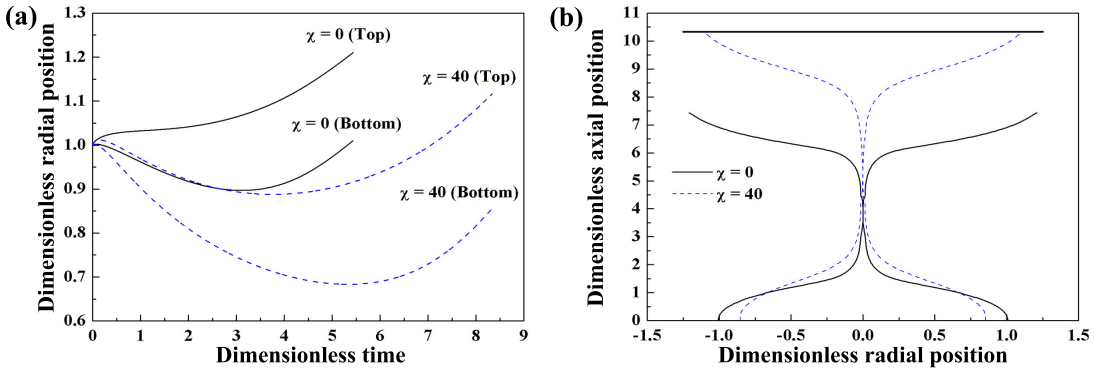

Figure 4.5: (a) Time-evolution of contact line on top and bottom plates for $\chi = 0$ (solid line) and 40 (dashed line). (b) Final bridge shapes for $\chi = 0$ (solid line) and 40 (dashed line). The bridge breakup times for $\chi = 0$ and 40 are 5.4 and 8.3, respectively. Values of other parameters are $Ca = 0.5$, $\theta_{\text{top}} = 60°, \theta_{\text{bottom}} = 80°$, and $\Delta\theta_r = 20°$.

positions. When $\chi = 0$, the top contact line simply expands in the radial direction, while the bottom contact line first retracts and then expands. However, when $\chi = 40$, both contact lines retract and then expand. Note that the bottom contact radius decreases faster than the top contact radius when $\chi = 40$ because the bottom surface is less wettable.

Figure 4.5(b) compares the final bridge shapes for $\chi = 0$ and 40. In Fig. 4.5(b), the difference between the top and bottom contact radii of the electrified bridge (0.26) is larger than that of the non-electrified bridge (0.20) when the simulation ends. In addition, the electrified bridge breaks up at a longer length. These results suggest that the electric field stabilizes the liquid bridge and amplifies the influence of wettability differences, a feature we will discuss further in section 4.3.1.

Figure 4.6(a) shows the time-evolution of contact-line positions predicted by the 1D model for the case where $\Delta\theta_r = 20°$ and $Ca = 0.5$. The bottom contact radius with and without the electric field first decreases and then increases. These results are qualitatively similar to those from the 2D model, as is the behavior of the contact line for the non-electrified bridge. However, the 1D model predicts that the top contact radius of the electrified bridge increases monotonically, whereas the 2D model predicts that the top contact radius of the electrified bridge first decreases and then increases.

Figure 4.6(b) shows the final bridge shapes predicted by the 1D model. The presence

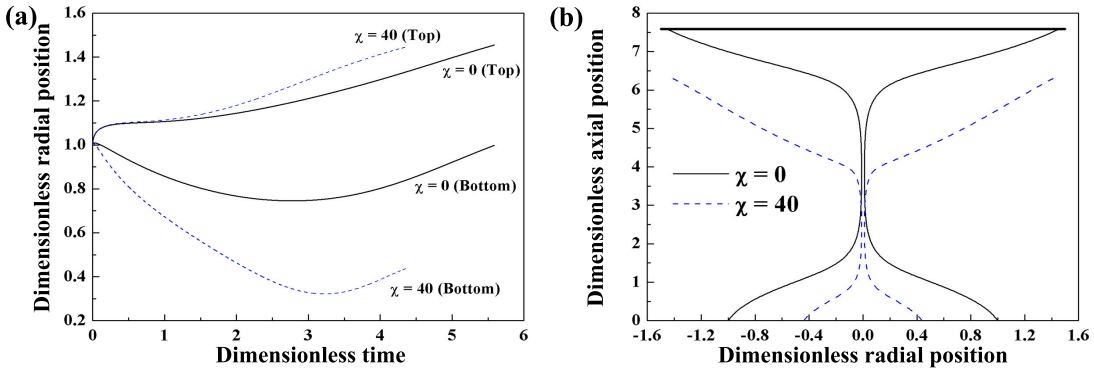

Figure 4.6: (a) Time-evolution of contact line on top and bottom plates for $\chi = 0$ (solid line) and 40 (dashed line). (b) Final bridge shapes for $\chi = 0$ (solid line) and 40 (dashed line). The breakup times for $\chi = 0$ and 40 are 5.6 and 4.4, respectively. Values of other parameters are $Ca = 0.5$, $\theta_{\text{top}} = 60°, \theta_{\text{bottom}} = 80°$, and $\Delta\theta_r = 20°$.

of the electric field significantly decreases the contact radius on the less wettable surface, which is consistent with the predictions of the 2D model (Fig. 4.5(a)). However, the 1D model predicts that the electrified bridge breaks up earlier than the non-electrified bridge, which is opposite to what the 2D model predicts.

As can be seen by comparing Fig. 4.5 with Fig. 4.6, the behavior of the bottom contact line predicted by the 1D and 2D models is qualitatively similar, as is the behavior of the top contact line in the absence of the electric field. However, the 1D model predicts that the top contact radius of the electrified bridge increases monotonically, while the 2D model predicts that the top contact radius of the electrified bridge first decreases and then increases. In addition, the 1D model predicts that the electrified bridge breaks up earlier than the non-electrified bridge, which is opposite to the prediction of the 2D model. The reasons for these differences will be discussed in section 4.3.1.

Physical mechanisms

For perfect dielectrics, the only way the electric field influences the liquid bridge is through the normal stress balance (Eq. (4.11)). It is instructive to examine this boundary condition in the slender-jet limit, as it yields an expression for the liquid pressure [82],

$$P = \frac{\kappa}{Ca} - v_z - \chi \frac{\epsilon - 1}{2} E^2, \tag{4.20}$$

where E is the leading-order axial component of the electric field. The three terms on the right-hand side of Eq. (4.20) represent contributions from surface tension, viscous, and electrostatic forces, respectively. Note that the pressure in Eq. (4.20) only depends on the axial coordinate due to the slender-jet approximation. Because χ is always positive and ϵ is greater than 1, the electrostatic term in Eq. (4.20) is always negative. As a result, the electrostatic term lowers the pressure in the bridge.

We now plot pressure contours and bridge shapes predicted by the 2D model for the case where $Ca = 0.5$ and $\Delta\theta_r = 20°$ to gain insight into the observations of section 4.3.1. The physical mechanisms we will discuss also hold at lower values of Ca. For convenience, we rotate the bridge 90° clockwise so the top/bottom surface is on the right/left in Fig. 4.7.

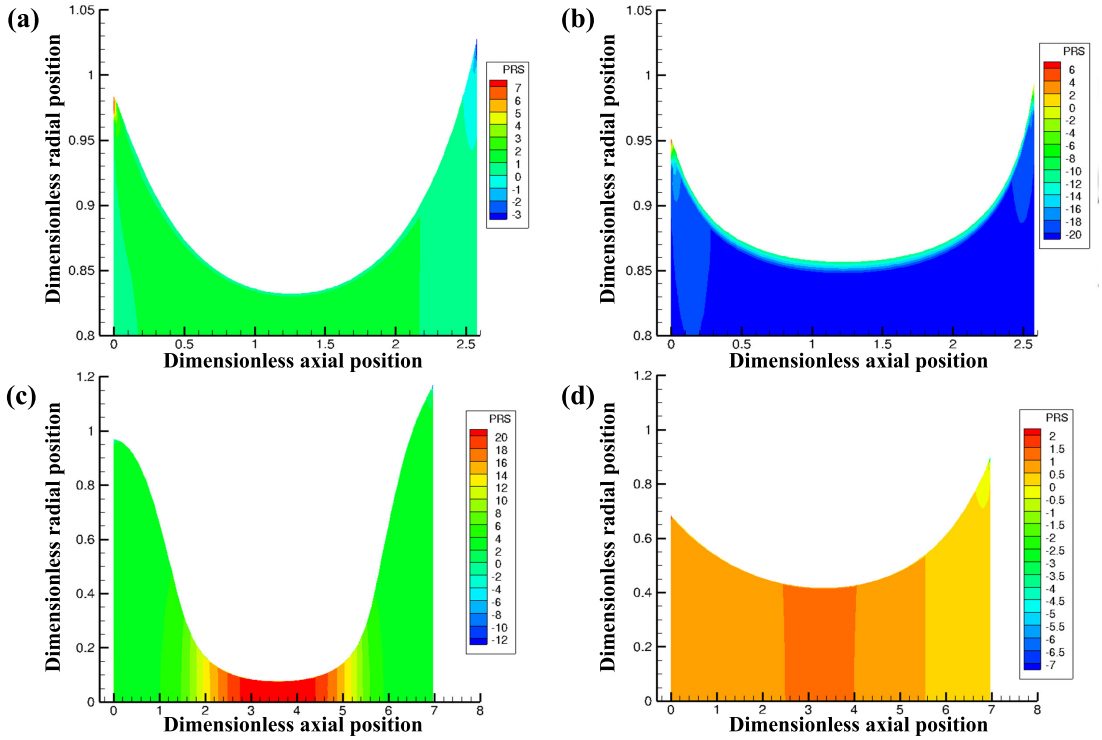

Figure 4.7: Pressure contours and bridge shapes for the cases where (a,c) $\chi = 0$ and (b,d) $\chi = 40$ at (a,b) $t = 0.6$ and (c,d) $t = 5$. The bridge breakup times for $\chi = 0$ and 40 are 5.4 and 8.3, respectively. Values of other parameters are $Ca = 0.5$, $\theta_{\text{top}} = 60°$, $\theta_{\text{bottom}} = 80°$, and $\Delta\theta_r = 20°$.

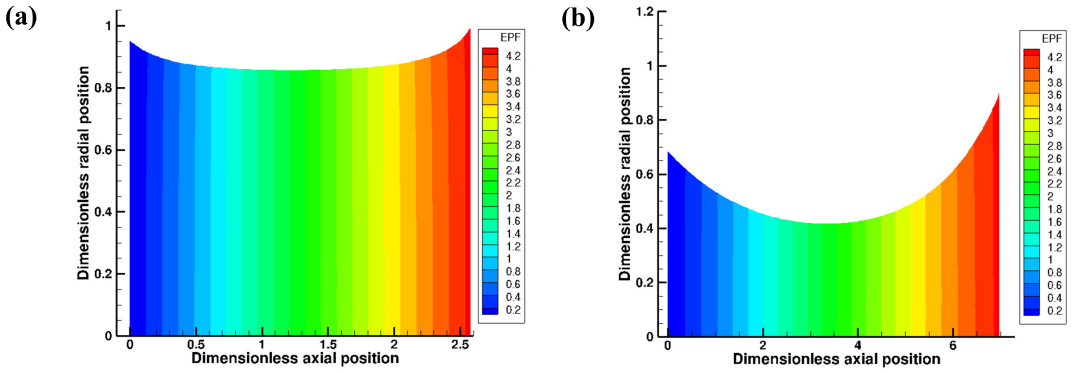

Figure 4.8: Electrostatic potential contours and bridge shapes for for the case where $\chi = 40$ at (a) $t = 0.6$ and (b) $t = 5$. Values of other parameters are $Ca = 0.5$, $\theta_{\text{top}} = 60°, \theta_{\text{bottom}} = 80°$, and $\Delta\theta_r = 20°$.

Figure 4.7(a) shows pressure contours when $\chi = 0$ at $t = 0.6$. The highest pressure is near the left (bottom) contact line, while the lowest pressure is near the right (top) contact line. Since liquid flows from regions of higher pressure to lower pressure, the bottom contact radius decreases while the top contact radius increases (Fig. 4.5(a)).

Figure 4.7(b) shows pressure contours when $\chi = 40$ at $t = 0.6$. The pressure near both contact lines is larger than the pressure near the bridge center. This can be understood by noting that the axial component of the electric field is stronger near the bridge center than near the contact lines, as can be seen by examining the electrostatic potential contours in Fig. 4.8(a). According to Eq. (4.7), the electric field will lower the pressure the most near the bridge center. The resulting pressure gradients cause both contact lines to retract. Because the left (bottom) surface is less wettable than the right (top) surface, the left contact line retracts faster than the right contact line (Fig. 4.5(a)). The lower pressure in the bridge center when the electric field is present also implies that the bridge is stabilized by the electric field and should stretch longer before breaking up.

Figure 4.7(c) shows pressure contours when $\chi = 0$ at $t = 5$. Because this is close to the breakup time of $t = 5.4$, the highest pressure is near the bridge center. The resulting pressure gradients push liquid away from the bridge center toward each plate. As a consequence, the contact radii increase near the end of stretching (Fig. 4.5(a)).

Figure 4.7(d) shows pressure contours when $\chi = 40$ at $t = 5$. The highest pressure is near the left (bottom) plate, while the lowest pressure is near the right (top) plate. There is also a local maximum in pressure near the bridge center. In addition, the radial component of the electric field becomes more pronounced (relative to the axial component) near the contact lines as can be seen by examining the electrostatic potential contours in Fig. 4.8(b). Since the electrostatic potential at the top plate is a constant, the influence of electrostatic forces becomes weaker during stretching, and eventually ($t \sim 6$) the region of highest pressure occurs near the bridge center (results not shown). As a consequence, both contact lines expand in the radial direction (Fig. 4.5(a)). Because the electric field delays bridge breakup, the contact line on the less wettable surface has more time to retract on that surface. As a result, more liquid is transferred to the more wettable surface when the electric field is present.

We now discuss the reason for the different motion of the top contact line predicted by the 1D and 2D models when the electric field is present. Comparison of Figs. 4.7(a) and 4.7(b) shows that the electric field significantly modifies the pressure distribution in the bridge. Fig. 4.7(b) shows that there is a strong radial pressure gradient near the right (top) contact line, which is what causes the contact line to retract initially (Fig. 4.5(a)). However, the 1D model neglects pressure gradients in the radial direction [54], and as a result, the 1D model predicts that the top contact line expands at early times when the electric field is present (see Fig. 4.6(a) of Supplemental Material). At later times, the axial pressure gradient dominates, and so the contact-line motion predicted by both models is consistent at later times (compare Fig. 4.5(a) and Fig. 4.6(a) of Supplemental Material).

In contrast to the 1D model, the 2D model predicts that the electrified bridge can be stretched longer than the non-electrified bridge before breakup occurs (Fig. 4.5(b)). Recall from Fig. 4.7 that the electric field lowers the pressure near the bridge center. This allows the bridge to stretch for a longer time before breaking up, and as a consequence, allows more time for the contact line to retract on the less wettable surface (Fig. 4.5(a)). But as noted in section 4.3.1, the 1D model tends to predict more contact-line movement than the 2D model due to its neglect of radial pressure gradients. We believe that this simplification, along with the modification of the pressure distribution in the bridge by the electric field, causes the 1D model to predict that the electrified

bridge breaks earlier than the non-electrified bridge. Notably, the breakup times for the non-electrified bridge predicted by the 1D and 2D models are comparable ($t = 5.6$ vs. $t = 5.4$), but the breakup time for the electrified bridge predicted by the 1D model is much faster than what is predicted by the 2D model ($t = 4.4$ vs. $t = 8.3$) (Fig. 4.5 and Fig. 4.6 of Supplemental Material).

4.3.2 Leaky dielectric

We now consider leaky dielectrics where the surface charge density q and liquid conductivity K^* may be non-zero.

Electrostatic contribution to the tangential stress

For leaky dielectrics, the electric field still makes a contribution to the normal stress balance. However, a non-zero surface charge density and an electric field can also influence the tangential stress balance, as seen in Eq. (4.12). As discussed in Ref. [82] in the context of the 1D model, the transfer ratio can be increased by manipulating the direction of the electrostatic contribution to the tangential stress. The magnitude of this stress is determined by the surface charge density q and the tangential component of the electric field along the interface. The direction of this stress depends on the sign of q and the direction of the electric field since $\chi > 0$.

To enhance liquid transfer to the top plate, the electrostatic contribution to the tangential stress has to be positive so that it points to the positive z-direction. Since the sign of the surface charge may depend on material properties, the direction of the electric field can be adjusted to manipulate the direction of the tangential stress. If the surface charge is positive, then the direction of the electric field should point in the positive z-direction by applying a positive potential on the bottom plate while grounding the top plate (and vice versa; note that $\mathbf{E}_i = -\nabla\phi_i$).

Liquid transfer

We set the initial surface charge density q_o to 0 or 0.5. The latter value of charge density corresponds to 4.4×10^{-6} C/m^2 for a 1 kV potential difference over a 1 mm gap. This initial surface charge density is about two orders of magnitude smaller than

the values used in studies of electrospinning [43], but is large enough to significantly influence bridge behavior. In this section, a constant electrostatic potential is applied at the bottom plate while the top plate is grounded. Therefore, the direction of the electrostatic contribution to the tangential stress is in the positive z-direction.

The second term on the right-hand side of Eq. (4.5) represents a change in surface charge density due to charge accumulation at the liquid-air interface [33]. We set the dimensionless conductivity K^* to 0 or 1. The latter value corresponds to 8.8×10^{-12} $(\Omega$ m$)^{-1}$ for a 1 mm characteristic length and 1 mm/sec stretching speed. This conductivity is of the same order of magnitude of what is observed for silicon oil. If K^* is even smaller, not enough surface charge accumulates to significantly influence the bridge shape before the simulation ends.

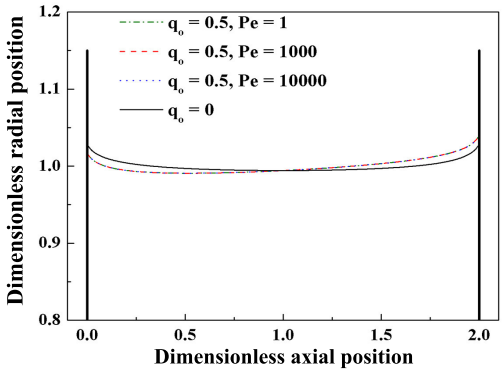

Figure 4.9: Comparison equilibrium bridge shapes for different Pe. Here, $\theta_{\text{top}} = \theta_{\text{bottom}} = 60°$, $\Delta\theta_r = 0°$, and $Ca_E = 40$.

The diffusion term in Eq. (4.5) is usually neglected [33], but we keep this term to prevent steep charge gradients that form near each contact line [44]. To determine the value of Pe to use in our simulations, we examine equilibrium bridge shapes. When the bridge reaches its equilibrium shape, the surface charge density should be uniform. To obtain an equilibrium shape, we start with a cylinder having an initial aspect ratio of 1 and set the velocity of both plates to zero until an equilibrium shape is reached. Both the top and bottom contact angles are set at 60° to remove the influence of the wettability differences. Because the velocity of both surfaces is zero, we use a velocity scale of γ/μ and time scale of $R\mu/\gamma$. The electrocapillary number $Ca_E = R\epsilon_o E^2/\gamma$ represents the ratio of electrostatic to surface-tension forces.

Figure 4.9 shows equilibrium bridge shapes for different values of Pe at $Ca_E = 40$. When no initial surface charge is present, the bridge is symmetric due to zero wettability difference. However, when $q_o = 0.5$, the equilibrium shapes are asymmetric but very similar to each other for $Pe = 1 \sim 10^4$. These calculations indicate that the equilibrium bridge shapes for $Pe \sim 1$ to 10^4 are very similar, so we choose a value of $Pe = 1000$ since it provides a reasonable balance between computational accuracy and cost.

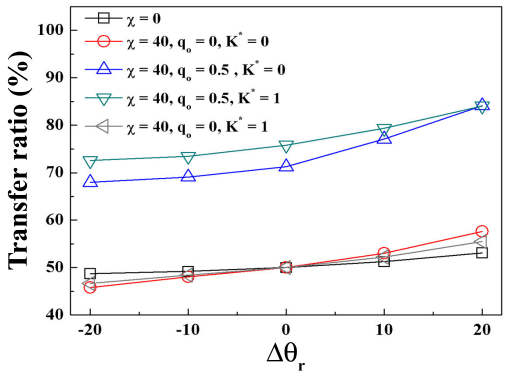

Figure 4.10: Transfer ratio vs. wettability difference for cases where $\chi = 0$ ($\square$), $\chi = 40$, $q_o = 0$, $K^* = 0$ ($\bigcirc$), $\chi = 40$, $q_o = 0.5$, $K^* = 0$ ($\triangle$), $\chi = 40$, $q_o = 0.5$, $K^* = 1$ ($\bigtriangledown$), and $\chi = 40$, $q_o = 0$, $K^* = 1$ ($\triangleleft$). Here, $\theta_{\text{top}} = 60°$, and θ_{bottom} varies from 40° to 80°. Values of other parameters are $Ca = 0.5$ and $Pe = 1000$.

To understand how the initial surface charge density and conductivity influence liquid transfer, we consider four different cases: (i) $q_o = 0$, $K^* = 0$ (perfect dielectric) (ii) $q_o = 0.5$, $K^* = 0$, (iii) $q_o = 0$, $K^* = 1$, and (iv) $q_o = 0.5$, $K^* = 1$. Figure 4.10 shows the transfer ratio for these cases at $Ca = 0.5$, as well as the transfer ratio for the non-electrified bridge.

In Fig. 4.10, the values of the transfer ratio for the case where $q_o = 0$ and $K^* = 1$ are in between the values for the perfect dielectric bridge and the non-electrified bridge. However, for the case where $q_o = 0.5$, and $K^* = 0$, the transfer ratio increases about 20% compared to the transfer ratio for the perfect dielectric bridge for all values of $\Delta\theta_r$. Additionally, the transfer ratio for the case where $q_o = 0.5$ and $K^* = 1$ is only about 1% to 5% higher than that for the case where $q_o = 0.5$ and $K^* = 0$.

These results indicate that tangential stresses arising from surface charge can significantly enhance liquid transfer even when the top plate is less wettable than the bottom

plate. In addition, they show that the initial surface charge plays a more important role than liquid conductivity in controlling liquid transfer. The predictions of the 2D model are in qualitative agreement with those from the 1D model [82], although the 1D model predicts a higher transfer ratio due to the approximations it makes (section 4.3.1).

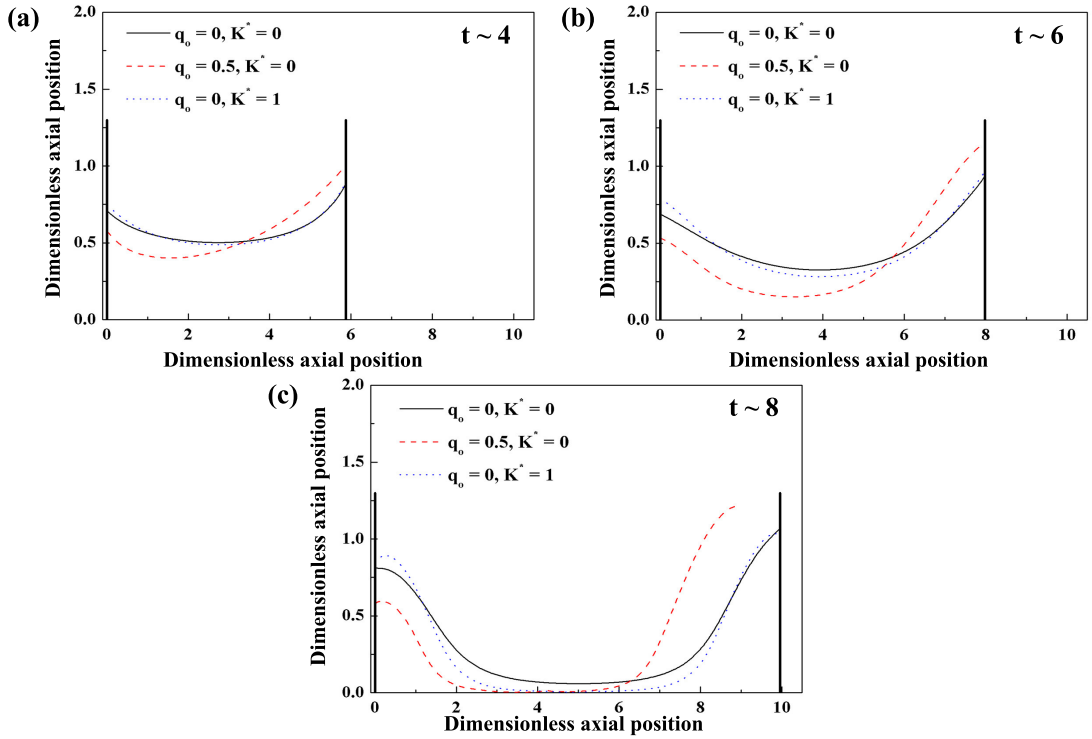

Figure 4.11: Bridge shapes at times (a) $t = 4$, (b) $t = 6$, and (c) $t = 8$. The breakup times for the cases with $q_o = 0$, $K^* = 0$ (solid line), $q_o = 0.5$, $K^* = 0$ (dashed line), and $q_o = 0$, $K^* = 1$ (dotted line) are 8.3, 6.9, and 8.0, respectively. Values of other parameters are $Ca = 0.5$, $\chi = 40$, $\theta_{\text{top}} = 60°$, $\theta_{\text{bottom}} = 80°$, and $\Delta\theta_r = 20°$.

We now examine bridge shapes at different times to explain why the initial surface charge plays a more important role than conductivity in controlling liquid transfer. Figure 4.11 shows bridge shapes at several different times. In Fig. 4.11(a), liquid is pushed to the right (top) plate for the case where $q_o = 0.5$ and $K^* = 0$, whereas the bridge shapes for the other two cases nearly overlap. As shown in Eq. (4.12), the electrostatic contribution to the tangential stress is the product of the surface charge and the tangential component of the electric field. Therefore, when the initial surface charge

is non-zero, the tangential stress pushes liquid at the beginning of bridge stretching. However, for the case where $q_o = 0$ and $K^* = 1$, it takes time for charge to accumulate at the liquid-air interface. As a consequence, the tangential stress is not strong enough to significantly influence bridge shape.

At later time $t = 6$ (Fig. 4.11(b)), the bridge for the case where $q_o = 0.5$ and $K^* = 0$ is close to breakup. In addition, the bridge for the case where $q_o = 0$ and $K^* = 1$ becomes narrower than the bridge for the case where $q_o = 0$ and $K^* = 0$ due to the presence of tangential stresses. We find that negative surface charge accumulates on the left (bottom) half of the bridge because the left plate is the positive electrode, and vice versa. As a consequence, the tangential stress near the left plate points in the negative z-direction while the tangential stress near the right plate points in the positive z-direction. This drives liquid to each plate and results in a narrower bridge and a slightly lower transfer ratio (Fig. 4.10).

Final bridge shapes are shown in Fig. 4.11(c). The bridge with $q_o = 0.5$ breaks earlier ($t = 6.9$) than the bridges with $q_o = 0$ ($t = 8.0$ for $K^* = 1$ and $t = 8.3$ for $K^* = 0$). These results show that the initial surface charge not only enhances liquid transfer but also reduces the breakup time. However, the breakup time for the bridge with $q_o = 0.5$ is still longer than that for a corresponding non-electrified bridge (Fig. 4.5(b)) because of the stabilizing effect of the electric field. If the initial surface charge is zero, the surface charge does not accumulate fast enough for tangential stresses to significantly modify liquid transfer. If the initial surface charge and conductivity are non-zero, the accumulated surface charge can increase the strength of the tangential stress, and the transfer ratio can be further increased (Fig. 4.10).

4.4 Results - Cavity

In section 4.3, we observed that application of an electric field stabilizes a stretching liquid bridge, which allows more time for the contact line to recede on the less wettable surface and leads to an increase in liquid transfer to the more wettable surface. Tangential stresses due to surface charge can significantly enhance liquid transfer, even to the less wettable surface. Predictions from the 2D model are in qualitative agreement with those of the 1D model presented in our prior work [82]. In this section, we replace

the bottom plate with a cavity (Fig. 4.2(b)) to study how electric fields influence liquid transfer. Because the cavity has a geometry that varies in the radial direction, the 1D model cannot be applied and 2D calculations are necessary.

In our study, the parameters in Eq. (4.19) are the depth of cavity $\delta = 1$, distance from the symmetry axis to the midpoint of the cavity wall $r_s = 0.8$, and curvature of the corner $r_d = 0.3$; the values chosen are consistent with those used in our previous studies [57, 63]. The initial distance between the flat plate and the cavity bottom is 1.2, and consistent with our previous studies [57, 63], we begin with a liquid bridge that has a vertical liquid-air interface located 1.05 units away from the symmetry axis. Before stretching the bridge, we run simulations without an electric field with $U = 0$ until the bridge reaches an equilibrium shape. This equilibrium shape is then used as an initial condition when stretching the bridge, both in the absence and presence of an electric field.

4.4.1 Perfect dielectric

Effects of electrostatic forces

We begin by examining liquid transfer for perfect dielectrics. The top contact angle θ_{top} is fixed at 70°, while the bottom contact angle θ_{bottom} varies from 50° to 90°. The relative permittivity of the liquid phase is again set to $\epsilon = 2.74$.

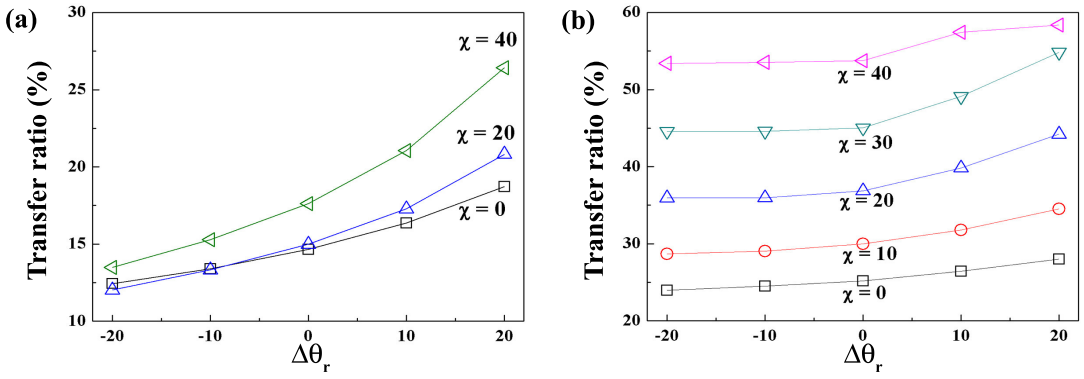

Figure 4.12: Relationship between transfer ratio and wettability difference for different values of χ at (a) $Ca = 0.1$ and (b) $Ca = 0.5$. Here, $\theta_{\text{top}} = 70°$, and θ_{bottom} varies from 50° to 90°. The wettability difference $\Delta\theta_r = \theta_{\text{bottom}} - \theta_{\text{top}}$.

Figure 4.12 shows how the transfer ratio varies as function of wettability difference in the absence and presence of an electric field at $Ca = 0.1$ and 0.5. In Fig. 4.12(a), where $Ca = 0.1$, the transfer ratio increases as $\Delta\theta_r$ increases when $\chi = 0$. However, the values of the transfer ratio are much less than those for liquid transfer between two flat plates (Fig. 4.3). Because the contact line tends to pin on the cavity wall and retract on the flat plate, the resulting droplet that forms on the flat plate is much smaller than that in the cavity [57]. When $\chi = 20$, the transfer ratio increases as $\Delta\theta_r$ increases but does not change much when $\Delta\theta_r < 0°$. However, when χ is further increased to 40, the values of the transfer ratio are larger for all $\Delta\theta_r$ compared to the values when the electric field is absent. The transfer ratio also becomes larger as $\Delta\theta_r$ increases. These results show that if electrostatic forces are strong enough, they can increase liquid transfer from a cavity even when $\Delta\theta_r < 0$.

Comparison of Figs. 4.12(a) and 4.12(b) shows that when no electric field is present, the transfer ratio increases as Ca increases from 0.1 to 0.5. Because the viscous forces are stronger at higher Ca, they are more effective at reducing the tendency of the contact-line to retract on the flat plate, and as a result, more liquid is transferred there [57]. As can be seen in Fig. 4.12(b), the transfer ratio increases as χ increases for all $\Delta\theta_r$; the physical mechanisms responsible for this will be discussed below. As noted in section 4.3.1, the influence of the electric field is more prominent at larger Ca since χCa is larger.

We now characterize how the electric field changes contact-line movement and thus the transfer ratio. Figure 4.13(a) shows the time-evolution of contact-line positions for $\chi = 0$ and 40 at $Ca = 0.5$ and $\Delta\theta_r = 20°$. In Fig. 4.13(a), both contact lines slip down each surface at the beginning of stretching for $\chi = 0$. However, the top contact line keeps retracting until bridge breakup, while the bottom contact line effectively pins on the cavity wall [57]. Even though the top plate is more wettable than the cavity, the top contact radius becomes smaller than the bottom contact radius. Therefore, the transfer ratio is only 28% (Fig. 4.12(b)). For $\chi = 40$ (Fig. 4.13(a)), the bottom contact line slips faster than the top contact line. The faster retraction of the bottom contact line down the cavity wall when the electric field is present allows more liquid near the cavity to transfer to the flat plate.

Figure 4.13(b) shows the final bridge shapes for $\chi = 0$ and 40. In Fig. 4.13(b), the

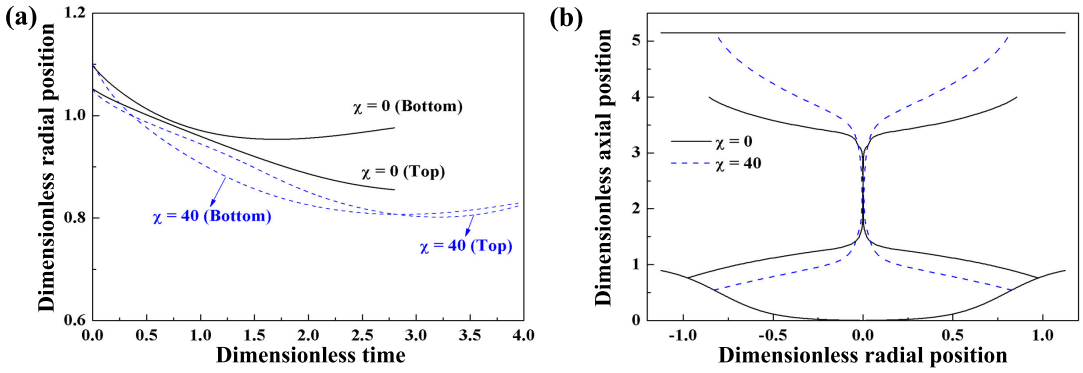

Figure 4.13: (a) Time-evolution of contact-line on top (flat plate) and bottom (cavity) surfaces for $\chi = 0$ (solid line) and 40 (dashed line). (b) Final bridge shapes for $\chi = 0$ (solid line) and 40 (dashed line). The bridge breakup times for $\chi = 0$ and 40 are 2.8 and 3.9, respectively. Values of other parameters are $Ca = 0.5$, $\theta_{\text{top}} = 70°$, $\theta_{\text{bottom}} = 90°$, and $\Delta\theta_r = 20°$.

size of the droplet in the cavity for $\chi = 40$ is smaller than that for $\chi = 0$. Even though the value of the top contact radius for $\chi = 40$ is slightly smaller than that for $\chi = 0$ (Fig. 4.13(a)), the size of the top droplet for the electrified bridge is larger than that for the non-electrified bridge (Fig. 4.13(b)). These results show that the electric field enhances liquid transfer by increasing contact line slippage on the cavity wall, thus pushing more liquid to the top plate. Note that the electrified bridge breaks up at a longer length than the non-electrified bridge because the electric field stabilizes the bridge as discussed in section 4.3.1.

To understand how the electric field promotes contact-line movement on the cavity wall, it is useful to analyze pressure contours near the contact lines as shown in Fig. 4.14. Figures 4.14(a) and 4.14(b) show pressure contours for $\chi = 0$ at $t = 0.4$. At the right (top) surface (Fig. 4.14(b)), the highest pressure is near the contact line, and the pressure decreases away from the contact line. Such a pressure gradient drives liquid away from the contact line, causing it to retract. At the left (bottom) contact line (Fig. 4.14(a)), the pressure gradient is smaller than that near the right (top) contact line. As discussed in Ref. [57], the interface near the cavity wall does not have to deform as much to maintain a constant contact angle due to the inclination of the cavity wall. As a consequence, the capillary pressure gradients there are smaller compared to those

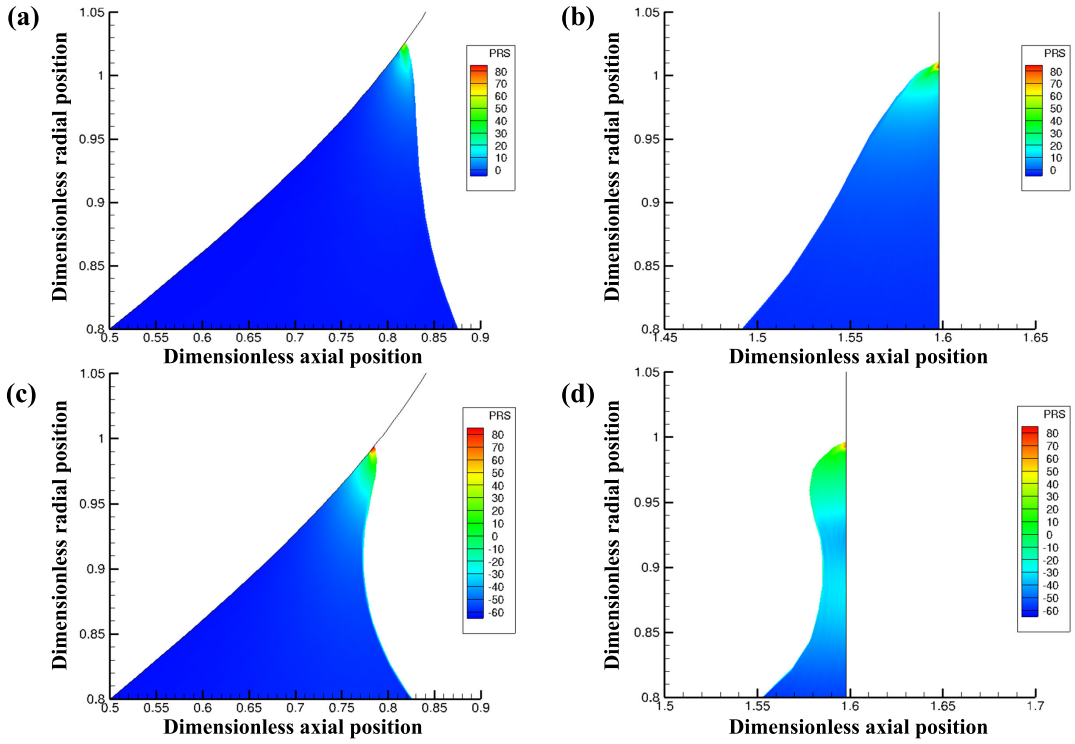

Figure 4.14: Pressure contours and interface shapes for (a,b) $\chi = 0$ and (c,d) $\chi = 40$ at $t = 0.4$. Panels (a) and (c) show the region near the contact line on the cavity wall, and panels (b) and (d) show the region near the flat plate. Values of other parameters are $Ca = 0.5$, $\theta_{\text{top}} = 70°, \theta_{\text{bottom}} = 90°$, and $\Delta\theta_r = 20°$.

near the contact line on the flat plate and the contact line effectively pins on the cavity wall (Fig. 4.13).

Figures 4.14(c) and 4.14(d) show pressure contours for $\chi = 40$ at $t = 0.4$. As discussed in section 4.3.1, the presence of the electric field decreases the pressure near the bridge center. Figures 4.14(c) and 4.14(d) show that the lowest pressure for the electrified bridge is much smaller than that for the non-electrified bridge (Fig. 4.14(a) and 4.14(b)). As a result, there is a higher pressure gradient near the contact line on the right (top) surface (Fig. 4.14(d)) compared to the case where $\chi = 0$ (Fig. 4.14(b)). The higher pressure gradient drives more liquid away from the contact line, leading to a large change in interface shape. In particular, a thin film of liquid forms on the top plate.

At the left (bottom) surface, the maximum pressure near the contact line is increased when the electric field is present (Fig. 4.14(c) and Fig. 4.14(a)). This, along with a lower pressure near the bridge center, leads to a higher pressure gradient near the contact line on the cavity wall, causing it to slip more. This overcomes the apparent pinning that was observed in the absence of the electric field (Fig. 4.13), and allows more liquid to be transferred to the top plate. We also observe that the interface is more highly curved near the cavity wall and begins to form a thin film when the electric field is present. Although the contact line on the top plate retracts more when the electric field is present, the increased slippage of the contact line on the cavity wall outweighs this effect and leads to an increase in the transfer ratio.

Effects of cavity depth

In this section, we report results from a brief parametric study examining the influence of cavity depth on liquid transfer. Here, the depth of cavity $\delta = 0.5$, which is one-half the value used in the previous section; the rest of the parameters in Eq. (4.19) remain the same. Figure 4.15(a) shows the two cavity shapes. Because we use a hyperbolic tangent function to define cavity shape, the angle between the cavity bottom and cavity wall increases about 7° when δ decreases from 1 to 0.5. The depth is decreased by 50% while the angle is changed only about 6%, so any change in the transfer ratio is likely mainly due to the change in cavity depth. The initial distance between the flat plate and the cavity for the shallower cavity is taken to be 0.6; this is half the value used in

the previous section and was chosen since the cavity depth has been halved.

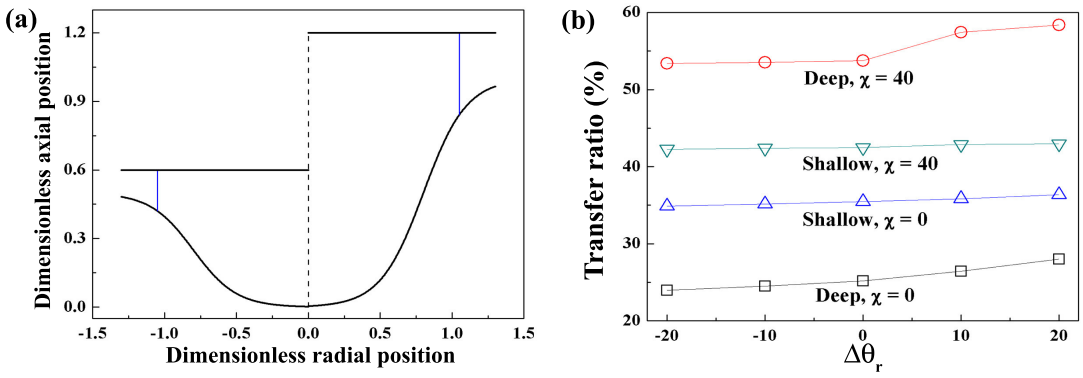

Figure 4.15: (a) Cavity shapes for $\delta = 1$ (right) and 0.5 (left). (b) Relationship between transfer ratio and wettability difference for different values of χ and cavity depths at $Ca = 0.5$. Here, $\theta_{\text{top}} = 70°$, and θ_{bottom} varies from 50° to 90°.

Figure 4.15(b) shows the transfer ratio for the two cavity depths at $Ca = 0.5$. When $\chi = 0$, the transfer ratio for the shallow cavity is higher than that for the deep cavity because the contact line on the shallow cavity slips more (results not shown). This result can be rationalized by noting that the cavity becomes a flat plate when δ approaches 0. Note that the transfer ratio for the geometry having two flat plates with $\Delta\theta_r = 20°$ and $Ca = 0.5$ is approximately 50%. Therefore, the transfer ratio increases as the cavity becomes shallower.

When $\chi = 40$, the transfer ratio increases relative to the $\chi = 0$ case for both the deep and shallow cavities for all wettability differences. Notably, the transfer ratio for the deep cavity increases about 30% while the transfer ratio for the shallow cavity only increases about 8%. Thus, the deep cavity eventually transfers more liquid to the top plate than the shallow cavity when the electric field is applied, which is the opposite to what is observed when the electric field is absent.

We now discuss the reason why the deep cavity transfers more liquid than the shallow cavity when the electric field is present. Figure 4.16 shows pressure contours for the shallow and deep cavity at $t = 0.4$. For the shallow cavity (Fig. 4.16(a)), the dimensionless pressure difference between the vicinity of cavity wall and bulk is about 75. For the deep cavity (Fig. 4.16(b)), the dimensionless pressure difference is about 150. This higher pressure difference arises from the change in curvature near the

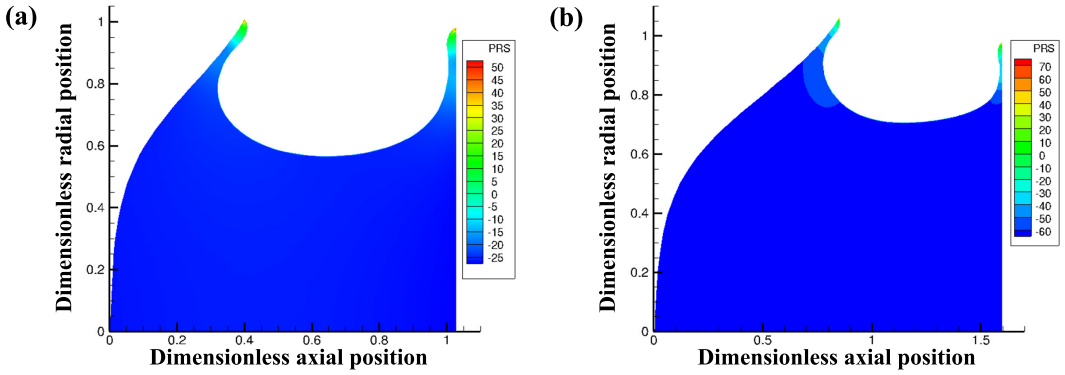

Figure 4.16: Pressure contours and interface shapes for the (a) shallow cavity and (b) deep cavity at $t = 0.4$. Values of other parameters are $Ca = 0.5$, $\chi = 40$, $\theta_{\text{top}} = 70^\circ, \theta_{\text{bottom}} = 90^\circ$, and $\Delta\theta_r = 20^\circ$.

contact line at the cavity wall. For the shallow cavity, the curvature near the contact line does not need to vary as much to maintain a contact angle. Therefore, the pressure difference in the shallow cavity is smaller than that of the deep cavity. At the later times (results not shown), the curvature of the interface in the shallow cavity becomes nearly constant, which causes the contact line to effectively pin. However, the interface of the deep cavity remains highly curved until the end of the stretching. Consequently, for the deep cavity, the capillary pressure gradient pumps liquid away from the cavity wall, causing the transfer ratio to increase.

In summary, by modifying the pressure distribution in the liquid bridge, the electric field also modifies the interface shapes and pressure gradients near the contact lines. This modification is more pronounced for the deep cavity, and results in a larger transfer ratio compared to the shallow cavity.

4.4.2 Leaky dielectric

In section 4.3.2, we found that tangential stresses due to surface charge have a significant influence on liquid transfer when both plates are flat. We now study the impact of the initial surface charge and conductivity on liquid transfer when the bottom plate is replaced by a cavity. We consider the cases where (i) $q_o = 0$, $K^* = 0$ (perfect dielectric), (ii) $q_o = 0.5$, $K^* = 0$, (iii) $q_o = 0$, $K^* = 1$, and (iv) $q_o = 0.5$, $K^* = 1$. The initial shapes and contact angles are the same as those used in section 4.4.1. The electroviscous

number $\chi = 40$, and the capillary number $Ca = 0.5$. As in section 4.3.2, a constant electrostatic potential is applied at the bottom plate while the top plate is grounded so that the electrostatic contribution to the tangential stress tends to point in the positive z-direction.

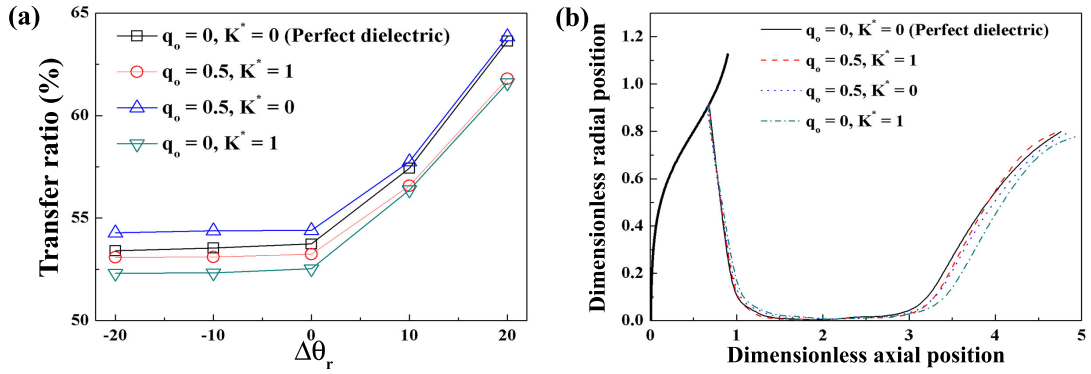

Figure 4.17: (a) Relationship between transfer ratio and wettability difference when (i) $q_o = 0$, $K^* = 0$ (□), (ii) $q_o = 0.5$, $K^* = 0$ (△), (iii) $q_o = 0$, $K^* = 1$ (▽), and (iv) $q_o = 0.5$, $K^* = 1$ (◯). Here, $\theta_{\text{top}} = 70°$, and θ_{bottom} varies from 50° to 90°. (b) Final bridge shapes for different cases when $\theta_{\text{top}} = \theta_{\text{bottom}} = 70°$ The bridge breakup times for cases (i)-(iv) are 3.56, 3.64, 3.73, and 3.55, respectively. Values of other parameters are $Ca = 0.5$ and $\chi = 40$.

Figure 4.17(a) shows the transfer ratio for perfect dielectrics ($q_o = 0$, $K^* = 0$) and leaky dielectrics at $Ca = 0.5$ and $\chi = 40$. The values of transfer ratio for the leaky dielectric cases are about 2% higher or lower than those for the perfect dielectric.

Figure 4.17(b) shows the final bridge shapes for these four cases when $\theta_{\text{top}} = \theta_{\text{bottom}} = 70°$. The final shapes almost overlap except for the region near the right (top) plate, and the bridge breakup times are all within 5% of the prefect-dielectric value. In contrast to the case where both surfaces are flat (Fig. 4.11), the electrostatic contribution to the tangential stress does not appear to significantly influence the movement of the contact line on the left (bottom) surface. In addition, the behavior of the transfer ratio and breakup times with respect to q_0 and K^* is less systematic than what is observed for liquid transfer between two flat plates (Fig. 4.10). These results indicate that the electrostatic contribution to the tangential stress has a much smaller effect on liquid transfer when the bottom plate replaced by a cavity. We have performed some additional calculations with $q_o = 1$ and 5 (results not shown), but the increase in

transfer ratio is still less than 5%.

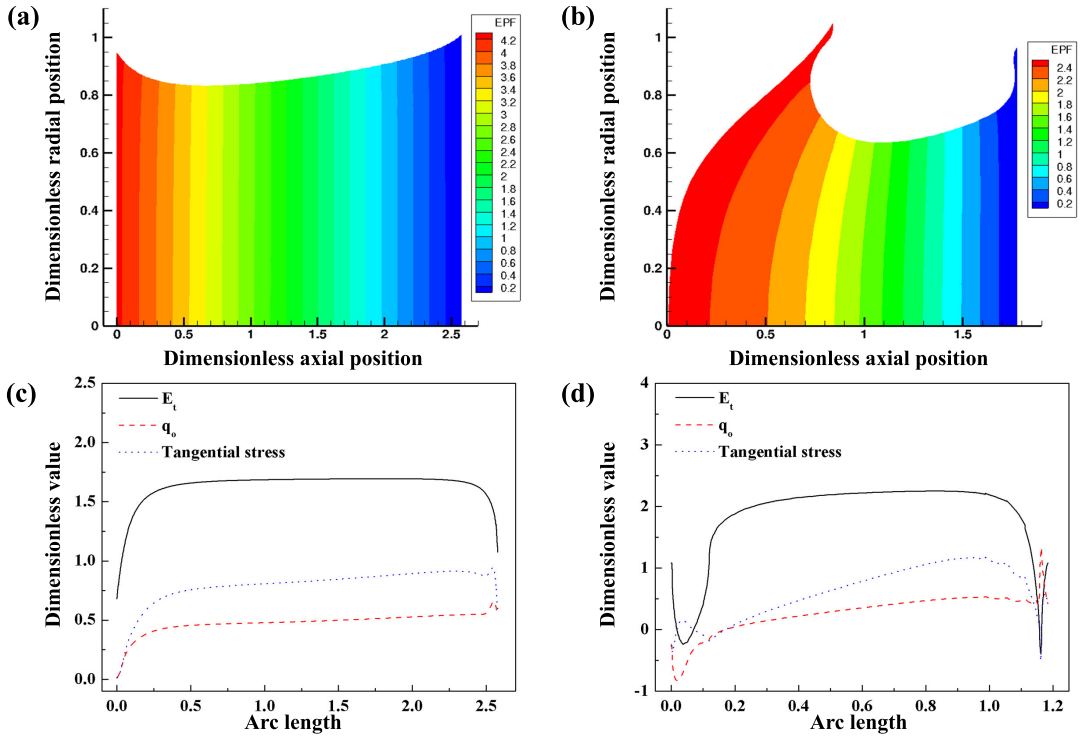

Figure 4.18: (a,b) Electrostatic potential contours and (c,d) electrostatic contribution to the tangential stress for liquid transfer between (a,c) flat plates and (b,d) a flat plate and a cavity at $t = 0.6$. Values of other parameters are $Ca = 0.5$, $\chi = 40$, $\theta_{\text{top}} = \theta_{\text{bottom}} = 70°$, $q_o = 0.5$, and $K^* = 1$.

From Eq. (4.12), the magnitude of the tangential stress is determined by the tangential component of the electric field and the surface charge density. To gain some insight into the results shown in Fig. 4.17, we compare the electrostatic potential for liquid transfer between two flat plates and liquid transfer between a flat plate and a cavity. We choose the case where $q_o = 0.5$ and $K^* = 1$, and to exclude the influence of wettability differences, set $\theta_{\text{top}} = \theta_{\text{bottom}} = 70°$.

Figure 4.18(a) shows the electrostatic potential contours for the case with two flat plates at $t = 0.6$. Figure 4.18(c) shows the corresponding tangential component of the electric field, surface charge, and electrostatic contribution to the tangential stress as a function of the arc-length coordinate along the interface. Since $\mathbf{E} = -\nabla\psi$, the direction

of the electric field is from left to right. In Fig. 4.18(a), the bridge interface is nearly parallel to the electric field. In addition, because the slope of the interface near each contact line is higher than that near the center of the bridge, the tangential component of the electric field near the center is greater than that near each contact line (Fig. 4.18(c)). As can be seen in Fig. 4.18(c), the surface charge is still uniformly distributed except near each contact line. The surface charge is approximately zero near the left surface, and it is positive near the right surface because the flow of liquid at the interface is from the left to right. As a result, the tangential stress pushes liquid to the right surface and enhances liquid transfer.

Figure 4.18(b) shows the electrostatic potential contours for the case with the cavity at $t = 0.6$. Figure 4.18(d) shows the corresponding tangential component of the electric field, surface charge, and electrostatic contribution of the tangential stress along the interface. In Fig. 4.18(b), the interface near each contact line is highly curved and nearly perpendicular to the direction of the electric field (positive z-direction). Therefore, as can be seen in Fig. 4.18(d), the tangential component of the electric field varies considerably near each contact line and is close to zero in some places. Near the center of the bridge, the tangential component of the electric field is relatively uniform. The surface charge is negative near the left contact line, and increases to positive values as the right contact line approached. The resulting tangential stresses over much of bridge length are positive, but near each contact line are close to zero and even negative. The positive tangential stresses tend to drive liquid to the right. However, the near-zero and negative tangential stresses near the contact lines lead to little additional contact line movement. Moreover, the thin films of liquid that form near each contact line provide additional viscous resistance to the tangential stresses. These factors may account for the less systematic behavior of the behavior of the transfer ratio and breakup times with respect to q_0 and K^* (Fig. 4.17).

4.5 Conclusions

Motivated by the use of electrostatic assist to improve liquid transfer in printing processes, we have examined the influence of electric fields on liquid transfer in two model

geometries, both of which involve liquid bridges with moving contact lines. For liquid transfer between two flat plates, application of an electric field stabilizes the liquid bridge. This allows more time for the contact line to retract on the less wettable surface and leads to an increase in liquid transfer to the more wettable surface. Tangential stresses due to surface charge can significantly enhance liquid transfer, even to the less wettable surface if the tangential stresses point toward that surface. The initial surface charge plays a more important role than liquid conductivity in enhancing liquid transfer. Predictions from the 2D model used in this work are in qualitative agreement with those of the 1D model presented in our prior work.

For liquid transfer between a flat plate and a cavity, the electric field modifies the pressure distribution in the bridge, and as a consequence, also the interface shapes and pressure gradients near the contact lines. In particular, the pressure gradient near the contact line on the cavity wall is increased, causing the contact line to slip more. This overcomes the apparent pinning that occurs in the absence of the electric field, and allows more liquid to be transferred to the top plate, even when the top plate is less wettable than the flat plate. Notably, the modification is more pronounced for a deep cavity, resulting in a larger transfer ratio compared to a shallow cavity. In contrast to case of liquid transfer between two flat plates, surface charge does not have as significant an influence on liquid transfer due to the way the cavity and electric field modify the interface shape near the contact line.

The results of this work provide a foundation for understanding the physical mechanisms underlying electrostatic assist. At high printing speeds ($Ca \sim 1$), the transfer ratio is only 50% in the absence of an electric field for liquid transfer between two flat plates. For liquid transfer from a cavity, the transfer ratio can be even lower due to an apparent pinning of the contact line on the cavity wall. To overcome these limits, and thus reduce printing defects, additional forces such as electric fields must be used. The present work illustrates the physical mechanisms through which electric fields can improve liquid transfer. The results are relevant not only to printing, but potentially also to other applications [46] such as adhesion, tribology, and microfluidics, where liquid bridges with moving contact lines appear.

Chapter 5

Final Remarks

In this thesis, we have investigated electrohydrodynamic effects on liquid transfer in gravure printing processes. We use a combination of theory and experiment to understand the fundamental mechanisms by which electrostatic forces influence liquid transfer. In this chapter, we summarize the results in this work and suggest future research directions.

5.1 Conclusions

In Chapter 2 we develop a one-dimensional (1D) slender-jet model and a two-dimensional (2D) axisymmetric model of liquid bridge stretching and compare the resulting predictions with previously published experimental data. The results of our calculations indicate that it is not always necessary to account for contact-angle hysteresis (CAH) to accurately predict liquid transfer. At relatively low stretching speeds, predictions from both models of the amount of liquid transferred agree well with the experimental data. Notably, the amount of liquid transferred is primarily governed by the overall bridge shape and is not significantly influenced by contact-line motion toward the end of bridge stretching. When the stretching speed is high enough, the models predict that each surface receives half the liquid, in agreement with experimental observations. In this regime, viscous forces overwhelm the influence of wettability differences.

For intermediate values of the stretching speed, predictions from each model can deviate substantially from the experimental data, which we speculate is due to the

influence of surface defects that are not included in the models. In this regime, there can be significant differences between the predictions of the 1D and 2D models, which are due to the tendency of the contact line to slip more in the 1D model. Nevertheless, our results also indicate that the simpler 1D model can provide qualitatively accurate descriptions of the transfer ratio as a function of $|\Delta\theta_r|$ and Ca. Thus, the 1D model may be a useful tool for exploratory studies that incorporate other physical effects (e.g., electrostatics). This research provides the first systematic comparison between theory and experiment for liquid transfer in the absence of an electric field. It lays the necessary foundation for studying liquid transfer when an electric field is present.

In Chapter 3, the 1D model is modified to include electrostatic effects and advance fundamental understanding of how electric fields can be used to improve liquid transfer. For perfect dielectrics, the results show that electrostatic forces enhance liquid transfer to the more wettable surface for any stretching speed. The presence of the electric field increases the pressure difference inside the liquid bridge and drives liquid toward the more wettable surface. For leaky dielectrics, the electrostatic contribution to the tangential stress also plays a key role. If the sign of the initial surface charge density and the direction of the electric field are chosen appropriately, nearly all the liquid can be driven to the more wettable plate. More generally, our results suggest that the surface charge and electric field can be used to augment or oppose flows driven by wettability differences. Our work advances fundamental understanding of electrostatic assist (ESA), a method used in inudstrial printing processes to improve liquid transfer. Results from our flow visualization experiments reveal that electric fields can also significantly influence contact-line motion. This research provides the first systematic explanation for the physical mechanisms underlying ESA. It provides a necessary basis for extending the model to consider liquid transfer from cavities.

In Chapter 4, we include electrostatic effects into the 2D model to determine how cavity shape influences liquid transfer when an electric field is present. We show that electric fields can be used to enhance liquid transfer for two different geometries. When both plates are flat, the presence of an electric field lowers the pressure inside the perfect dielectric liquid bridge. This lower pressure enables the liquid bridge to be stretched longer, so the contact line on the more wettable surface has more time to slip down the surface. As a result, more liquid is transferred to the more wettable surface. For the

leaky dielectrics, the sign of the surface charge density and the direction of the electric field can be controlled appropriately to transfer more liquid to the target substrate regardless the wettability difference.

When the perfect dielectric liquid bridge is stretched between a cavity and a flat plate, application of an electric field also lowers the pressure in bulk and thus significantly increases the pressure difference near the contact line on cavity wall. As a result, the contact line slips off the cavity wall, and more liquid is transferred to the flat substrate. However, for leaky dielectrics, the initial surface charge density and the conductivity do not further enhance liquid transfer. The tangential component of the electric field is near zero near both contact lines because the interface near the contact line is perpendicular to the electric field. As a result, the electrostatic contribution to the tangential stress is too weak to influence the contact line motion significantly.

This work is inspired by the application of ESA in gravure printing processes to reach more than 50% of liquid transferred from cavity to the substrate. Our results indicate that electric fields can be an effective way to overcome the 50% barrier. This work advances the fundamental understanding of the application of electrostatic assist and provides the guideline in designing ESA systems to help in reducing printing defects.

5.2 Future research directions

Through out this work, we have studied how electrohydrodynamic effects and trapezoidal cavities influence the stretching of the liquid bridge and liquid transfer. Although this work has shed a light on fundamental understanding of liquid transfer in an electric field, there are still many problems that need to be explored in the future.

In printed electronics, the inks often contain conductive nanoparticles, solvents or polymeric materials, resulting in complex non-Newtonian behaviors. The polymeric material may exhibit viscoelastic, shear thinning and shear thickening behaviors. These behaviors can significantly alter the liquid viscosity or the surface tension during the liquid transfer. Therefore, we can expand this work by considering more complex fluid rheology in the model. In addition, the interaction between viscoelasticity and electrohydrodynamic effects is essential to further understand electrostatic assist in printed electronic processes. The slender-jet model that we discussed in chapter 3 will be an

useful tool to investigate these effects. The effect of viscoelasticity can be included by changing in the constitutive relationships. However, the slender-jet model can only be used to study the liquid transfer between two flat surfaces because the liquid transfer with cavities is inherent a two-dimensional problem. A two- or three-dimensional model is still required to study the liquid transfer with the presence of the cavities.

The presence of the particles will also influence ink transfer. The incomplete ink transfer may cause the accumulation of the particles in the cells, resulting to the poor quality of the printing products after drying. Additionally, the colloidal particles may contain charges. The presence of the electric field can affect the flow of the conductive particles. Therefore, electrokinetics effects may have to be included in the model.

In chapter 2, we discussed the discrepancy of contact line motion between the experimental results and model predictions. We also notice that the contact radii expand near the end of stretching. In section 3.5, we found that the presence of the electric field can deform the shape of the liquid bridge and thus allow the contact line on the less wettable surface to move. Even though our models yield predictions consistent with the experimental observations by accounting for the different boundary conditions, our model is unable to predict this transition before the observation. In order to obtain a better prediction of liquid transfer or contact-line motion, it may be necessary to account for the contact angle hysteresis and the speed-dependence of the contact angle to accurately describe contact-line motion near bridge breakup, where the contact-line speed increases rapidly.

As we discussed in section 3.5.4, the results from our flow visualization experiments show that electric fields unpin the contact line and thus significantly influence contact-line motion, which is not currently feasible in our model. Experimental studies of liquid transferred from a cavity to a flat surface with electric fields will provide the opportunity to further understand the physical mechanisms of ESA. In order to observe the contact line motion within the cavity, a transparent cavity, which can be made by polyurethane, is needed. The surface of the cavity can be modified chemically to alter the wettability. This transparent cavity will allow us to directly observe the liquid in the cavity. The transfer ratio can be calculated by weighting the liquid in the cavity before and after liquid bridge stretching. Therefore, we can advance the physical understanding of how the electric field and cavity shape influence the contact line motion and thus the liquid

transfer, which will ultimately provide insight into how ESA works.

5.3 Final remarks

Through this thesis, we have investigated the influence of the electrostatics and geometries on liquid transfer in printing processes. The research results obtained from a combination of both theory and experiment will provide guidance on how to design cavity shape, surface wettability, and electric field strength to maximize liquid transfer. In addition to advancing fundamental understanding of liquid bridges, the results of this work will aid the optimization of printing processes for manufacturing electronic devices. We hope that this thesis provides better fundamental understandings of electrostatic assist and builds a solid foundation for studying the transfer of complex fluids in the presence of electric fields.

References

[1] Accessed at www.steinerfilm.de.

[2] gigaom.com.

[3] K. B. Morris. Electrostatically assisted gravure. *Printing Technology*, 12(3):180–195, 1968.

[4] C. Gupta, G. A. Mensing, M. A. Shannon, and P. J. A. Kenis. Double transfer printing of small volumes of liquids. *Langmuir*, 23(5):2906–2914, 2007.

[5] H. Chen, T. Tang, and A. Amirfazli. Liquid transfer mechanism between two surfaces and the role of contact angles. *Soft Matter*, 10(15):2503–2507, 2014.

[6] H. Chen, T. Tang, and A. Amirfazli. Effects of surface wettability on fast liquid transfer. *Phys. Fluids*, 27:112102, 2015.

[7] B. Qian and K. S. Breuer. The motion, stability and breakup of a stretching liquid bridge with a receding contact line. *J. Fluid Mech.*, 666:554–572, 2011.

[8] http://www.flexiblecircuit.com/products/flex-printed/index.php.

[9] S. Tekoglu, G. Hernandez-Sosa, E. Kluge, U. Lemmer, and N. Mechau. Gravure printed flexible small-molecule organic light emitting diodes. *Org. Electron.*, 14:3493?3499, 2013.

[10] M. Bariya, Z. Shahpar, H. Park, J. Sun, Y. Jung, W. Gao, H. Nyein, T Liaw, L. Tai, Q. P. Ngo, M. Chao, Y. Zhao, M. Hettick, G. Cho, and A. Javey. Roll-to-Roll gravure printed electrochemical sensors for wearable and medical devices. *ACS Nano*, 12(7):6978–6987, 2018.

[11] http://www.qmcdots.com/products/products-solar.php.

[12] https://www.idtechex.com/.

[13] A. Carlson, A. M. Bowen, Y. Huang, R. G. Nuzzo, and J. A. Rogers. Transfer printing techniques for materials assembly and micro/nanodevice fabrication. *Adv. Mater.*, 24(39):5284–5318, 2012.

[14] P. F. Moonen, I. Yakimets, and J. Huskens. Fabrication of transistors on flexible substrates: From mass-printing to high-resolution alternative lithography strategies. *Adv. Mat.*, 24(41):5526–5541, 2012.

[15] M. Jung, J. Kim, J. Noh, N. Lim, C. Lim, G. Lee, J. Kim, H. Kang, K. Jung, A.D. Leonard, J.M. Tour, and G. Cho. All-printed and roll-to-roll-printable 13.56-MHz-operated 1-bit RF tag on plastic foils. *IEEE Trans. Electron Devices*, 57:571–580, 2010.

[16] R. Abbel, Y. Galagan, and P. Groen. Roll-to-Roll fabrication of solution processed electronics. *Adv. Eng. Mater.*, 2018.

[17] A. Huebler, B. Trnovec, T. Zillger, M. Ali, N. Wetzold, M. Mingebach, A. Wagenpfahl, C. Deibel, and V. Dyakonov. Printed paper photovoltaic cells. *Advanced Energy Materials*, 6:1018?1022, 2011.

[18] R. Sondergaard, M. Hosel, and F. Krebs. Roll-to-roll fabrica- tion of large area functional organic materials. *J. Polym. Sci. B Polym. Phys.*, 51:16–34, 2013.

[19] M. Yi, D. Yeom, W. Lee, S. Jang, and G. Choi. Scalability on roll-to-roll gravure printed dielectric layers for printed thin film transistors. *J. Nanosci. Nanotechnol.*, 13(8):5360–5364, 2013.

[20] G. Grau, J. Cen, H. Kang, R. Kitsomboonloha, W. J. Scheideler, and V. Subramanian. Gravure-printed electronics: recent progress in tooling development, understanding of printing physics, and realization of printed devices. *Flex. Print. Electron*, 1:023002, 2016.

[21] M. Hambsch, K. Reuter, M. Stanel, G. Schmidt, H. Kempa, U. Fugmann, U. Hahn, and A.C. Hubler. Uniformity of fully gravure printed organic field-effect transistors. *Mater. Sci. Eng., B*, 170(1):93 – 98, 2010.

[22] R. D. Gamota, P. Brazis, K. Kalyanasundaram, and J. Zhang. *Printed organic and molecular electronics*. Kluwer Academic Publishers, 2004.

[23] J. Noh, D. Yeom, C. Lim, H. Cha, J. Han, J. Kim, Y. Park, V. Subramanian, and G. Cho. Scalability of roll-to-roll gravure-printed electrodes on plastic foils. *Electronics Packaging Manufacturing, IEEE Transactions on ...*, 33(4):275–283, 2010.

[24] B. Michel, A. Bernard, A. Bietsch, E. Delamarche, M. Geissler, D. Juncker, H. Kind, J. P. Renault, H. Rothuizen, H. Schmid, P. Schmidt-Winkel, R. Stutz, and H. Wolf. Printing meets lithography: Soft approaches to high-resolution printing. *IBM J. Res. Dev.*, 45(5):697–719, 2001.

[25] N. Hoda and S. Kumar. Boundary integral simulations of liquid emptying from a model gravure cell. *Phys. Fluids*, 20(9):092106, 2008.

[26] X. Yin and S. Kumar. Flow visualization of the liquid-emptying process in scaled-up gravure grooves and cells. *Chem. Eng. Sci.*, 61(4):1146–1156, 2006.

[27] H. F. George. Electrostatically assisted ink transfer in gravure printing. *ACS Symposium Series*, 200:359–370, 1982.

[28] https://eltex.de/en/product-category/systems/esa-en.

[29] Accessed at www.shinko-jp.biz/english/contents/product/print.html.

[30] C. N. C. Lam, R. Wu, D. Li, M. L. Hair, and A. W. Neumann. Study of the advancing and receding contact angles: Liquid sorption as a cause of contact angle hysteresis. *Adv. Colloid Interface Sci.*, 96(1-3):169–191, 2002.

[31] J. Eggers and E. Villermaux. Physics of liquid jets. *Rep. Prog. Phys.*, 71(3):036601, 2008.

[32] J. R. Melcher and G. I. Taylor. Electrohydrodynamics: A review of the role of interfacial shear stresses. *Annu. Rev. Fluid Mech.*, 1(1):111–146, 1969.

[33] D. A. Saville. Electrohydrodynamics: The Taylor-Melcher leaky dielectric model. *Annu. Rev. Fluid Mech.*, 29:27–64, 1997.

[34] M. M. Hohman, M. Shin, G. Rutledge, and M. P. Brenner. Electrospinning and electrically forced jets. I. stability theory. *Phys. Fluids*, 13(8):2201–2220, 2001.

[35] G. Taylor. Studies in electrohydrodynamics. I. The circulation produced in a drop by electrical field. *Proc. R. Soc. A*, 291:159–166, 1966.

[36] G. Taylor. Disintegration of water drops in an electric field. *Proc. R. Soc. A*, 280:383–397, 1964.

[37] O. A. Basaran and F. K. Wohlhuter. Effect of nonlinear polarization on shapes and stability of pendant and sessile drops in an electric (magnetic) field. *J. Fluid Mech.*, 244:1–16, 1992.

[38] C. L. Burcham and D. A. Saville. The electrohydrodynamic stability of a liquid bridge: Microgravity experiments on a bridge suspended in a dielectric gas. *J. Fluid Mech.*, 405:37–56, 2000.

[39] C. L. Burcham and D. A. Saville. Electrohydrodynamic Stability: Taylor-Melcher theory for a liquid bridge suspended in a dielectric gas. *J. Fluid Mech.*, 452:163–187, 2002.

[40] S. Herminghaus. Dynamical instability of thin liquid films between conducting media. *Phys. Rev. Lett.*, 83:2359–2361, 1999.

[41] S. A. Roberts and S. Kumar. Electrohydrodynamic instabilities in thin liquid trilayer films. *Phys. Fluids*, 22(12):122102, 2010.

[42] H. Sirringhaus, T. Kawase, R. H. Friend, T. Shimoda, M. Inbasekaran, W. Wu, and E. P. Woo. High-resolution inkjet printing of all-polymer transistor circuits. *Science*, 290:2123–2126, 2000.

[43] J. J. Feng. The stretching of an electrified non-Newtonian jet: A model for electrospinning. *Phys. Fluids*, 14(11):3912–3926, 2002.

[44] A. Corbett and S. Kumar. Spreading of thin droplets of perfect and leaky dielectric liquids on inclined surfaces. *Langmuir*, 32:6606–6617, 2016.

[45] A. Ramkrishnan and S. Kumar. Electrohydrodynamic effects in the leveling of coatings. *Chem. Eng. Sci.*, 101:785–799, 2013.

[46] S. Kumar. Liquid transfer in printing processes: Liquid bridges with moving contact lines. *Annu. Rev. Fluid Mech.*, 47(1):67–94, 2015.

[47] M. J. Vogel and P. H. Steen. Capillarity-based switchable adhesion. *Proc. Natl. Acad. Sci.*, 8:3377–3381, 2010.

[48] S. Gaudet, G. H. McKinley, and H. A. Stone. Extensional deformation of Newtonian liquid bridges. *Phys. Fluids*, 8:2568–2579, 1996.

[49] T. M. Squires and S. R. Quake. Microfluidics: Fluid physics at the nanoliter scale. *Rev. Mod. Phys.*, 77:977–1026, 2005.

[50] M. Pudas, J. Hagberg, and S. Leppavuori. Printing parameters and ink components affecting ultra-fine-line gravure-offset printing for electronics applications. *J. Eur. Ceram. Soc.*, 24(10-11):2943–2950, 2004.

[51] R. Gaudiana and C. Brabec. Organic materials: Fantastic plastic. *Nat. Photonics*, 2:287–289, 2008.

[52] F. C. Krebs. Fabrication and processing of polymer solar cells: A review of printing and coating techniques. *Sol. Energy Mater. Sol. Cells*, 93(4), 2009.

[53] P. Kopola, T. Aernouts, S. Guillerez, H. Jin, M. Tuomikoski, A. Maaninen, and J. Hast. High efficient plastic solar cells fabricated with a high-throughput gravure printing method. *Sol. Energy Mater. Sol. Cells*, 94, 2010.

[54] C.-H. Huang, M. S. Carvalho, and S. Kumar. Stretching liquid bridge with moving contact lines: Comparison of liquid-transfer predictions and experiments. *Soft Matter*, 12:7457–7469, 2016.

[55] A. V. Chadov and E. D. Yakhnin. Investigation of the transfer of a liquid from one solid-surface to another .1. slow transfer - method of approximate calculation. *Colloid J. of the Ussr*, 41(4):700–703, 1979.

[56] E. D. Yakhnin and A. V. Chadov. Investigation of the transfer of a liquid from one solid-surface to another .2. dynamic transfer. *Colloid J. USSR*, 45(6):1034–1039, 1983.

[57] S. Dodds, M. S. Carvalho, and S. Kumar. Stretching and slipping of liquid bridges near plates and cavities. *Phys. Fluids*, 21(9):092103, 2009.

[58] H. Chen, A. Amirfazli, and T. Tang. Modeling liquid bridge between surfaces with contact angle hysteresis. *Langmuir*, 29(10):3310–3319, 2013.

[59] H. Chen, T. Tang, and A. Amirfazli. Effect of contact angle hysteresis on breakage of a liquid bridge. *Eur. Phys. J. Spec. Top.*, 224:277–288, 2015.

[60] H. Chen, T. Tang, H. Zhao, K.-Y. Lao, and A. Amirfazli. How pinning and contact angle hysteresis govern quasi-static liquid drop transfer. *Soft Matter*, 12:1998–2008, 2016.

[61] H. Chen, T. Tang, and A. Amirfazli. Fast liquid transfer between surfaces: breakup of stretched liquid bridges. *Langmuir*, 31:11470–11476, 2015.

[62] L. H. Tanner. The spreading of silicone oil drops on horizontal surfaces. *J Phys. D Appl. Phys.*, 12(9):1473–1484, 1979.

[63] S. Dodds, M. S. Carvalho, and S. Kumar. Stretching liquid bridges with moving contact lines: The role of inertia. *Phys. Fluids*, 23(9):092101, 2011.

[64] S. Dodds, M. S. Carvalho, and S. Kumar. The dynamics of three-dimensional liquid bridges with pinned and moving contact lines. *J. Fluid Mech.*, 707:521–540, 2012.

[65] M. Mastrangeli. The fluid joint: The soft spot of micro- and nanosystems. *Adv. Mater.*, 27:4254–4272, 2015.

[66] P. M. Gresho, R. L. Lee, and R. L. Sani. On the time-dependent solution of the incompressible Navier-Stokes equations in two and three dimensions. *Recent Advances in Numerical Methods in Fluids*, 1:27–79, 1980.

[67] J. Eggers. Nonlinear dynamics and breakup of free-surface flows. *Rev. Mod. Phys.*, 69(3):865–929, 1997.

[68] J. Eggers and T. F. Dupont. Drop formation in a one-dimensional approximation of the Navier-Stokes equation. *J. Fluid Mech.*, 262:205–221, 1994.

[69] X. Zhang, R. S. Padgett, and O. A. Basaran. Nonlinear deformation and breakup of stretching liquid bridges. *J. Fluid Mech.*, 329:207–245, 1996.

[70] O. E. Yildirim and O. A. Basaran. Deformation and breakup of stretching bridges of Newtonian and sheer-thinning liquids: Comparison of one- and two-dimensional models. *Chem. Eng. Sci.*, 56(1):211–233, 2001.

[71] L. Rayleigh. On the instability of jets. *Proc. R. Soc. London*, 10:4–12, 1878.

[72] J. Plateau. Experimental and theoretical researches on the figures of equilibrium of a liquid mass withdrawn from the action of gravity, etc. *Annual Reports of the Smithsonian Institution*, pages Smithsonian Institution Press, Washington, D.C., 1863.

[73] A. Akbari, R. J. Hill, and T. G. M. van de Ven. Liquid-bridge breakup in contact-drop dispensing: Liquid-bridge stability with a free contact line. *Phys. Rev. E*, 92:022404, 2015.

[74] A. Akbari and R. J. Hill. Liquid-bridge breakup in contact- drop dispensing: Liquid-bridge stability with a free contact line. *Soft Matter*, 12:6868–6882, 2016.

[75] J. B. Bostwick and P. H. Steen. Stability of constrained capillary surfaces. *Annu. Rev. Fluid Mech.*, 47:539–568, 2015.

[76] B. Kang, W. H. Lee, and K. Cho. Recent advances in organic transistor printing processes. *Appl. Mater. Interfaces*, 5:2302–2315, 2013.

[77] H. Kang, R. Kitsomboonloha, K. Ulmer, L. Stecker, G. Grau, J. Jang, and V. Subramanian. Megahertz-class printed high mobility organic thin-film transistors and inverters on plastic using attoliter-scale high-speed gravure-printed sub-5 μm gate electrodes. *Org. Electron.*, 15:3639–3647, 2014.

[78] M. Jung, J. Kim, J. Noh, N. Lim, C. Lim, G. Lee, J. Kim, H. Kang, K. Jung, A. D. Leonard, J. M. Tour, and G. Cho. All-printed and roll-to-roll-printable 13.56-MHz-operated 1-bit RF tag on plastic foils. *IEEE Trans. Electron Devices*, 57:571–580, 2010.

[79] D. Tobjrk and R. sterbacka. Paper electronics. *Adv. Mater.*, 23:1935–1961, 2011.

[80] S. Khan, L. Lorenzelli, and R. S. Dahiya. Technologies for printing sensors and electronics over large flexible substrates: A review. *IEEE Sensors J.*, 15:3164–3185, 2015.

[81] D. Sung, A. F. Vornbrock, and V. Subramanian. Scaling and optimization of gravure-printed silver nanoparticle lines for printed electronics. *IEEE Trans. Compon. Packag. Technol.*, 33:105–114, 2010.

[82] C.-H. Huang and S. Kumar. Electrostatic assist of liquid transfer between flat surfaces. *Langmuir*, 34:5124–5137, 2018.

[83] A. Ramkrishnan and S. Kumar. Electrohydrodynamic deformation of thin liquid films near surfaces with topography. *Phys. Fluids*, 26(12):122110, 2014.

[84] A. V. Joshi, C. Dettke, and J. Steingraeber. Investigation on electrostatic assist and gravure process parameters on solid mottle reduction for shrink films. *J. Coat. Technol. Res.*, 13:375–383, 2016.

[85] J. J. Feng. Stretching of a straight electrically charged viscoelastic jet. *J. Non-Newtonian Fluid Mech.*, 116(1):55–70, 2003.

[86] H. A. Stone, J. R. Lister, and M. P. Brenner. Drops with conical ends in electric and magnetic fields. *Proc. R. Soc. Lond. A*, 455:329–347, 1999.

[87] S. Sankaran and D. A. Saville. Experiments on the stability of a liquid bridge in an axial electric-field. *Phys. Fluids*, 5(4):1081–1083, 1993.

[88] A. Ramos, H. Gonzalez, and A. Castellanos. Experiments on dielectric liquid bridges subjected to axial electric-field. *Phys. Fluids*, 6(9):3206–3208, 1994.

[89] R. McLenaghan and S. Levy. Standard mathematical tables and formulae. *CRC Press*, 1995.

[90] F. C. Krebs. Fabrication and processing of polymer solar cells: A review of printing and coating techniques. *Sol. Energ. Mat. Sol. Cells*, 93:394–412, 2009.

[91] Y. Zheng, Z. He, Y. Gao, and J. Liu. Direct desktop printed-circuits-on-paper flexible electronics. *Sci. Rep.*, 3:1786, 2013.

[92] Q. Thiburce and A. J. Campbell. Low-voltage polyelectrolyte-gated polymer field-effect transistors gravure printed at high speed on flexible plastic substrates. *Adv. Electron. Mater.*, 3:1600421, 2016.

[93] J.-T. Wu, M. S. Carvalho, and S. Kumar. Transfer of rate-thinning and rate-thickening liquids between separating plates and cavities. *J. Non-Newtonian Fluid Mech.*, 255:57–69, 2018.

[94] A. K. Sankaran and J. P. Rothstein. Effect of viscoelasticity on liquid transfer during gravure printing. *J. Non-Newtonian Fluid Mech.*, 175-176:64–75, 2012.

[95] M. S. Carvalho D. M. Campana. Liquid transfer from single cavities to rotating rolls. *J. Fluid Mech.*, 747:545–571, 2014.

[96] D. M. Campana, S. Ubal, M. D. Giavedoni, F. A. Saita, and M. S. Carvalho. Three dimensional flow of liquid transfer between a cavity and a moving roll. *Chem. Eng. Sci.*, 149:169–180, 2016.

[97] J. A. Lee, J. P. Rothstein, and M. Pasquali. Computational study of viscoelastic effects on liquid transfer during gravure printing. *J. Non-Newtonian Fluid Mech.*, 199:1–11, 2013.

[98] T. D. Blake. The physics of moving wetting lines. *J. Colloid Interface Sci.*, 299:1–13, 2006.